LOW-ENERGY ELECTRON DIFFRACTION EFFECTS AT COMPLEX INTERFACES

A Thesis
Presented to
The Academic Faculty

by

Doogie Oh

In Partial Fulfillment
of the Requirements for the Degree
Doctor of Philosophy in the
School of Chemistry and Biochemistry

Georgia Institute of Technology
May 2009

LOW-ENERGY ELECTRON DIFFRACTION EFFECTS AT COMPLEX INTERFACES

Approved by:

Professor Thomas M. Orlando, Advisor
School of Chemistry and Biochemistry
Georgia Institute of Technology

Professor Joseph W. Perry
School of Chemistry and Biochemistry
Georgia Institute of Technology

Professor Phillip N. First
School of Physics
Georgia Institute of Technology

Professor Rigoberto Hernandez
School of Chemistry and Biochemistry
Georgia Institute of Technology

Professor Nicholas V. Hud
School of Chemistry and Biochemistry
Georgia Institute of Technology

Date Approved: May 2009

To my parents,

Haejung Oh and Jungyun Hwang

ACKNOWLEDGEMENTS

I want to express my heartfelt gratitude to my advisor, Dr. Thomas M. Orlando. He presented me with research topics through which I became trained as a true scientist. He taught me how to tackle academic tasks and to present my knowledge and achievement. It is my great fortune to have been his student. I want to thank Dr. Phillip First for giving me directions in graphene research and Dr. Nicholas Hud for guidance in the DNA damage research. In addition, I want to thank Dr. Joseph Perry and Dr. Rigoberto Hernandez for giving me valuable advice regarding preparation of this thesis.

I want to express my sincere gratitude to Nikhil Sharma, a graduate student in the First group, School of Physics. We collaborated on graphene research and he helped me in many ways. Specifically, I appreciate his efforts in sample preparation and the scanning tunneling microscopy studies. Also, I want to thank Dr. Yanfeng Chen, a former Orlando group student. He carried out the DNA damage experiments, and we co-authored a paper on this topic. For the Raman study, I was helped by Harry Abernathy and Dr. Meilin Liu in Materials Science and Engineering at Georgia Institute of Technology. I express my gratitude to them. Richard Bedell and José Fonts in electronics shop are also both appreciated for their help with instrumentation mechanical and electrical assistance.

I would like to thank all of my colleagues in the Orlando group, School of Chemistry and Biochemistry at Georgia Tech. I especially thank senior students, Kristin Shepperd, Babajide Olanrewaju; research scientists, Alexandr Aleksandrov, Gregory Grieves; and a former student, Marcus Johnson. Many thanks also go to Hannah Barks, Michele Dawley, Alice Johnson, Jason McLain, Michael Poston, Torri Rose, Denis Sokolov, and Josh Symonds for helpful suggestions during numerous practice presentations. Also I want to wish good luck to Denis Sokolov who will continue the graphene research in the Orlando group.

Finally, I want to express my deepest gratitude to my family. My parents gave endless love and strength for me so I could overcome all the difficulties during my Ph.D studies. I

also thank my sisters, Yebin Oh and Jieil Oh. Especially, I bless my baby nephew, Seohyun Kim.

TABLE OF CONTENTS

LIST OF FIGURES

SUMMARY

Low-energy electron scattering is used as a tool to study electron-stimulated processes at complex interfaces. The electron diffraction in each complex interface is theoretically treated by a multiple scattering formalism for quantitative analysis. In Chapter 2, mathematical descriptions of electron-stimulated processes and a multiple scattering expansion extended from the single-scattering case are presented. A separable representation of the Green function is used to introduce formalisms for calculating electron intensities with spherical-wave effects which are applicable in low-energy electron diffraction effects at complex interfaces. An abridged version of the theory is published in Physica Scripta **T110** 256 (2004). Zone-specific desorption of Cl^+ ion from Si(111)-7×7 surfaces is revealed by correlating diffraction features in electron-stimulated desorption with calculations of electron intensities at selected sites in Chapter 3. The result was published in Surface Science **600** L245 (2006).

Graphene epitaxially grown on SiC(0001) substrate is characterized by Auger electron diffraction and Raman scattering. In Chapter 4, angle-resolved Auger electron measurements gives Auger electron diffraction features of epitaxial graphene which shows that the buffer layer structure affects the diffraction features. Analysis of the Auger experiments with the scattering formalism suggest that Auger electron diffraction is a useful method to probe epitaxial graphene. This result will be submitted for publication in Surface Science. In Chapter 5, Raman spectroscopy of epitaxial graphene is used to probe epitaxial graphene layers. The Raman shows evolution of the D, G, and 2D band features as a function of ′graphene′ thickness. Studies of peak features as a function of sample thickness reveal electronic and geometric properties of epitaxial graphene on SiC(0001). This work will be submitted for publication in Nano Letters.

The diffraction method applied for analysis of Cl^+ desorption from Si surfaces is further extended into a research topic relevant to biology. Probabilities of DNA strand breaks

induced by low-energy electron collision are correlated with electron intensities calculated based on the scattering formalism. The physics involved in DNA damage may be dominated by dissociative electron attachment and dissociative ionization. The multiple scattering theory is applied in order to correlate experimental results obtained by mass spectrometry and gel electrophoresis. This theoretical "path approach" helps demonstrate the potential role of diffraction in low-energy electron induced damage of hydrated DNA. This study was published in the Journal of Chemical Physics **128** 195102 (2008).

CHAPTER I

INTRODUCTION

1.1 Low-energy electron induced surface processes

Low-energy (< 100 eV) electrons are used to examine surface electronic and atomic structure and are often the probe of choice due to their small penetration depth and strong interaction with the solid. Incident low energy electron beams have been used for surface analysis such as low-energy electron diffraction (LEED) and variants thereof. Other techniques, such as electron energy loss spectroscopy (EELS), secondary electron emission (SEE), Auger electron spectroscopy (AES), and inverse photoemission (IP) depend upon the transfer of energy from the incident electron beam to the solid by an inelastic scattering event.

For adsorbate covered surfaces and condensed phase targets, the inelastic channels can be collective, multi-electron excitations that often "localize" in an adsorbate-substrate or surface complex [1–6]. When this type of localization of electronic energy occurs, non-thermal desorption can ensue via a process known as desorption induced by electronic transitions (DIET). If DIET is initiated by electrons, the overall process is simply referred to as electron-stimulated desorption (ESD) [6].

A very useful technique known as electron-stimulated desorption ion angular distributions (ESDIAD) has also been developed to probe the bonding sites of a wide variety of adsorbate covered surfaces [6, 7]. ESDIAD has been used to show the bonding geometry of Cl atoms on the Si(100)-(2×1) surface [8]. For the study of Cl^+ desorption from Si surfaces, ESD has been used and useful information including the threshold energy has been gleaned [9–12].

1.2 Physics of electron-simulated processes

Surface processes can be activated by incident electrons. During electron collision processes, electronic excitation is needed to break the chemical bond and desorb ionic or neutral fragments. To explain the desorption based on electronic excitation, several models

were proposed. The rate of ESD can be represented by the product of the electronic excitation cross section and the desorption probability according to the Menzel-Gomer-Redhead (MGR) model [4] in which desorption occurs due to the repulsive excited state potential. For ion desorption from ionic or covalent surfaces, Knotek and Feibelman proposed a model involving Auger decay [5].

1.2.1 Desorption models

1.2.1.1 The Menzel-Gomer-Redhead model for ESD

This model incorporates the adiabatic approximation during electronic excitation and semi-classical description of desorption processes. Incident electrons excite the ground state of the surface-adsorbate complex into the antibonding or other high lying states. This transition is instantaneous so the mediated nuclear motion can be separated from the electronic wave-function, which is a Flanck-Condon transition. This process is described in Figure 1.1 as a vertical transition (red line). The excited state is unbound and the species associated with the excitation starts to move away from the surface. If the excited state is de-excitated before the species goes far, it is recaptured into the surface. However, after passing the critical distance, it is desorbed by gaining the kinetic energy over the potential barrier.

1.2.1.2 The Knotek-Feibelman model

The MGR model cannot explain how O^+ can be created from an initially electronegative species such as O^{2-}. This can be created at a higher threshold than the energy required for the transition from bonding to antibonding states. Knotek and Feibelman suggested that interatomic Auger decay following the ionization of a transition metal in metal oxides leads to O^+ ejection [5]. In this model, a core hole is created in the highest lying core state of metal atom, and then, an electron in the oxygen valence band decays inter-atomically. During this process, extra energy is generated and another electron from the valence band can be kicked off into conduction band by overcoming hole-hole repulsion. Finally, oxygen can be desorbed in the neutral or O^+ ion state due to the removal or reversal of the Madelung energy. The Knotek-Feibelman model explains the desorption of ionic systems well.

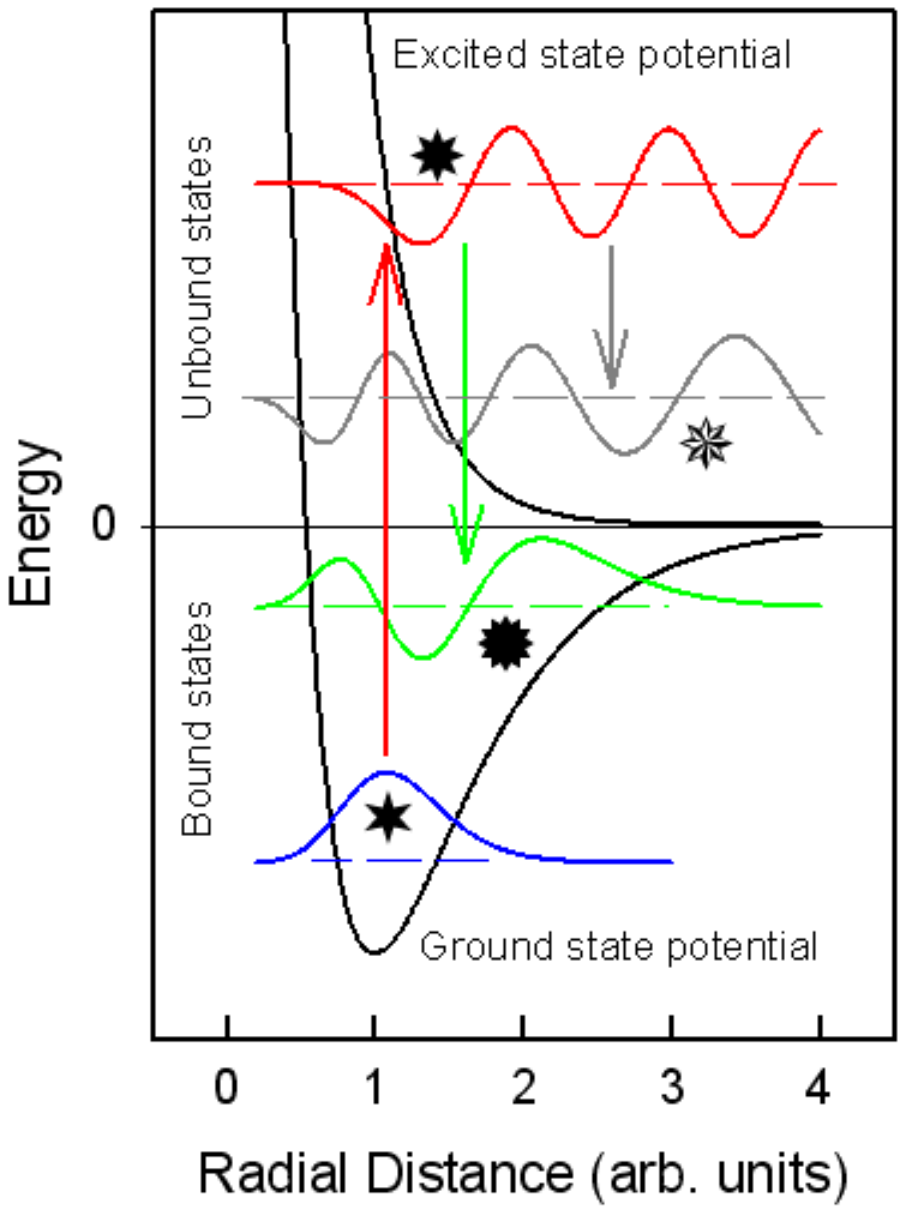

Figure 1.1: Graphical representation of the Menzel-Gomer-Redhead (MGR) model of ESD.

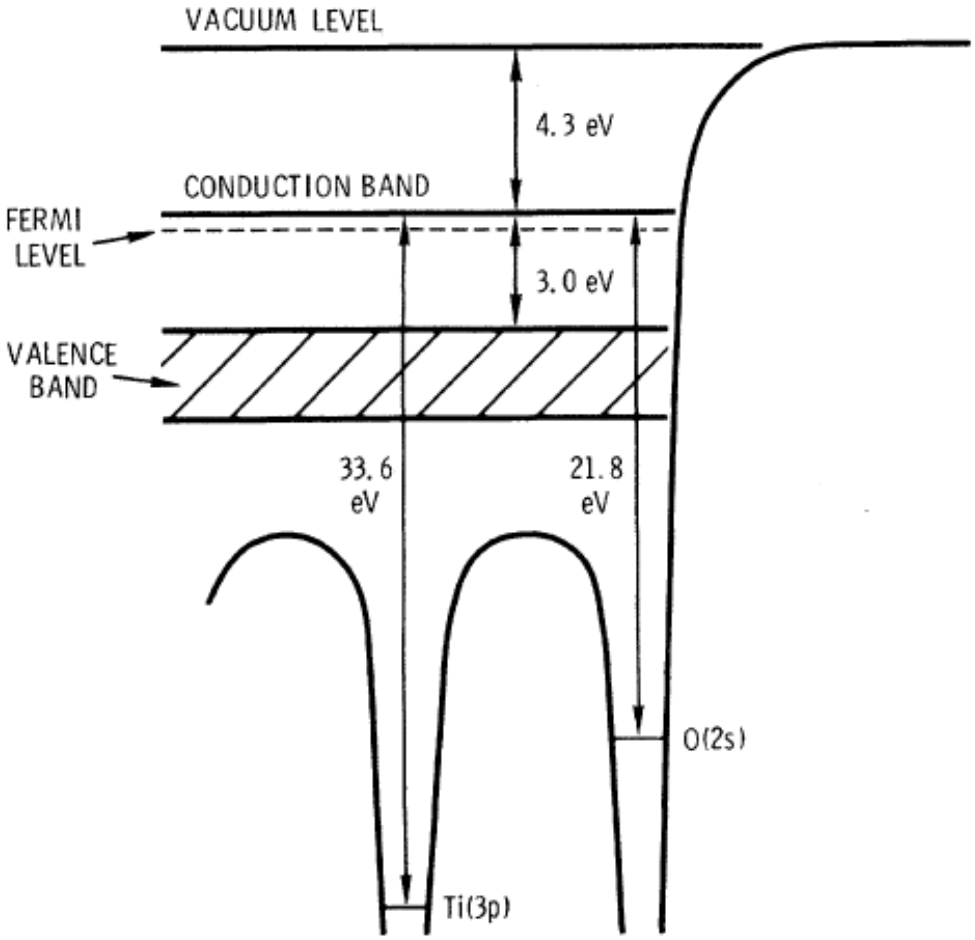

Figure 1.2: Graphical representation of the Kotek-Feibelman model of ESD. This figure is obtained from the reference, M. L. Knotek and Peter J. Feibelman, Phys. Rev. Lett. **40** 964 (1978).

1.2.2 Diffraction effects in electron-stimulated processes

When the incident electron collides with complex targets, its wavefield is initially interfered by elastically scattered components before many body effects induce any further perturbations. However, to date, most treatments have concentrated on final state effects [13–15]. Essentially, no theoretical treatments have focused on the potential importance of initial state effects in diffraction and interference. In this thesis, the most relevant details of a useful multiple scattering description of how diffraction can influence ESD is presented. Previously, Sieger and Orlando observed interference effects in the electron-stimulated desorption of Cl^+ from Cl terminated Si(111) surfaces and referred to this potentially useful affect as diffraction in electron-stimulated desorption (DESD) [16, 17].

Related works on standing wave effects in high energy (e.g. $>$ 1 keV x-rays) photon-stimulated desorption (XPSD) of ions from semiconductor surfaces have also been reported [18–20]. Analysis of the x-ray standing wave (XSW) difference spectra obtained at the Cl 1s absorption edge allowed identification of the ESD active sites from the Si(111)-(1$\times$1):Cl surface and separation of the direct and indirect contributions to ion desorption [18]. A recent analysis of the XSW and XPSD data in conjunction with density functional modeling of the Si(111):Cl system suggests that $SiCl_3$ terminal sites may be selectively revealed. Since DESD relies upon initial state effects and utilizes lower energy ($<$ 50 eV) electrons with low penetration depths, the indirect channels can be minimized near threshold and site specific desorption should also be observable.

1.3 Auger electron diffraction for ultra-thin film analysis

Epitaxial graphene grown on SiC substrate is studied intensively because it has potential for microelectronic applications which might replace the current silicon-based technology. However, there are still many things to be revealed in its structural and electronic properties. For epitaxial graphene grown on SiC, this heterogeneous system is believed to have an interfacial buffer layer. Thus, the device built on the surface will be strongly affected by the perturbation induced in graphitic layers. In this thesis, I apply angle-resolved AES to study a few layers of graphitic sheets grown on SiC surfaces. Normal AES is used for elemental

analysis of surfaces and adsorbate covered surfaces because emitted Auger electrons have short inelastic mean free paths and are element specific. However, the Auger electron diffraction (AED) information can provide important aspects for specific Auger electron emitters. This method is also strengthened by the scattering calculations using the similar theoretical description with those applied for the Cl^+ desorption on Si surfaces and DNA damage.

In addition, Raman scattering spectroscopy based on low-energy electron scattering is introduced for the analysis of epitaxial graphene. The Raman process is initiated by laser excitation. Then, the excited electrons are coupled with phonons and are scattered in low-energy electronic states. Electronic and topographic information regarding the epitaxial graphene can be probed by the outgoing Raman shifted photon. Raman spectroscopy is carried out to monitor the spectral evolution of few layer graphene as the number of epitaxial layers becomes thicker. AED and Raman are complementary to each other for studying epitaxial graphene in terms of controllability, probing media, and available information.

CHAPTER II

THEORETICAL OVERVIEW

2.1 Representation of electron collision processes

2.1.1 Fermi's Golden Rule

Fermi's Golden rule is introduced to derive equations for electron collision processes according to the theory of the impact ionization (e-2e) spectroscopy of solids [21–23]. I use hartree atomic units, $e = \hbar = m = 1$ for all mathematical expressions. By Fermi's Golden rule, the rate of collision processes is expressed as

$$\Gamma_{i\to f} = 2\pi|\langle 34|H_{ee}|12\rangle|^2 \rho_{if}\delta(E_f - E_i) \tag{1}$$

where ρ_{if} is the density of initial and final states, H_{ee} is the electron-electron interaction Hamiltonian, and the δ-function conserves the total system energy. The initial state of the projectile (target) electron is labeled by the index 1 (2), and the final state of the projectile (target) electron is labeled 3 (4). The pictorial description of the process is presented in Figure 2.1.

For the case of ESD processes, it is assumed that ion desorption is initiated by a screened shallow or deep core level and final state effects are not treated. Also, the electron-electron interaction Hamiltonian can be expressed in a simple form which does not account for small

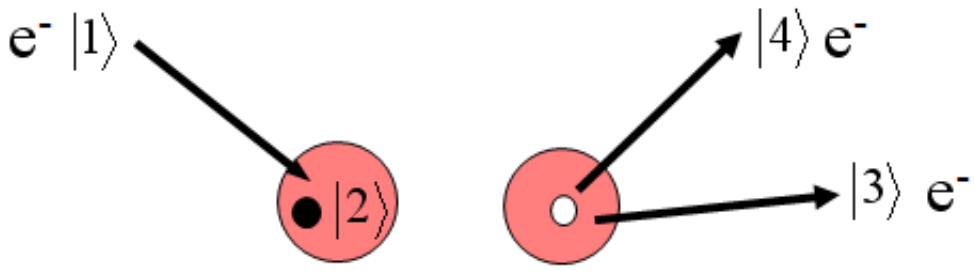

Figure 2.1: Description of an electron collision process. The incoming electron with state 1 collides with electron 2 and this process produces final states of two electrons with state 3 and 4.

magnetic and retardation effects in low-energy electron collisions. The final form without considering electron exchange is approximated by

$$\Gamma_{if} \propto \int\int \rho_1(\mathbf{k},\mathbf{r}) \frac{e^{-2a|\mathbf{r}-\mathbf{r}'|}}{|\mathbf{r}-\mathbf{r}'|^2} \rho_2(\mathbf{r}') d\mathbf{r} d\mathbf{r}' \tag{2}$$

where $\rho_1(\mathbf{k},\mathbf{r})$ is the charge density of the incident electron with wave vector $\mathbf{k}$, $\rho_2(\mathbf{r}')$ the charge density of the target electron, and a screened Coulomb interaction represents the electron-electron interaction Hamiltonian with screening length a^{-1}. The screening length used in the calculations is short so that the interaction integral can be reduced to the point overlap integral. This mediates that the ESD rate is proportional to the probability of finding the incident electron in the vicinity of the absorber located at $\mathbf{R}_a$. It can be represented by

$$I \propto \psi^*(\mathbf{R}_a)\psi(\mathbf{R}_a). \tag{3}$$

$\psi(\mathbf{R}_a)$ is the electron wave function at position $\mathbf{R}_a$ in the presence of the surface and $\psi^*(\mathbf{R}_a)$ is the complex conjugate of the wave function.

2.1.2 Electron diffraction in collisions with surfaces

In order to calculate the interaction integral, we need to obtain the complete description of the incident electron density on the surface. The electron density is formed by the interference of the directly incoming electron wave with wave components elastically scattered by near-surface atoms. Therefore, the incident electron wavefunction, $\psi(\mathbf{r})$ can be expanded in a multiple-scattering series,

$$\psi(\mathbf{r}) = \phi^0(\mathbf{r}) + \phi^1(\mathbf{r}) + \phi^2(\mathbf{r}) + \ldots + \phi^N(\mathbf{r}). \tag{4}$$

Successive terms represent no scattering, single scattering, double scattering, etc. In the limit, as $N \to \infty$, ψ represents the solution to the time-independent Schrdinger equation in the solid. As $\mathbf{r} \to \infty$, this formalism reduces to low energy electron diffraction theory.

2.1.2.1 Plane-wave approximation

In the absence of scattering, the incident electron wave function is

$$\phi^0(\mathbf{r}) = \langle \mathbf{r}|\mathbf{k}\rangle = e^{i\mathbf{r}\cdot\mathbf{k}} e^{-\frac{z}{\lambda\cos(\theta)}}. \tag{5}$$

In Eq. (5), $\mathbf{k}$ is the electron wave-vector, corrected for refraction through the inner potential, V_0. The right-hand exponential represents attenuation of the incident plane wave from inelastic scattering processes. λ is the inelastic scattering mean-free path, z is the vertical distance traveled in the solid, and θ is the angle between $\mathbf{k}$ and the surface normal.

The electron wave function in the presence of the surface can be approximated to first order by

$$\psi(\mathbf{r}) \simeq \phi^0(\mathbf{r}) + \sum_{i=1}^{N} \phi^0(\mathbf{R}_i) f(\theta_s) \frac{e^{ik|\mathbf{R}_i - \mathbf{r}|}}{ik|\mathbf{R}_i - \mathbf{r}|} e^{\frac{-|\mathbf{R}_i - \mathbf{r}|}{\lambda}}. \tag{6}$$

$\mathbf{R}_i$ are bond vectors of the N lattice atoms in the cluster surrounding the absorber at $\mathbf{R}_a$. The scattering factor, $f(\theta)$ is obtained by the usual asymptotic atomic scattering formula

$$f(\theta) = \sum_{l} (2l+1) e^{i\delta_l} \sin(\delta_l) \mathrm{P}_l(\cos\theta). \tag{7}$$

l is angular momentum quantum number, $e^{i\delta_l}\sin(\delta_l)$ is the scattering matrix, and $\mathrm{P}_l(\cos\theta)$ is the Legendre polynomial. This model invokes several simplifying approximations: i) spherical-wave effects are neglected, ii) the interaction with the absorber is assumed to occur at a point (point-excitation approximation) iii) the absorber potential is ignored, and iv) the effect of lattice vibrations is neglected. While admittedly simplified, however, this model is sufficient to reproduce the essential features of the relevant physics, and is valid in the limit of high electron energy ($E > 1$ keV) and short mean-free-paths.

2.1.2.2 Spherical wave effects

At low energy electrons ($E < 1$ keV) and short bond lengths ($kR < 10$), spherical wave effects can be important because low-energy electrons are more sensitive to local scattering potentials than high-energy electrons. In order to take into account the curved-wave effect and also to expand the formulas in a multiple scattering series for low-energy electron diffraction, several approaches have been introduced. Among them, path approaches based on the perturbation method were successfully applied in extended x-ray absorption fine structure (EXAFS) [24] and photoelectron diffraction (PED) theories [25]. Although they are not as exact as diagonalization methods, the short mean free path of the photoelectron makes them very competitive because long paths are smeared out by short lifetimes. Detailed formalisms incorporating spherical wave effects can be derived from the Lippman-Schwinger

equation. General aspects are developed in the next section.

2.2 Multiple scattering formalism with separable representation

2.2.1 Multiple scattering expansion

The electron scattering formalism with complex potentials is developed starting from the Lippman-Schwinger equation with a single potential,

$$|\psi_{\mathbf{k}}\rangle = |\phi_{\mathbf{k}}\rangle + \frac{1}{E - H_0 + i\eta} V|\psi_{\mathbf{k}}\rangle. \tag{8}$$

$|\psi_{\mathbf{k}}\rangle$ and $|\phi_{\mathbf{k}}\rangle$ are electron states in the scattering potential and in free space, respectively. The operator $1/(E-H_0+i\eta)$ is the free-particle Green function operator and notated G_0. It is one of two ingredients in the multiple scattering expansion. The other one is the t-matrix which is defined in the relationship between free particle and perturbed states

$$T(V)|\phi_{\mathbf{k}}\rangle = V|\psi_{\mathbf{k}}\rangle. \tag{9}$$

The Eq. (8) has two perturbed states in both sides so iterative substitution for that in the right side leads to

$$|\psi_{\mathbf{k}}\rangle = |\phi_{\mathbf{k}}\rangle + G_0V|\phi_{\mathbf{k}}\rangle + G_0VG_0V|\phi_{\mathbf{k}}\rangle + G_0VG_0VG_0V|\phi_{\mathbf{k}}\rangle + \cdots . \tag{10}$$

Then, $|\psi_{\mathbf{k}}\rangle$ is substituted in Eq. (9)

$$T(V)|\phi_{\mathbf{k}}\rangle = V(|\phi_{\mathbf{k}}\rangle + G_0V|\phi_{\mathbf{k}}\rangle + G_0VG_0V|\phi_{\mathbf{k}}\rangle + G_0VG_0VG_0V|\phi_{\mathbf{k}}\rangle + \cdots). \tag{11}$$

From Eq(11), the t-matrix operator is expanded into

$$T(V) = V + VG_0V + VG_0VG_0V + VG_0VG_0VG_0V + \cdots . \tag{12}$$

From Eq. (8) and Eq. (9), the Lippman-Schwinger equation becomes

$$|\psi_{\mathbf{k}}\rangle = |\phi_{\mathbf{k}}\rangle + G_0T(V)|\phi_{\mathbf{k}}\rangle. \tag{13}$$

Eq. (13) is the wavefunction in the presence of a single scattering potential. The G_0T operator can be analyzed as scattering with potential V and free propagation. The t-matrix operator T with a single scattering potential can be generalized into the multiple

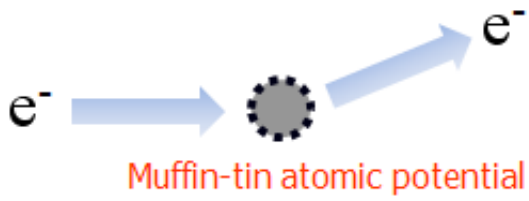

Figure 2.2: Pictorial representation of an electron collision process with an atomic scattering. potential

scattering form by substituting $V = \sum_{i=1} V^i$ in Eq. (12)

$$T(V) = T[\sum_i V^i] = V + VG_0V + VG_0VG_0V + \cdots \tag{14}$$

$$= \sum_i V^i + [\sum_i V^i]G_0[\sum_j V^j] + [\sum_i V^i]G_0[\sum_j V^j]G_0[\sum_k V^k] + \cdots . \tag{15}$$

Eq. (15) can be rearranged by separating out all terms involving only one potential and summing them with each potential to define the cell t-matrices, $t(V^i) \equiv t^i = V^i + V^iG_0V^i + V^iG_0V^iG_0V^i + \cdots$. They are introduced to expand T into total t-matrix

$$T[\sum_i V^i] = \sum_i t^i + \sum_i \sum_{j\neq i} t^iG_0t^j + \sum_i \sum_{j\neq i} \sum_{k\neq j} t^iG_0t^jG_0t^k + \cdots . \tag{16}$$

Now, Eq. (13) can be expanded into the formalism with the total t-matrix of multiple scattering potentials. By substituting this expansion into Eq. (13), the Lippman-Schwinger equation is generalized with multiple scattering potentials. The final form is written as

$$\psi(\mathbf{k},\mathbf{r}) = \langle\mathbf{r}|\mathbf{k}\rangle + \langle\mathbf{r}|\sum_i G_0(\mathbf{r},\mathbf{R}_i)t(\mathbf{R}_i)|\mathbf{k}\rangle + \langle\mathbf{r}|\sum_i \sum_{j\neq i} G_0(\mathbf{r},\mathbf{R}_i)t(\mathbf{R}_i)G_0(\mathbf{R}_i,\mathbf{R}_j)t(\mathbf{R}_j)|\mathbf{k}\rangle + \cdots . \tag{17}$$

The shortened bra and ket notation with $\mathbf{r}$ and $\mathbf{k}$ are used to represent the position projection of the electron k-state. All of the free propagators and t-matrices in this equation are parameterized with position vectors. There are three terms at the right hand side in Eq. (17). The first one corresponds to the nonscattered component. Second and third terms are first and second order scattering components. Each term clearly states the corresponding scattering process. The particular component of the incoming electron follows a specific

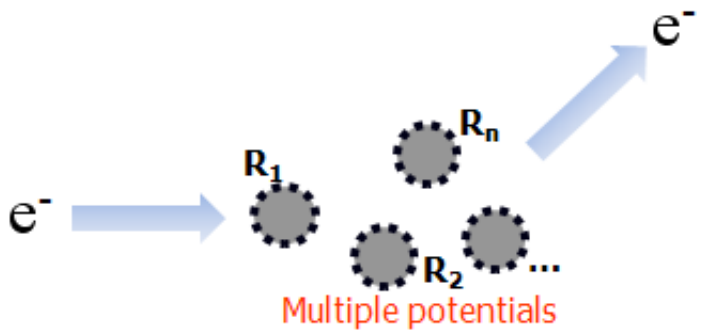

Figure 2.3: Pictorial representation of an electron collision process with multiple atomic scattering potentials.

scattering path and experiences a scattering event that is formulated by the product of the first t-matrix, first free propagation, second t-matrix, second free propagation, and so on.

Two ingredients of the expansion, the free-particle propagator and t-matrix were defined from the single potential Lippman-Schwinger equation. Therefore, the solution with multiple potentials can be treated with single potential solutions instead of directly solving the equation with complicated multiple potentials.

2.2.2 Multiple scattering formalism in electron collisions

Multiple scattering theory is applied to calculate the wavefunction of the incoming or outgoing electrons. For the calculation, however, we need significant computation resources. Here, we make an assumption that higher order terms in the expansions contribute negligibly to the electron wavefield. This can be justified because inelastic processes make higher order components incoherent relative to the nonscattered electron. Therefore, we can neglect higher order components, but still keep the validity of solving the electron wavefunction.

2.2.2.1 Initial-state effects in electron-stimulated processes

In electron-stimulated processes, electron localization may be enhanced by elastic scattering. If so, this may increase the rate of desorption by initial state effects. If only 1st order

scattering is considered, the electron wavefunction at an electron absorber is written by

$$\psi(\mathbf{k}, \mathbf{R}_a) = \langle \mathbf{r}[G_0(\mathbf{R}_a, \mathbf{R}_\infty) + \sum_i G_0(\mathbf{R}_0, \mathbf{R}_i) t(\mathbf{R}_i) G_0(\mathbf{R}_i, \mathbf{R}_\infty)]\mathbf{k}\rangle. \tag{18}$$

where $\mathbf{R}_a$, $\mathbf{R}_\infty$, and $\mathbf{R}_\infty$ are locations of the absorber, e-gun, and scatterers.

2.2.2.2 Final-state effects in Auger electron processes

In Auger electron diffraction processes, outgoing Auger electrons are diffracted by scattered components, which induces a spatial interference pattern. The electron wavefunction at the detector can be also described by:

$$\psi(\mathbf{k}, \mathbf{R}_\infty) = \langle \mathbf{r}[G_0(\mathbf{R}_\infty, \mathbf{R}_e) + \sum_i G_0(\mathbf{R}_\infty, \mathbf{R}_i) t(\mathbf{R}_i) G_0(\mathbf{R}_i, \mathbf{R}_e)]\mathbf{k}\rangle. \tag{19}$$

where $\mathbf{R}_\infty$, $\mathbf{R}_e$, and $\mathbf{R}_i$ are locations of the detector, Auger electron emitter, and scatterers.

2.2.3 Separable representation of Green functions for multiple scattering formalism

Green functions can be based on angular momenta. Calculations in multiple scattering formalism, however, requires the computing resources because the dimension of the Green function rapidly increases with maximum number of angular momentum. In order to overcome this computational bottleneck, it is suggested that the Green function be represented by separable form into

$$\langle L, \mathbf{R}|G_0|L', \mathbf{R}'\rangle = G_{LL'}(\vec{\rho}) = \frac{\exp(i\rho)}{\rho} \sum_\lambda \tilde{\Gamma}^L_\lambda(\vec{\rho}) \Gamma^{L'}_\lambda(\vec{\rho}). \tag{20}$$

where $\vec{\rho} = k(\mathbf{R} - \mathbf{R}')$ are dimensionless vectors of propagation, $L = (l, m)$ are angular momentum quantum numbers, and $\lambda = (\mu, \nu)$ is the summation index. Γ^L_λ and $\tilde{\Gamma}^L_\lambda$ can be solved by applying rotation matrices and z-axis propagators into the explicit form of the Green function, which has been developed by Rehr and Albers [24].

The λ index becomes less important at higher order. For the lowest order $\lambda = (0, 0)$, it becomes $\Gamma^L_{00}(\vec{\rho}) = \sqrt{4\pi} Y_L(\theta, \phi) c_l(\rho)$ and $\tilde{\Gamma}^L_{00}(\vec{\rho}) = \sqrt{4\pi} Y^*_L(\theta, \phi) c_l(\rho)$ where Y are spherical harmonics, (θ, ϕ) are spherical coordinates of $\vec{\rho}$, and c_l is obtained by the Bessel function recurrence relation. Actually, c_l is a spherical-wave correction factor so that as ρ becomes

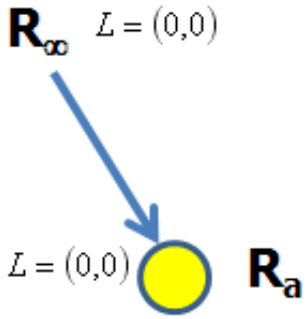

Figure 2.4: Pictorial representation of nonscattered component in an electron-stimulated process.

infinite, $c_l(\rho)$ becomes unity. Then, the separable approach is reduced back to the plane-wave approximation.

With the angular momentum restriction that $L = (0, 0)$ at the e-gun and the absorber, only the $\lambda = (0, 0)$ term becomes effective. Then, the nonscattered term in Eq. (18) is solved into

$$G_{00,00}(\vec{\rho}_{a\infty}) = \frac{\exp(i\rho_{a\infty})}{\rho_\infty}\tilde{\Gamma}^{00}_{00}(\vec{\rho}_{a\infty})\Gamma^{00}_{00}(\vec{\rho}_{a\infty}) \simeq \frac{\exp(i\rho_\infty + i\mathbf{k}\cdot\mathbf{R}_a)}{\rho_\infty}. \tag{21}$$

Both separable terms become unity from the explicit representation and the ρ_∞ value is the distance between the e-gun and the origin point. Therefore, the extra value of $\mathbf{k}\cdot\mathbf{R}_a$ in the argument of the exponential term gives phase information at the absorber site relative to the origin. The distance value in the denominator is written as ρ_∞, which is acceptable because the extra value is negligible compared to the distance from e-gun to origin.

Then, first-order scattered components need to be solved. $\lambda = (0, 0)$ is applied for both indices again from the s-wave assumption of the e-gun and absorber. For one scatterer, the corresponding electron path contributes to overall intensity by

$$\begin{aligned}
&\sum_{L_1} G_{00,L_1}(\vec{\rho}_{a1})t_{l_1}G_{L_1,00}(\vec{\rho}_{1\infty}) \\
&= \frac{\exp(i\rho_{a1})}{\rho_{a1}}\frac{\exp(i\rho_{1\infty})}{\rho_\infty}\sum_{L_1}\tilde{\Gamma}^{00}_{00}(\vec{\rho}_{a1})\Gamma^{L_1}_{00}(\vec{\rho}_{a1})t_{l_1}\tilde{\Gamma}^{L_1}_{00}(\vec{\rho}_{1\infty})\Gamma^{00}_{00}(\vec{\rho}_{1\infty}) \\
&= \frac{\exp(i\rho_{a1})}{\rho_{a1}}\frac{\exp(i\rho_{1\infty})}{\rho_\infty}\sum_{L_1}\Gamma^{L_1}_{00}(\vec{\rho}_{a1})t_{l_1}\tilde{\Gamma}^{L_1}_{00}(\vec{\rho}_{1\infty}) \\
&\simeq \frac{\exp(i\rho_{a1})}{\rho_{a1}}\frac{\exp(i\rho_\infty + i\mathbf{k}\cdot\mathbf{R}_1)}{\rho_\infty}\mathbf{F}_{00,00}(\vec{\rho}_{a1},\vec{\rho}_{1\infty}).
\end{aligned} \tag{22}$$

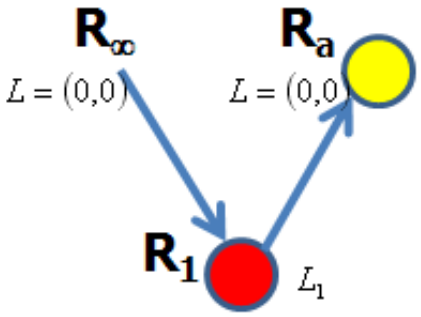

Figure 2.5: Pictorial representation of first-order scattered component in an electron-stimulated process.

In eq. (22),$\sum_{L_1} \Gamma_{00}^{L_1}(\vec{\rho}_{a1}) t_{l_1} \tilde{\Gamma}_{00}^{L_1}(\vec{\rho}_{1\infty})$ is substituted by $\mathbf{F}_{00,00}(\vec{\rho}_{a1}, \vec{\rho}_{1\infty})$. This term is defined by

$$F_{\lambda\lambda'}(\vec{\rho}, \vec{\rho'}) = \sum_{L} \Gamma_{\lambda}^{L}(\vec{\rho}) t_l \tilde{\Gamma}_{\lambda'}^{L}(\vec{\rho'}). \tag{23}$$

where t_l is the t-matrix for the scatterer shared by two consecutive propagation vectors $\vec{\rho}$ and $\vec{\rho'}$. It is notated as the scattering matrix. Again, the extra value of $\mathbf{k} \cdot \mathbf{R}_1$ in the argument of the exponential term gives phase information for scatterer 1.

With the solved form of the nonscattered and first-order scattered terms, the wavefunction with initial-state perturbation in Eq. (18) can be written as

$$\psi(\mathbf{k}, \mathbf{R}_a) = \exp(i\mathbf{k} \cdot \mathbf{R}_a) + \sum_{j} \exp(i\mathbf{k} \cdot \mathbf{R}_j) \frac{\exp(i\rho_{aj})}{\rho_{aj}} \mathbf{F}_{00,00}(\vec{\rho}_{aj}, \vec{\rho}_{j\infty}). \tag{24}$$

In this equation, $\frac{\exp(i\rho_{\infty})}{\rho_{\infty}}$ existed in all terms so that it can be effectively removed from the equation. j is the summation index of each scatterer. Eq. (24) will be used in chapter 3 and 6 for quantitative analysis of experimental results. For calculating the wavefunction with final-state perturbations, similar steps can be taken for Eq. (19) to be written as

$$\psi(\mathbf{k}, \mathbf{R}_{d=\infty}) = \exp(-i\mathbf{k} \cdot \mathbf{R}_e) + \sum_{j} \exp(-i\mathbf{k} \cdot \mathbf{R}_j) \frac{\exp(i\rho_{je})}{\rho_{je}} \mathbf{F}_{00,00}(\vec{\rho}_{\infty j}, \vec{\rho}_{je}). \tag{25}$$

Eq. (25) will be applied in chapter 4 for analyzing Auger electron diffraction results.

CHAPTER III

ZONE-SPECIFIC DESORPTION OF CL^+ ON SI(111)-(7×7):CL SURFACES

Diffraction in electron-stimulated desorption has revealed propensities for Cl^+ desorption from rest atom vs. adatom areas and unfaulted vs. faulted zones of Cl terminated Si(111)-(7×7) surfaces. We associate the 15 eV ± 1 eV threshold with ionization of Si-Cl bonding surface states and formation of screened 2-hole states with Si 3s character. Similar specificity is observed from two different 7×7 reconstructions. This can be due to reduced screening in unfaulted regions and increased hole-hole localization in Si back-bonds within faulted regions.

3.1 Electron-stimulated desorption from semiconductor surfaces

The physics associated with laser and low-energy (1-30 eV) electron interactions with matter is of fundamental and technological concern due to the intense interest in selective modification of surfaces at the atomic and nanoscale. To date, attempts to demonstrate site specific desorption have been restricted to laser stimulated desorption of Si adatoms from Si(111)-(7×7) [26], Si dimers on Si(100)-(2×1) [27], and P and In atoms from InP(110)-(1×1) [28]. Though it is well known that the electronic excitations involved in laser stimulated desorption of semiconducting and ionic materials are often the same as those governing electron-stimulated desorption (ESD) [2], the success in demonstrating spatial control and site specificity in ESD is indeed limited.

A scanning tunneling microscopy (STM) investigation of relatively high energy (2 keV) electron-beam induced damage of pristine Si surfaces reported that single adatom vacancies appeared 1.3 times more frequently in the faulted region of the Si(111)-(7×7) unit cell [29]. Similar STM based ESD studies of Si(111)-7×7:Br surfaces [30–32] have demonstrated reconstructions resulting from electron-stimulated removal of Si adatoms and adsorbed atomic Br. In these studies, the STM was the excitation source and a 15 eV threshold for Br removal

was reported [30].

It is known that the removal probability of adsorbates and terminal atoms can be modulated by the spatial variability in the surface charge density brought about by the interference of incident and elastically scattered electrons [16, 17, 33] or photons [18, 19]. This is controlled by the inherent symmetry and periodicity of the surface and when low energy electrons are used as the excitation source, it can be described as diffraction in electron stimulated desorption (DESD). In this chapter, it is demonstrated that at incident energies where secondary scattering is minimized, DESD leads to and reveals zone and site specificity.

3.2 Si(111)-(7×7) preparation and diffraction effects in ion desorption

3.2.1 Si(111)-(7×7) structure and preparation

Two Si(111) reconstructions are used in this chapber. For initial sample preparation, an n-type Si(111) substrate is cleaned in an ultra-high vacuum (UHV) system (base pressure 2×10^{-10} torr) by heating to 1300 °C for 10 seconds to desorb the oxide layer. After the oxide removal, the bulk terminated Si(111) surface is thermodynamically unstable because it contains many dangling bonds. Then, it is reconstructed with 7×7 periodicity so that the number of dangling bonds in the unit cell is reduced from 42 to 19. The sample is cooled to 450 °C and then to room temperature.

The Si(111)-(7×7)A:Cl is produced by exposing the clean (7×7) surface to 100 Langmuirs of Cl_2 at room temperature. This surface keeps the usual dimer-adatom-stacking (DAS) fault reconstruction with adatom and rest atom dangling bonds saturated by Cl [34, 35]. Figure 3.1(a) shows the structure of Si(111)-(7×7)A:Cl. In the top view of Figure 3.1(a), each atomic site is overlapped with atoms located below. The unit cell of the 7×7 reconstruction is clearly pictured on the figure. The unit cell is divided into two regions. In the left half of the unit cell, bulk Si atoms are located and overlapped with atoms in the surface region. It is called a faulted subunit. In contrast, the right half of the unit cell has a different structure from the left one and is called the unfaulted subunit. Half of bulk Si atoms in the unfaulted subunit are located in hollow sites. There are 19 Cl adsorbates in

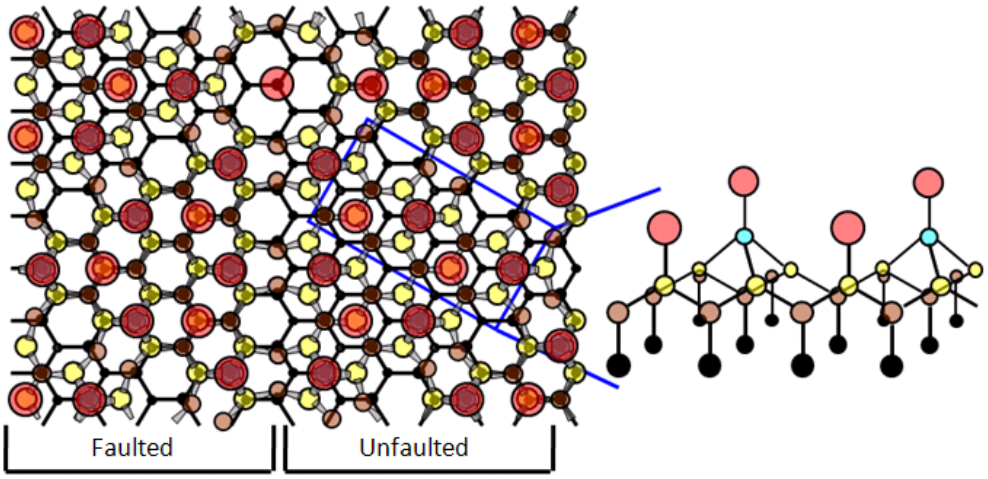

(a) Si(111)-(7×7)A:Cl

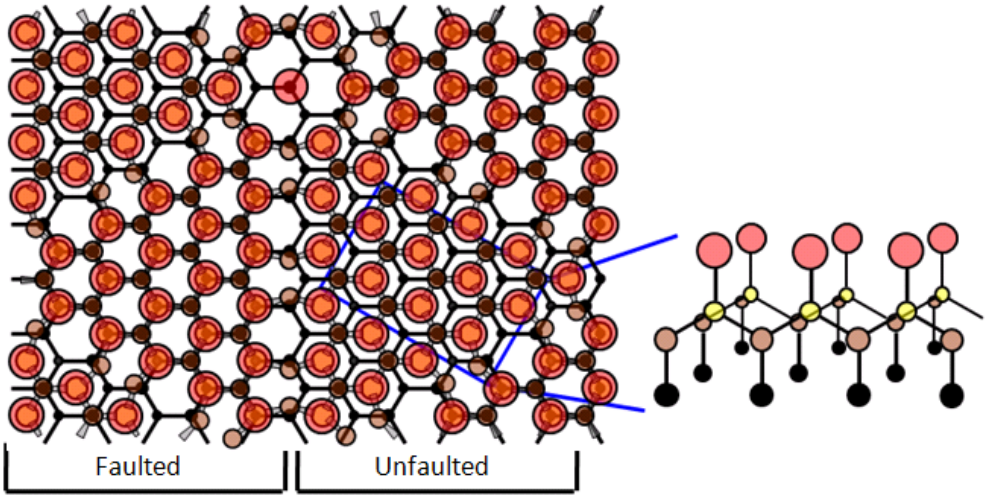

(b) Si(111)-(7×7)B:Cl

Figure 3.1: (a) Top view of Si(111)-(7×7)A:Cl with the side view of a selected region. The red circles located on top are Cl atoms. The blue circles are Si atoms located at adatom sites. Below the adatom layer, yellow circles are the upper layer of the Si bilayer and brown circles, the lower layer. The Si atoms in the bilayer are called rest atoms. Black dots are Si atoms in the bulk layer. The center of the ring shape in the upper layer is called the corner hole site. The surface is assumed to have only atoms which are monochloride. (b) Top view of Si(111)-(7×7)B:Cl with the side view of selected regions. The red circles located on top are Cl atoms. Yellow and brown circles are Si rest atoms of upper and lower layers in the Si bilayer. The corner hole site is presented in the upper center of the surface.

every unit cell. 12 of them are bonded to Si rest atoms, 6 of them to Si adatoms, and one to a Si corner hole. As already mentioned, the number of dangling bonds in the unterminated Si surface is reduced in order to decrease the surface energy.

After Cl atoms are adsorbed on Si surfaces, the 7×7 reconstruction is not stable anymore. Therefore, further reconstructions can be induced by any treatments easily. The second surface reconstruction is prepared by removing Si adatoms from Si(111)-(7×7)A:Cl. It is prepared by annealing the Si(111)-(7×7)A:Cl surface for 5 min at 300 °C. STM studies have shown that this surface retains the stacking fault, but adatoms have been removed and the remaining rest atom dangling bonds are Cl-terminated [35]. Figure 3.1(b) is the model of the Si(111)-(7×7)B:Cl. The Cl adsorbates are all directly bonded onto Si rest atoms and corner holes without intermediate Si adatoms.

3.2.2 Demonstration of diffraction effects in ion desorption

The DESD measurements are carried out in the same UHV system used to produce the Si(7×7)A:Cl and Si(7×7)B:Cl surfaces. This system is equipped with a rotating sample mount, a pulsed low energy (5-100 eV) electron gun (pulse width $\sim 1\mu$s), and a time-of-flight (TOF) mass spectrometer. The general aspects of the experimental setup are illustrated in Figure 3.2 and have been described by Sieger *et.al* [17]. The sample is mounted such that the parallel component of the electron **k**-vector points in the substrate crystal direction $[\bar{1}\bar{1}2]$ at azimuth $\phi = 0$. The electron gun has a fixed 45 polar angle of incidence relative to the sample normal. Data are acquired by leaving the electron gun and TOF spectrometer fixed, while the sample is rotated in azimuth. To ensure that all angular information was due to diffraction, an extraction field pulse of -125 V is applied between the sample and TOF entrance grid immediately following the electron pulse. This also ensured total ion collection. The total desorption yield is measured by integrating the area under the Cl^+ TOF peaks. The TOF spectra consisted solely of Cl^+ isotopes indicating clean samples. The low neutral and Cl^- yields [12] imply that ESD is dominated by Cl^+ removal, especially for excitation energies above 15 eV.

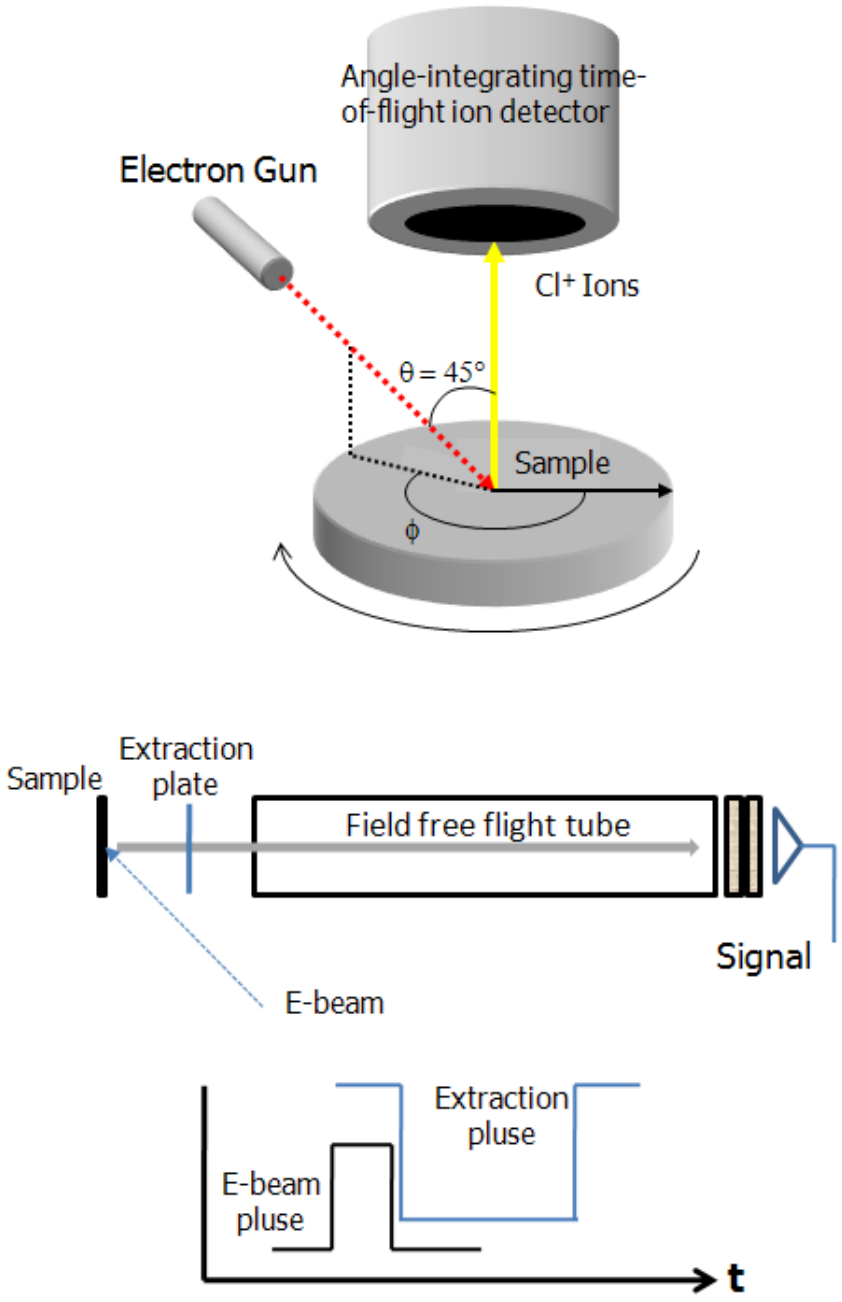

Figure 3.2: The experimental setup for measurement of DESD which uses a time-of-flight (TOF) mass spectrometer. The upper frame describes the experimental setup. The sample is mounted on the rotation sample holder normal to the symmetry axis of the TOF ion detector. The electron gun is fixed at a polar angle $\theta = 45°$ normal to the sample surface. The azimuthal angle ϕ is measured with respect to a specific crystal direction. The middle frame illustrates how TOF works. The bottom frame is the plot of digital signals for e-beam and extraction pulses as a function of time.

3.3 Calculation of incident electron intensity

3.3.1 Formalism

It is assumed that the ESD rate is proportional to the probability of finding the incident electron in the vicinity of an absorber located at $\mathbf{R}_a$. The electron density is formed by the interference of the directly incoming electron wave with components elastically scattered by the near-surface atoms. At low energy and short bond lengths, spherical wave effects can be important. Scattering matrices which can be used to tackle the problem of spherical waves were presented in chapter 2. Here, more detailed aspects of the formalism used for calculating the incident electron intensity are presented.

From Eq. (24), I take the second term in the right-hand side and rewrite it as

$$\phi^1(\mathbf{r}) = \sum_j \mathbf{M}_{00}(\vec{\rho}_{\mathbf{r}j})\mathbf{P}_{00}(\vec{\rho}_{\mathbf{r}j}, \hat{\mathbf{k}})\frac{e^{i\rho_{\mathbf{r}j}}}{\rho_{\mathbf{r}j}}e^{i\mathbf{k}\cdot\mathbf{R}_j}. \tag{26}$$

The product of two new matrices substitute the scattering matrix. The introduction matrix is defined as $\mathbf{P}_\lambda(\vec{\rho}_{\mathbf{r}j}, \hat{\mathbf{k}}) = \sqrt{4\pi}\sum_L \Gamma^L_\lambda(\vec{\rho}_{\mathbf{r}j})t^j_l Y^*_L(\theta, \phi)$. It is a special case of the scattering matrix which describes the collision of an incoming electron into one of scatterers around the selected absorber. The termination matrix, $\mathbf{M}_\lambda(\vec{\rho}_{\mathbf{r}j}) = \tilde{\Gamma}^{00}_\lambda(\vec{\rho}_{\mathbf{r}j})$, represents the process of leading the scattered electron into the absorber. Those matrices have parameters $\vec{\rho}_{\mathbf{r}j}$, which is the propagation vector from one of scatterers to the absorber and $\hat{\mathbf{k}}$ is the unit vector of incident electron $\mathbf{k}$-vector. For first-order components, however, the termination matrix is redundant because λ is $(0, 0)$. These matrices will be useful when higher-order terms are used in calculations. The spherical-wave treatment then becomes an issue of calculating effective scattering amplitudes, f_{eff}, for each order of scattering. The first order effective scattering amplitude is given by

$$f^1_{\text{eff}} = \mathbf{M}_{00}(\vec{\rho}_{\mathbf{r}j})\mathbf{P}_{00}(\vec{\rho}_{\mathbf{r}j}, \hat{\mathbf{k}}). \tag{27}$$

The thermal effect is included by introducing the Debye-Waller factor, $W(T)$, and the inelastic scattering effect is also incorporated by putting the decay term with inelastic mean free path, Λ. Thus, the total first-order scattering component becomes

$$\phi^1(\mathbf{r}) = \sum_j \mathbf{M}_{00}(\vec{\rho}_{\mathbf{r}j})\mathbf{P}_{00}(\vec{\rho}_{\mathbf{r}j}, \hat{\mathbf{k}})\frac{e^{i\rho_{\mathbf{r}j}}}{\rho_{\mathbf{r}j}}e^{i\mathbf{k}\cdot\mathbf{R}_j}W_j(T)e^{-|\frac{\rho_{\mathbf{r}j}}{\mathbf{k}}|/2\Lambda}. \tag{28}$$

We then use it to calculate $I \propto \psi^*(\mathbf{R}_a)\psi(\mathbf{R}_a)$ as a function of incident electron **k**-vector. In order to calculate the intensity, the calculated result of Eq. (28) should be summed with the nonscattered component. This can be calculated by taking into account inelastic decay effects for the first term in the right-hand side of Eq. (24).

3.3.2 Calculation details

The Si(111)-(7×7)A:Cl surface is assumed to have only adatoms which are monochlorides, although minor amounts of di- or tri-chlorides may exist. Calculations for the Si(111)-(7×7)A:Cl surface are carried out for all Si atoms within a 7×7 unit cell which have a dangling bond available to chemisorb Cl or all Cl atoms bonded to those Si atoms. For the Si(111)-(7×7)B:Cl surface, it is clear that all Si adatoms are stripped away and all Si rest atoms are bonded by Cl directly. Calculations for the Si(111)-(7×7)B:Cl surface are done for all 42 Si rest atoms in addition to one corner hole within one unit cell or Cl bonded to these rest atoms.

For the calculations, the cluster comprising atomic scatterers should be chosen to generate scattering paths. However, due to the short electron inelastic mean free path, a reduced cluster diameter less than about 50 $\mathring{A}$ is used, but it is still effective to calculate the first-order scattered electron component. The experimental Si-Cl bond length used is 2.03 $\mathring{A}$ and the inner potential, V_0, is assumed to be 16 eV. All calculations are carried out at 300 K. The direction of the incident electron **k**-vector varies experimentally as a function of azimuthal angle from 0 to 120 ° and the polar angle is fixed at 45 °. Note that the polar angle of the incident electron will be refracted to a larger value due to the silicon crystal inner potential, which should be considered when the electron **k**-vector is used in the calculations. Electron paths in the Si(111) surface are illustrated for calculations in Figure 3.3.

3.4 Cl^+ desorption from Si(111)-(7×7):Cl surface

3.4.1 Comparison between calculated intensities and Cl^+ ion yields

The experimental DESD χ-function (i.e. ion yield fluctuation as a function of azimuthal angle) is obtained by removing a smooth background curve due to incoherent secondary

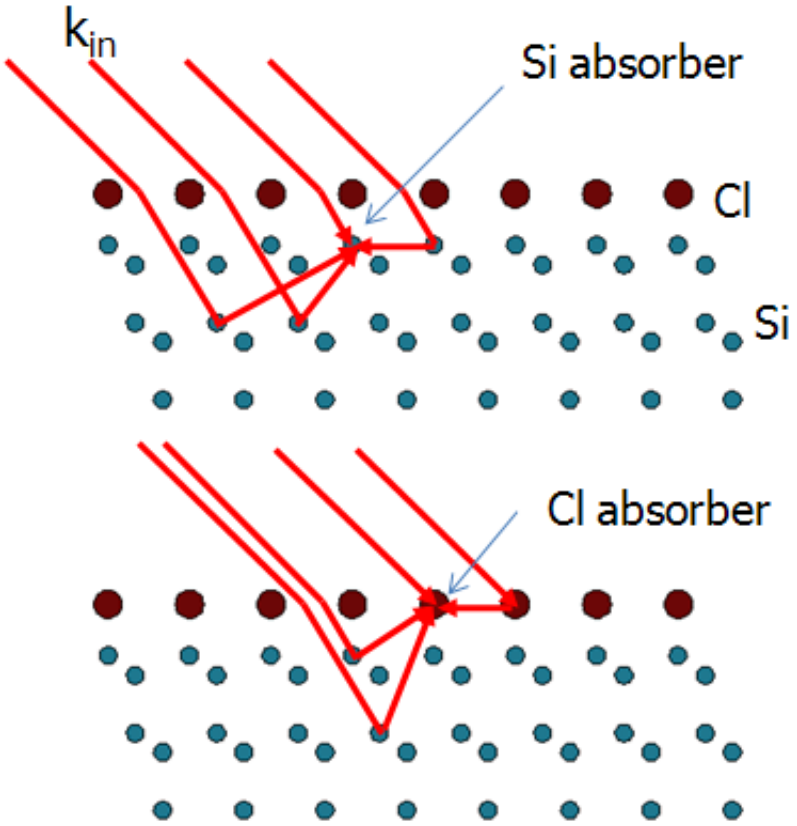

Figure 3.3: Incident electron scattering paths are illustrated in the Si(111) surface interface. In the upper frame, paths are generated for calculating an electron intensity at the Si absorber and the bottom frame is that for the Cl absorber.

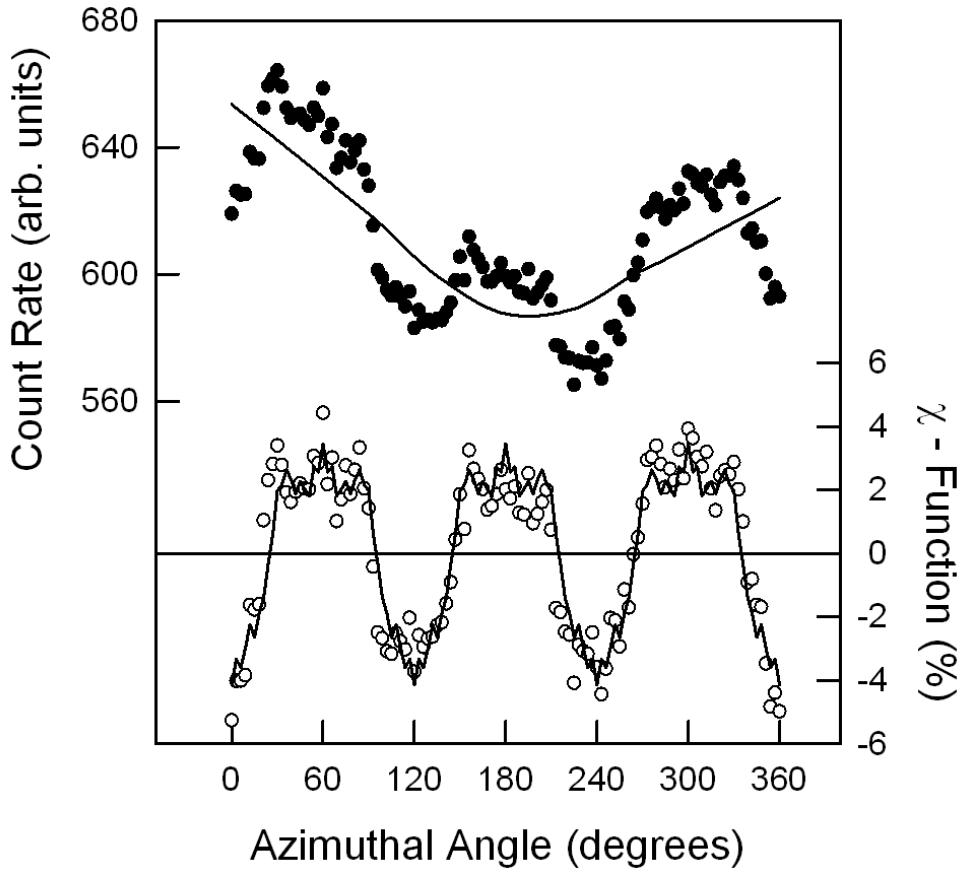

Figure 3.4: Total yield of Cl^+ ion is plotted as a function of azimuthal angle relative to the TOF symmetry axis (M. T. Sieger, G. K. Schenter, and T. M. Orlando, Phys. Rev. Lett. **82** 3348 (1999)). Total ion yield is obtained by integrating the area of the $^{35}Cl^+$ and $^{37}Cl^+$ signals. Upper plot shows the data superimposed on the instrument response function. The χ-function of ion yield is obtained by subtracting the instrument response function.

scattering and is simply $I/I_0 - 1$ where I_0 is the symmetry-averaged Cl^+ yield without electron diffraction effects [16]. One example of obtaining χ-function is presented in Figure 3.4. At 30 eV, the χ-function is approximately 10 percent or less of the total desorption signal due to contributions from secondary scattering. At threshold, though the signal is small, it can be greater than 50 percent.

For the Si(111)-(7×7)A:Cl surface, the calculation in which the excitation is localized on the Cl "absorber" does not display the major peaks at 30 and 90 seen in the χ-function in Figure 3.5(a). In contrast, the calculation using the Si absorber shows these features. There are similar trends in the comparison for the Si(111)-(7×7)B:Cl surface. The calculation using the Si "absorber" does display these peaks as well as the three main features near 30°, 60°, and 90° seen in the χ-function for the Cl-terminated B surface in Figure 3.5(b). Generally speaking, calculations using the Si absorber provide good, although not perfect, matches for Cl^+ desorption from Si(111)-(7×7):Cl surfaces.

The DESD calculation provides the sum of all partial waves from all scattering centers and our analysis is based on matching the χ-function with this summation. To improve the analysis and to examine whether DESD can reveal zone and site specificity, we analyze the Cl^+ desorption based on the electron intensity distribution associated with the faulted and unfaulted regions of the reconstructed Si(111)-(7×7) unit cell. The calculated electron intensity in the upper frame of Figure 3.6(a) is the summation for all Si sites bonded to Cl absorbates on the faulted subunit of the Si(111)-(7×7)A:Cl surface whereas the middle frame is the summation for the unfaulted subunit. The correlation with the data (solid line) is clearly much closer when comparing to the unfaulted region. However, there are still some mismatches. In order to understand this, we compare the data to calculations that include only a subset of sites where Si restatoms are directly bonded to Cl absorbates. These class 3, 6, and corner sites in Figure 3.6(b) are summed with weighting factors of 0.4, 0.2, and 0.4 and yield a close match in the lower frame of Figure 3.6(a).

A similar analysis is applied to the Si(111)-(7×7)B:Cl surface and is shown in Figure 3.7(a). Again, the calculated electron intensity for all Si localized sites on the unfaulted

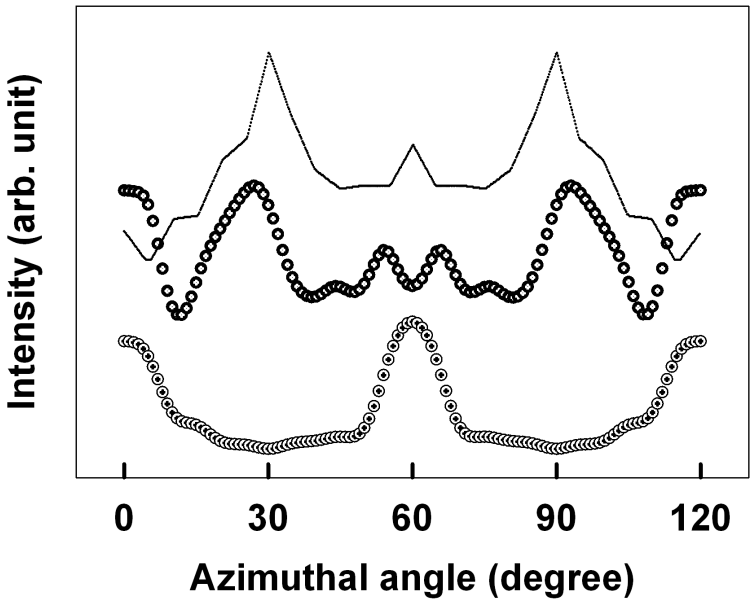

(a) Comparison in Si(111)-(7×7)A:Cl

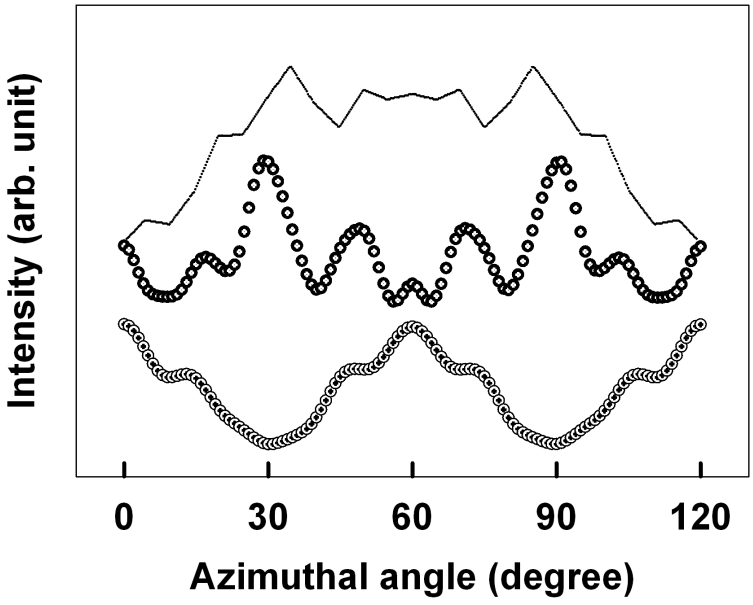

(b) Comparison in Si(111)-(7×7)B:Cl

Figure 3.5: (a) Comparison of calculated electron intensities vs. Cl^+ ion yields from the Si(111)-(7×7)A:Cl surface. The upper small solid line is the experimental Cl^+ ion yield as a function of azimuthal angle. The center plot (dark circle) is the calculated intensity at the Si absorber. The bottom plot (small circle with dot) is the calculated intensity at the Cl absorber. (b) Comparison of calculated electron intensities vs. Cl^+ ion yields in the Si(111)-(7×7)B:Cl surface. The upper solid line is the experimental Cl^+ ion yield. The middle dark circle is the calculated intensity at the Si absorber, and the bottom frame (small circle with dot) is the calculated intensity at the Cl absorber.

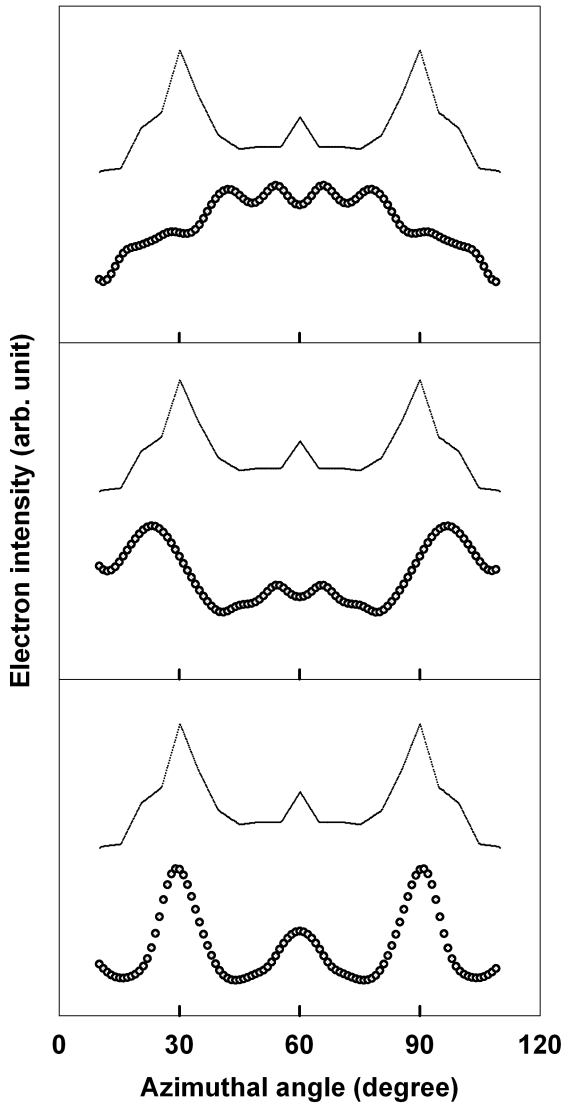

(a) A comparison of DESD from faulted and unfaulted regions of Si(111)-(7×7)A:Cl

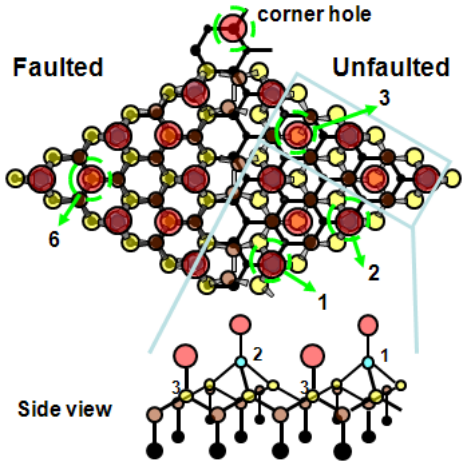

(b) Classes in Si(111)-(7×7)A:Cl

Figure 3.6: (a) A comparison of DESD from faulted and unfaulted regions of Si(111)-(7×7)A:Cl surfaces. The intensities in the calculations (circles) are scaled to match the measured χ-functions (solid line). The upper frame is the comparison to the summation of all localized Si sites on the faulted subunit and the middle frame, the unfaulted subunit. In the lower frame, only classes 3, 6, and a corner hole with the weighting factors of 0.4, 0.2, and 0.4 have been summed. (b) Classification of zones on the Si(111)-(7×7)A:Cl surface.

subunit matches the χ-function. However, like the A surface, there are still some mismatches in the relative peak heights. For example, peaks near 60° are higher than those near 30° and 90° in the calculated intensities, whereas the data is opposite. To explain this, only sites within classes 1, 4 and 5 in Figure 3.7(b), which are located at the edges and central part of the unfaulted region, are summed with an equal weighting. A near perfect match is obtained when allowing a minor contribution from the corner hole and some weak intensity from site 9 in the faulted region. This can be seen in the last frame of Figure 3.7(a). Thus, there appears to be clear site specificity and a propensity for removal of Cl^+ from the unfaulted subunit vs. other regions.

3.4.2 Mechanisms of zone-specific desorption from Si(111)-7×7 surfaces

This observation, in conjunction with the threshold energy of 15 eV, the low Cl^+ velocities [12], and the information on the surface electronic structure [36] provide the basis for deducing the most plausible mechanism(s) involved in DESD of Cl^+ from Si(111) surfaces. The first is based on initial excitation (ionization) of a level with mainly Si 3s character. A hole in the Si 3s level can be filled via Auger cascading primarily from the σ-bonding surface state [33]. The 5 eV gained in the cascade is approximately enough to excite an electron from the surface π-levels to the bottom of the lowest conduction band edge. Ion desorption then occurs due to the hole-hole Coulomb repulsion. Calculations describing the multielectron excited states governing cationic desorption from Cl terminated Si(111) supports these final state assignments [37]. The second mechanism is probably dominant and is based on direct ionization of the σ-bonding surface state. Assuming the initial ESD active sites are not fully negatively charged, 15 eV could lead to removal of Cl^+. Since the σ-bonding surface state partially overlaps the P_z orbital of Si, both mechanisms are consistent with the calculations and DESD data.

The interesting zone and spatial specificity can then be related to lifetime effects in the above mentioned final (surface) states which primarily result from increased strain in the faulted region and a reduced density of states at the Fermi level in the unfaulted region. The strain causes the surface layer in the faulted region to buckle giving rise to Si atoms that are

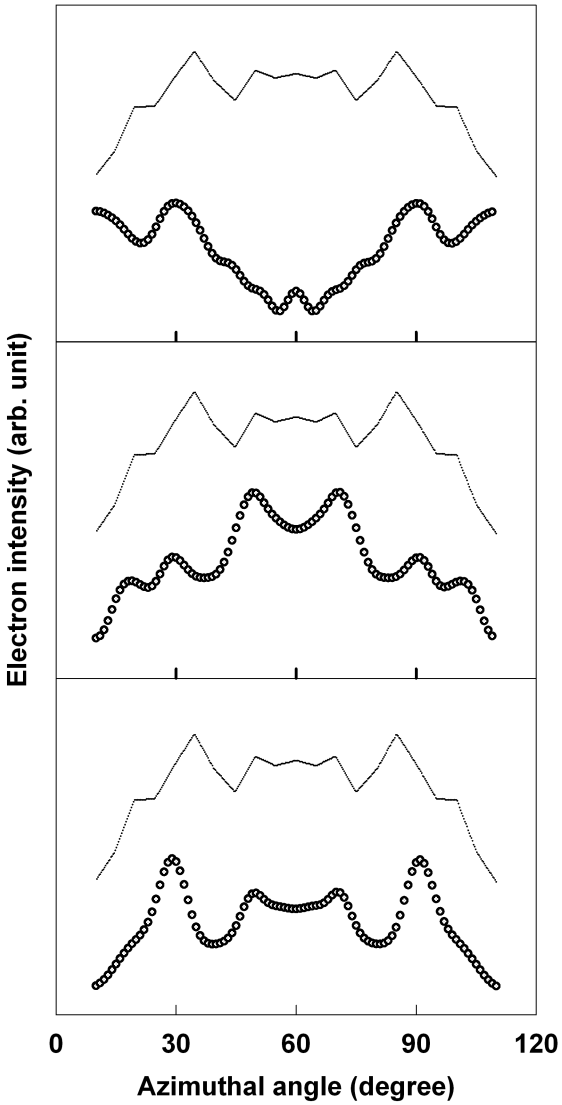

(a) A comparison of DESD from faulted and unfaulted regions of Si(111)-(7×7)B:Cl

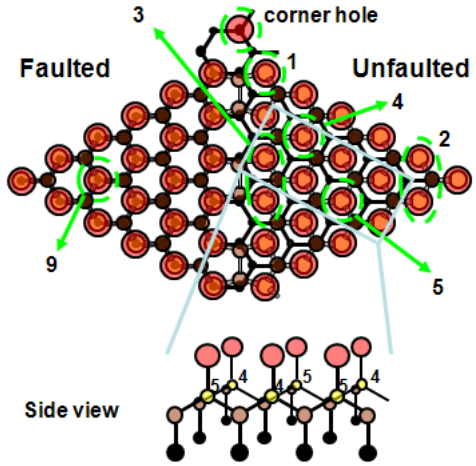

(b) Classes in Si(111)-(7×7)B:Cl

Figure 3.7: (a) A comparison of DESD from faulted and unfaulted regions of Si(111)-(7×7)B:Cl surfaces. The intensities in the calculations (circles) are scaled to match the measured χ-functions (solid line). The upper frame is the comparison to the summation of all localized Si sites on the faulted subunit and the middle frame, the unfaulted subunit. In the lower frame, only classes 1, 4, 5, 9, and a corner hole with the weighting factors of 0.4, 0.2, and 0.4 have been summed. (b) Classification of zones on the Si(111)-(7×7)B:Cl surface.

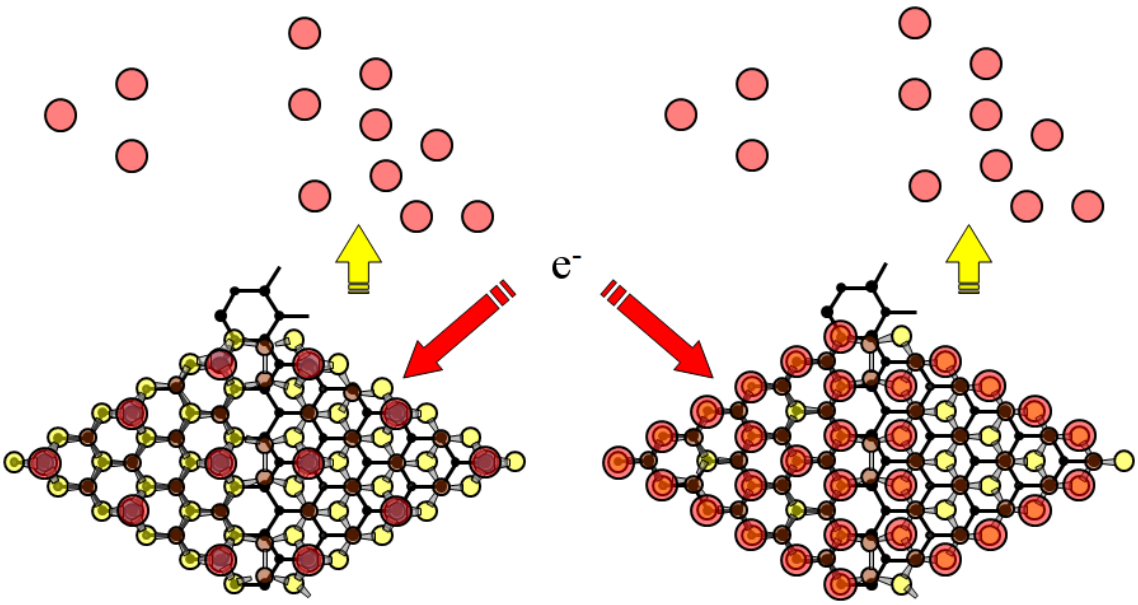

Figure 3.8: Cartoon of zone-specific desorption from Si(111)-(7×7) surfaces. It is revealed in this chapter that low-energy electron irradiation of Cl-terminated Si(111)-(7×7) induces zone and site specific desorption.

higher than those in the unfaulted zone by 0.2 $\AA$ [35]. In the elevated faulted region, surface electronic states localized on the Si-Si back-bond are slightly decoupled from bulk electronic states. Thus, the bandwidths associated with surface electronic states containing significant Si character will narrow. It has been shown that the desorption probability of adsorbates induced from localized holes is associated with the two-hole repulsion energy (U_h) and the bandwidth (ΔE) [38]. When the bandwidth is small compared to the repulsion energy, increased hole localization can occur. In this case, localized holes in Si-Si back-bonds may lead to Si-Si bond breakage but do not induce desorption of Cl^+ or any other cationic products. In addition, three bonds between Si adatoms and Si restatoms in the Si(111)-(7×7)A:Cl surface are distorted so increased hole-hole localization at those sites increases back-bond breakage while inhibiting Cl^+ desorption. Similar hole localization arguments have been given to explain the laser-induced desorption of adatoms from Si(111)-(7×7) [26].

Previous studies of electron stimulated desorption from surfaces containing electronegative adsorbates demonstrated large yield increases due to enhanced lifetimes brought about by reduced screening [1]. This resulted from a reduction of the density of states at the

Fermi level. Since calculations and STM measurements indicate a reduced density of states at the Fermi level in the unfaulted zones of Si(111)-(7×7) [39], screening in this zone will be reduced. Thus, holes in Si-Cl σ-bonding surface states have longer lifetimes so precisely the same effect observed previously can lead to selective removal of Cl^+ from the unfaulted regions.

3.5 Chapter summary

DESD revealed a propensity for Cl^+ desorption from the restatom vs. adatom and the unfaulted vs. faulted zones of the 7×7 reconstructed rest atom area of Si(111). ESD of Cl^+ initially involves states with significant Si 3s and/or Si-Cl σ-bonding character. The spatial selectivity can be related to changes in screening/hole-localization within the unfaulted and faulted regions.

CHAPTER IV

AUGER ELECTRON DIFFRACTION IN EPITAXIAL GRAPHENE ON SIC(0001)

Auger electron diffraction (AED) is used to characterize epitaxial graphene grown on 6H-SiC(0001). Auger spectra for graphene on SiC are taken by changing the outgoing wave relative to the direction of the symmetry axis of the cylindrical mirror analyzer. Auger diffraction effects are revealed by comparing two areas in carbon peaks (2p) of the 1st order derivative spectra. AED of carbon emitters as a function of azimuthal angle shows the six-fold symmetry in addition to some minor structure. As the epitaxial layer grows in thickness, the AED evolves, but still gives the feature reminiscent of the underlying SiC substrate. The quantitative analysis of AED plots with scattering calculations provides insight regarding graphene structure.

4.1 Chapter introduction

4.1.1 Rise of graphene

Carbon-based materials have long been known to form allotropes with different dimension. Zero dimensional form of sp^2 hybridized carbon was discovered in 1985 and named fullerene. Its two dimensional counterpart, carbon nanotube, was also identified 6 years later. Numerous endeavors were dedicated to applying them into real electronic devices, but have not been really successful. In year 2004, another family of sp^2 hybridized carbon species was discovered [40]. It was isolated from highly oriented pyrolytic graphite (HOPG) by applying sticky tape and released onto SiO_2 substrates. Graphene, the two-dimensional sheet of single layer graphitic material, has received widespread interest since then. It is mechanically stable and seems to have high electron mobility. Applications such as a resonator [41] or transport device [42] were reported in order to demonstrate the possibility of graphene based nanoelectronics.

The exfoliated graphene films created by the "tape method" are ideal for scientific

experiments, but, its application will be limited due to low production yield. Therefore, scalable methods to produce graphene are desired. One of these is to reduce graphene oxide which is easily synthesized and isolated due to relatively large interlayer spacing [43]. However, a more industry-compatible and scalable approach may be to grow graphene layers epitaxially on substrates such as Si. It has been long known that graphitic films can be grown on carbides by thermal decomposition and on transition metal surfaces by dosing chemical precursors during substrate heating. Figure 4.1 illustrates these growth methods.

Graphene has a 2-dimensional structure which gives its unique electronic properties. The graphene lattice looks like a honeycomb and its structure is composed of benzene rings. The Bravais lattice is, however, rhombic and based on two vectors. It contains two carbon atoms for a primitive basis. In one carbon, there are 4 valence band electrons. They form sp^2 hybridization so three electrons are involved in σ bonding, but one remaining valence electron is involved in π bonding. Figure 4.2 shows the 2D lattice and bonding structure with neighboring carbon atoms.

For graphene characterization, surface sensitive techniques are applicable in order to probe its ultra-thin 2-dimensional structure. Scanning tunnel microscopy (STM) [44], atomic force microscopy (AFM), and angle-resolved photoelectron spectroscopy (ARPES) [45] are widely used to probe the morphology and electronic structure of graphene surfaces. However, Auger electron diffraction (AED) which is based on low-energy electron scattering has not been introduced into studying graphene yet. In this chapter, AED is used to probe graphene samples epitaxially grown on SiC(0001) substrate.

4.1.2 Auger electron diffraction for surface analysis

AED has been developed as a useful technique that can yield structural information in the near surface region [46]. This technique was applied to study epitaxial growth [47], interface formation [48], and strain in interfaces [49]. Compared to other analytical techniques based on low-energy electrons, AED has some advantages [46]. Outgoing Auger electrons originate from specific atomic emitters so that structural features around those can be probed by

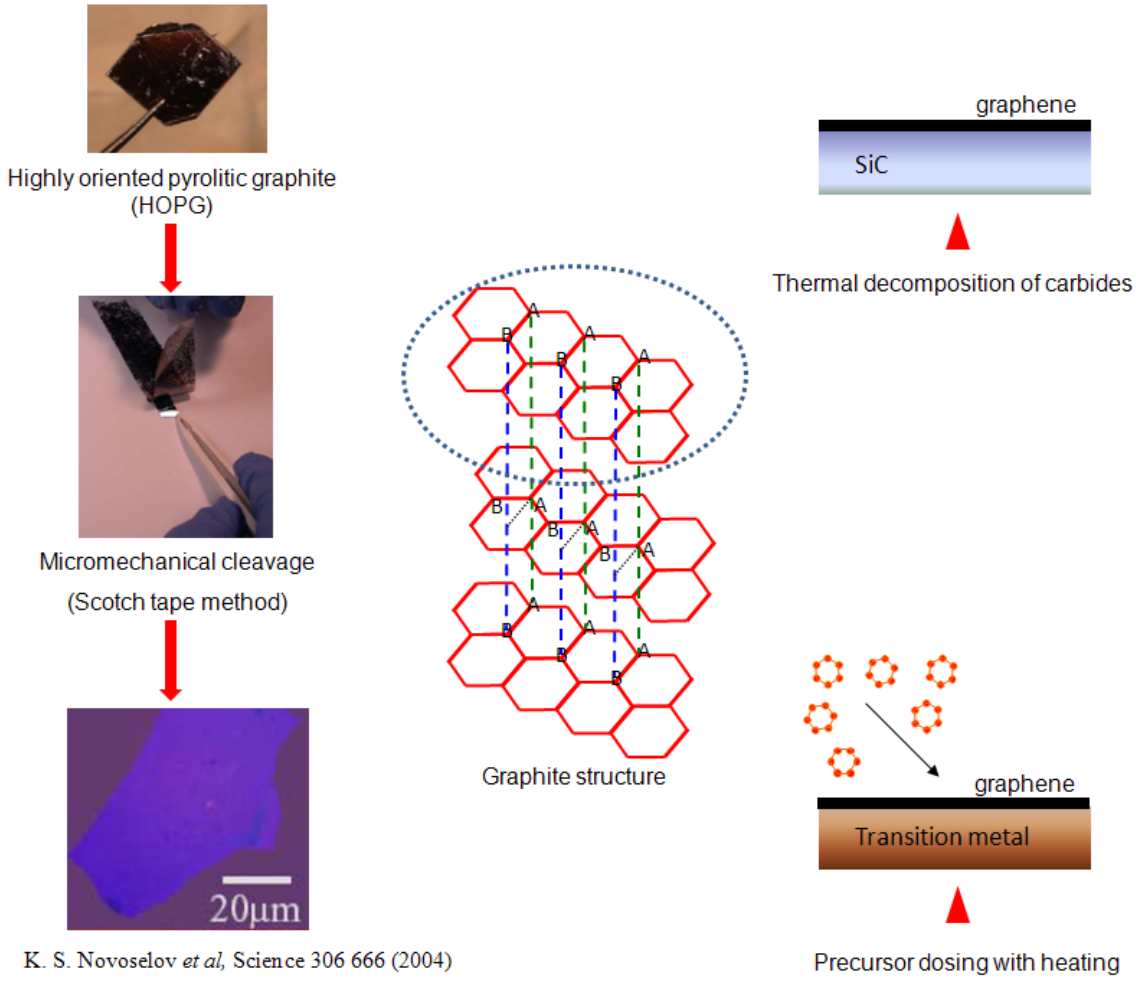

Figure 4.1: Graphene growth methods are illustrated and the graphite crystal structure is presented. The dotted circle surrounds one sheet of the graphite crystal indicating graphene. Note that the A site in one sheet is located on top of the A site in the neighboring sheet. The B site is located on top of the hollow site. The scotch tape method is described in the left side. Thermal decomposition of carbides is illustrated in the upper right and precursor-dosed growth on transition metal surfaces is in the bottom right.

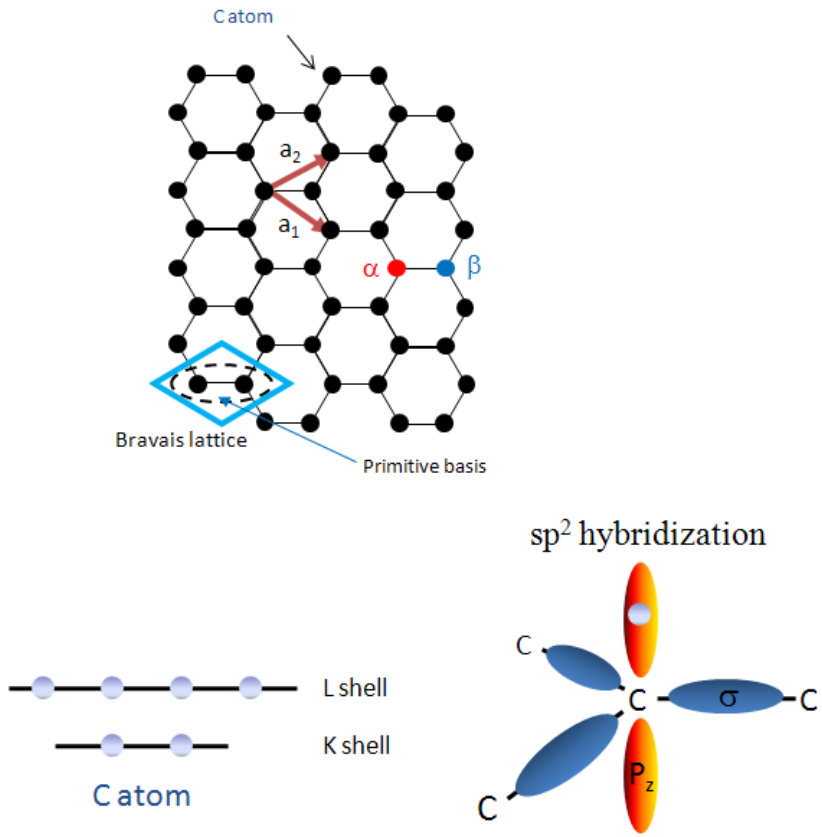

Figure 4.2: 2-Dimensional lattice of graphene and the chemical bonding structures between carbon atoms. The Bravais lattice in graphene is based on a_1 and a_2 lattice vectors. There are two carbon atoms in this lattice. sp^2 hybridization gives three σ and one π orbital from the carbon atoms.

looking at the corresponding energy range. The forward-focusing effect provides a good way for structural analysis by atomic chain detection [50]. Also, only scatterers included in the short range around the emitter effectively influence the diffraction. This implies that non-crystalline samples such as biological materials could be analyzed.

AED usually uses high-energy electrons to excite an Auger process, which gives versatility and control in measurement over photoelectron diffraction (PED). The excitation electron is more surface-sensitive so signal intensity is generally high. However, initial and final-state effects matter simultaneously in AED so the result is complicated and difficult to analyze. In this thesis, a treatment of angle-resolved Auger spectra is made to extract mainly final-state effects which are determined by outgoing Auger electron diffraction. Then, calculations using single scattering theory are compared to the AED experimental results to obtain insight regarding structural information of epitaxial graphene grown on the SiC(0001) substrate.

4.1.3 Principle of Auger electron diffraction

Auger electron emission is a three step process. At first, an incident high-energy electron collides with the surface and excites a core level electron, which leads to the creation of a core hole. Then, this core is filled with an electron via Auger decay. During this step, electron correlation leads to the ejection of an Auger electron with a well defined kinetic energy. Figure 4.3 illustrates the three step mechanism of Auger electron emission. However, three steps are not the end of Auger emission. The outgoing Auger electron goes through various different emission paths and can undergo elastic scattering and be diffracted.

4.2 Auger electron diffraction in epitaxial graphene on SiC(0001)

4.2.1 Experiment

Auger electron spectroscopy is carried out in an UHV chamber. The sample holder can be translated through the z-axis and tilted so that it can be located in front of multiple different analyzers. This chamber is designed to implement angle-resolved measurements for surface analysis. The sample holder is rotatable, which provides orientation of the azimuthal angle. The tilted motion of the sample holder also allows control of the polar angle. This

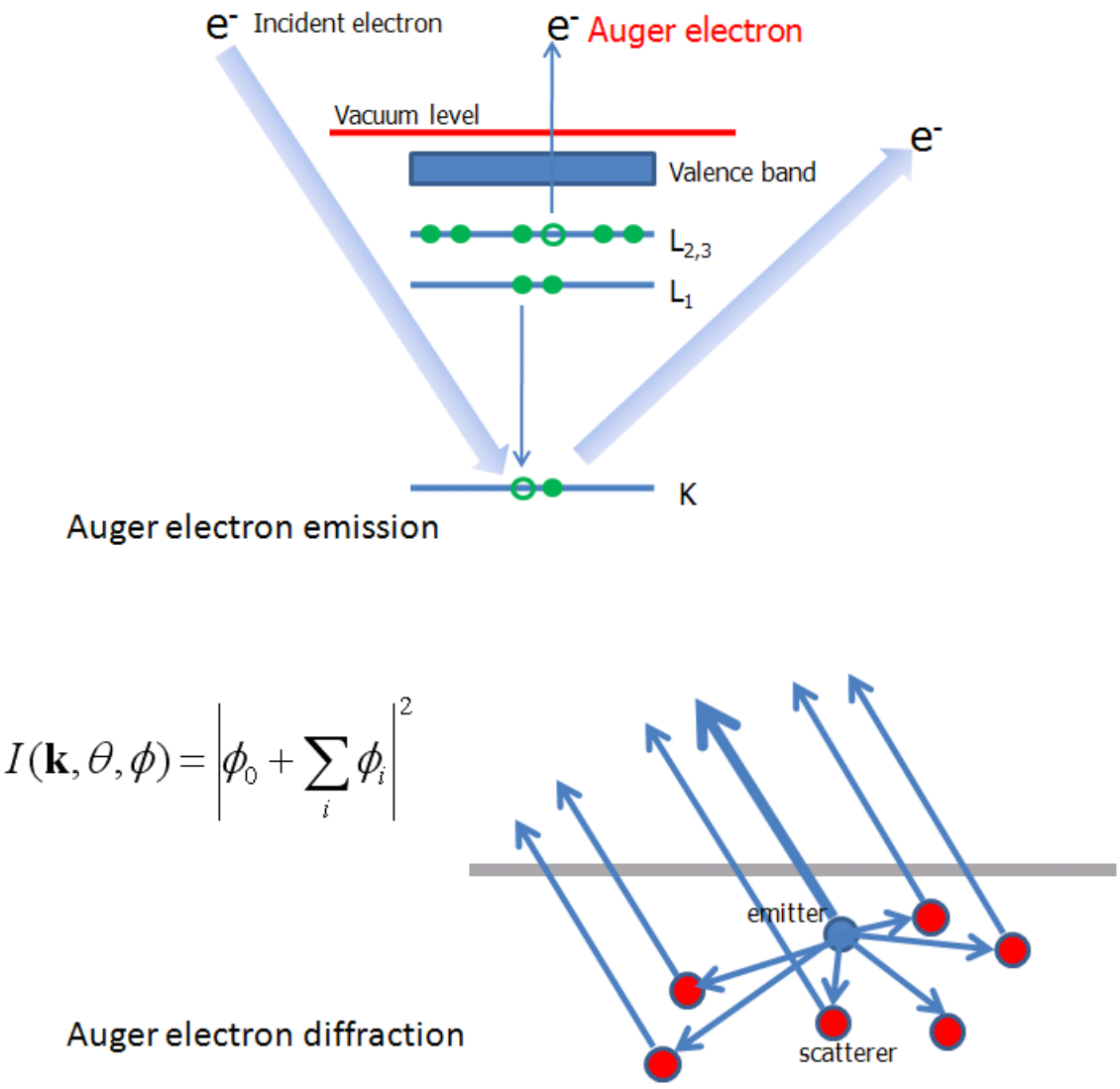

Figure 4.3: Auger electron emission and diffraction are illustrated.

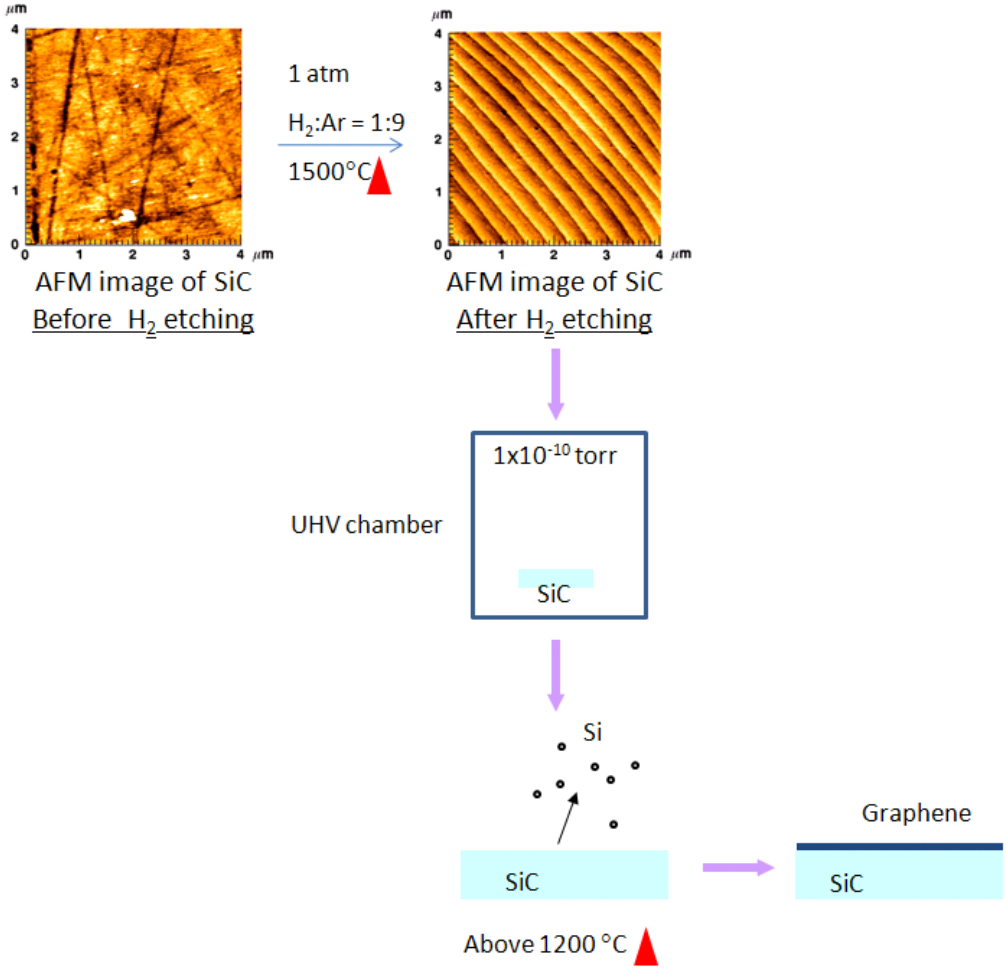

Figure 4.4: Steps for graphene preparation on SiC substrates is presented. The two AFM images show the different surface morphology of SiC before and after the hydrogen etching procedure. The sample is then transferred into an UHV chamber and annealed at more than 1200 °C. The grown graphene films are analyzed with Auger electron spectroscopy for thickness determination.

chamber also has a sample transfer system with a magnetically coupled transfer arm, a multi-motion wobble stick, and an electron bombardment heater. Through the transfer system, a hydrogen etched SiC(0001) substrate mounted on a molybdenum platen with a center hole can be transferred from atmosphere into the UHV main chamber. The substrate is then heated via electron bombardment with high energy electrons to above 1200°C for growth of epitaxial layers. The temperature of the SiC surface is measured by a calibrated infrared pyrometer. The procedure for sample preparation is briefly illustrated in Figure 4.4.

After epilayer creation, the sample is moved and mounted onto the rotation sample holder for angle-resolved Auger spectroscopy. The distance between the sample surface and the cylindrical mirror analyzer entrance is adjusted by scanning the elastic peak of excitation electrons. The sample center point is carefully aligned onto the irradiation spot from the electron gun located through the symmetry axis of the double-pass cylindrical mirror analyzer (DPCMA). This is done repeatedly in order to keep the consistency of sampling during Auger electron spectroscopy during angle-dependent measurements. The picture of the DPCMA mounted on the UHV chamber is shown in Figure 4.5. For calculating the thickness of graphene epilayers on SiC(0001), 0° polar angle which is the angle between the surface normal and excitation electron direction, is used for Auger spectroscopy.

Angle-resolved Auger spectroscopy is carried out by taking an Auger electron energy-scanned spectrum at a specific azimuthal angle. Then, the next energy-scanned spectrum is taken after the sample is rotated azimuthally. During this measurement, the polar angle is fixed. Therefore, an angle-resolved Auger measurement consists of Auger spectra in a range of azimuthal angles at a fixed polar angle. Azimuthal angle-resolved measurements are carried out also with other polar angles.

4.2.2 Extraction of diffraction information from Auger electron spectra

In order to extract diffraction information from the Auger spectra, the ratio of two peak intensities in each spectrum is plotted as a function of azimuthal angle. Because the Auger spectrum is actually the convolution of electronic and structural information, angle-dependent measurement of Auger electrons can give geometrical or structural information.

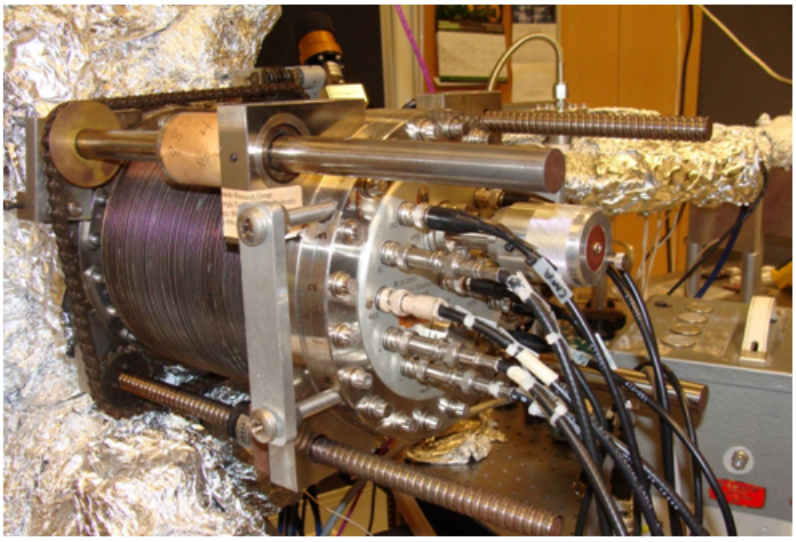

Double-pass cylidrical mirror analyzer

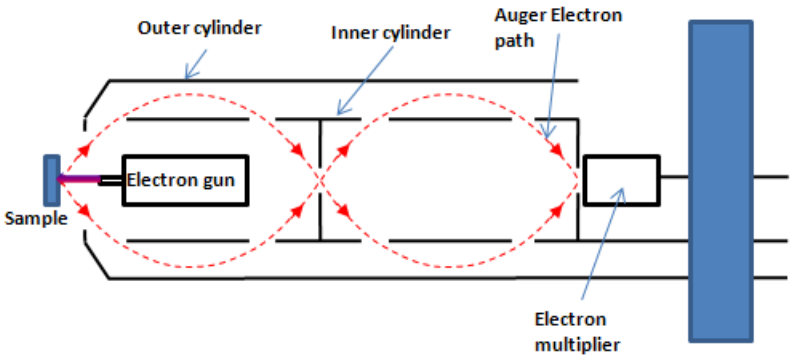

Ilustration of Auger electron collection

Figure 4.5: The picture of the double-pass cylindrical mirror analyzer (DPCMA) is presented and the Auger electron collection and detector are illustrated.

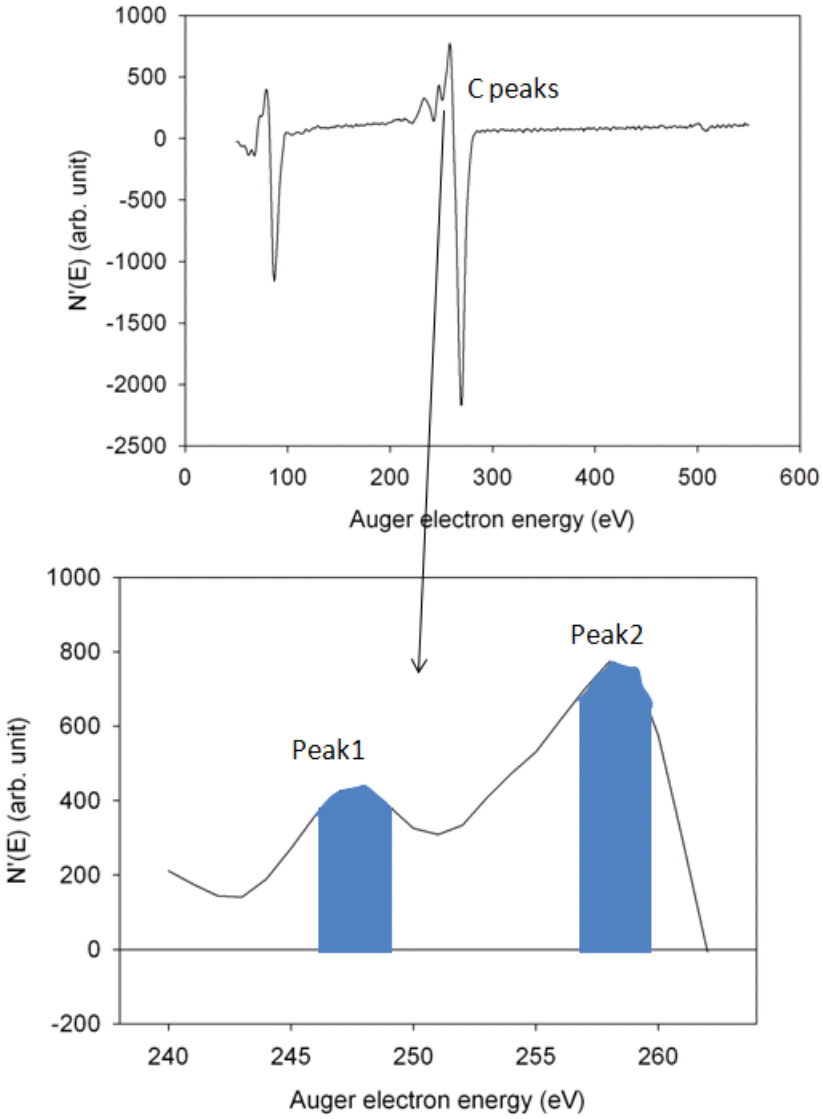

Figure 4.6: The derivative Auger electron spectrum of graphene on SiC(0001) is presented. Part of the Auger spectrum is magnified for C regions. Two different areas in the C regions are integrated and compared. Each Auger spectrum is carried out for a specific azimuthal and polar angle of incidence.

The shape of the Auger spectrum changes as the detection angle varies. The way to extract structural information from Auger spectra is illustrated in Figure 4.6.

The ratio of two regions in each Auger spectrum does not give any information until it is plotted as a function of azimuthal angle. The plot of the area ratio is presented in the upper frame of Figure 4.7. As clearly seen, we can see periodicity with a 60 degree oscillation. However, a rising background is also observable. This background function can be calculated by assuming a quadratic function. This function is then subtracted so we can obtain a χ-function which gives the percent error of data fluctuation relative to the background. In the lower frame in Figure 4.7, the χ-function of the area ratio is plotted.

The Auger diffraction information obtained by this peak comparison method can be strengthened by carrying out the measurement at several different polar angles. Then, we have a complete picture of Auger electron diffraction for a specific atomic emitter located at the surface region. In order to understand the evolution of Auger electron diffraction features, χ-functions of the peak area ratio with various polar angles are plotted as a function of azimuthal angle. We focus on the carbon emitters which exist through all the layers of samples.

4.2.3 Sampling of graphitic epilayer on SiC(0001)

Three different samples are prepared for Auger electron diffraction studies. The derivative Auger spectra of these samples taken with zero-polar angle are presented in Figure 4.8. These spectra are normalized to the carbon peak. It is clear that the Si peak becomes weaker as the epilayer becomes thicker. These Auger spectra and the C:Si ratio is used to determine the graphene overlayer thickness.

4.3 Calculations of Auger electron diffraction in epitaxial graphene

4.3.1 Formalism

The collected Auger electron intensity originates from an emitter located at $\mathbf{R}_e$. The intensity at the emitter site is formed by interference of the directly outgoing electron wave with components elastically scattered by the near-surface atoms. Like the case of DESD, spherical-wave effects should be taken into account for calculating the Auger intensity from

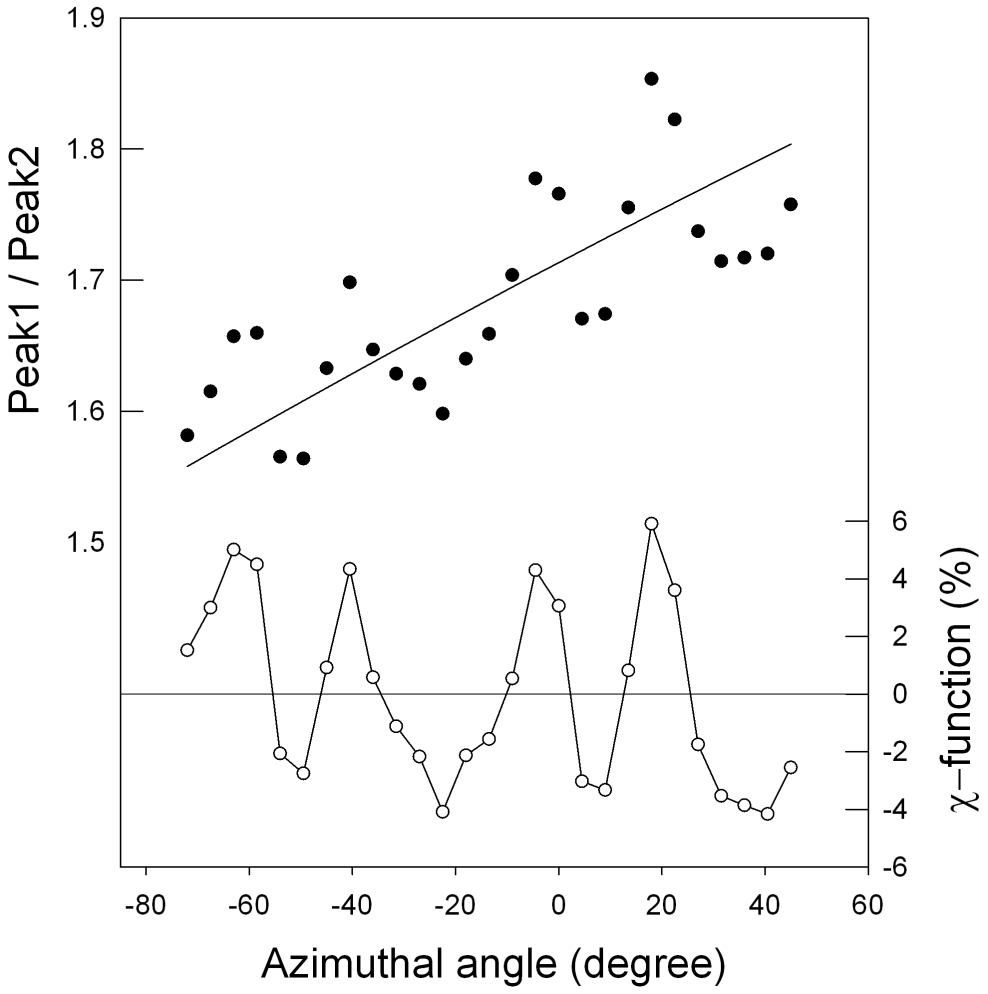

Figure 4.7: The ratio of two areas in each Auger spectrum is plotted as a function of azimuthal angle of measurement. For each plot, the polar angle of incidence is fixed. The straight line is the background and is subtracted from each point to yield the χ-function.

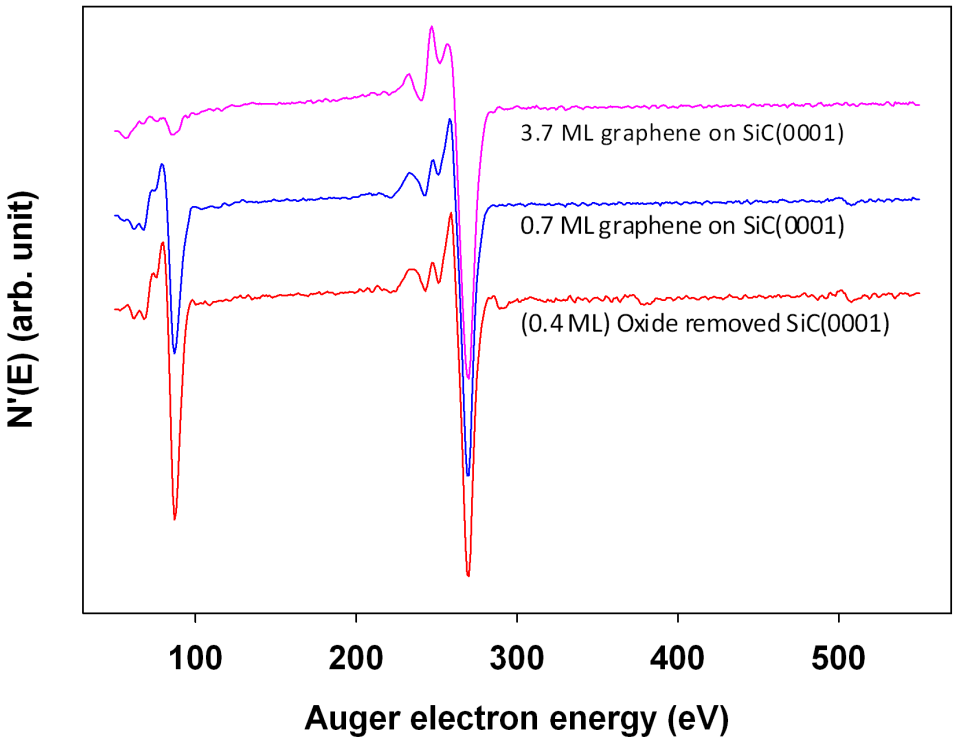

Figure 4.8: Derivative Auger spectra for three graphitic samples. The red plot is the spectrum of oxide-removed SiC(0001) substrate. The blue plot is that of graphitic sample calculated as 1.6 ML. The purple plot is that of graphitic sample calculated as 3.7 ML.

the emitter located in the sample surface. The formalism presented in chapter 2 is referred to again for AED calculations.

The wavefunction perturbed by final-state effects (i.e. equation 25) is used to calculate electron intensity due to Auger electron diffraction. The second term in the right-hand side of Eq. (25) is the first-order scattered components from the position $\mathbf{r}$ and can be rewritten as

$$\phi^1(\mathbf{r}) = \sum_j \mathbf{M}_{00}(\hat{\mathbf{k}}, \vec{\rho}_{j\mathbf{r}})\mathbf{P}_{00}(\vec{\rho}_{j\mathbf{r}})\frac{e^{i\rho_{j\mathbf{r}}}}{\rho_{j\mathbf{r}}}e^{-i\mathbf{k}\cdot\mathbf{R}_j}. \tag{29}$$

Compared to Eq. (26), introduction and termination matrices are redefined. Here, the introduction matrix is $\mathbf{P}_\lambda(\vec{\rho}_{j\mathbf{r}}) = \Gamma^{00}_\lambda(\vec{\rho}_{j\mathbf{r}})$ and the termination matrix is $\mathbf{M}_\lambda(\vec{\rho}_{j\mathbf{r}}, \hat{\mathbf{k}}) = \sqrt{4\pi}\sum_L Y_L(\theta,\phi)t^j_l\tilde{\Gamma}^L_\lambda(\vec{\rho}_{j\mathbf{r}})$. This is a specially defined scattering matrix which describes scattering of outgoing Auger electrons by one of the scatterers into the detector located far away from the surface. The introduction matrix represents the process of leading the emitted electron from the emitter into the one of the scatterers. For first-order components, however, the introduction matrix is redundant because λ is $(0,0)$. These matrices will be useful when higher-order terms are used in the calculations.

The Debye-Waller factor, $W(T)$ and the inelastic scattering effect should be also incorporated like we did in DESD. Thus, the total first-order scattering component for the emitter located at position $\mathbf{r}$ becomes

$$\phi^1(\mathbf{r}) = \sum_j \mathbf{M}_{00}(\hat{\mathbf{k}}, \vec{\rho}_{j\mathbf{r}})\mathbf{P}_{00}(\vec{\rho}_{j\mathbf{r}})\frac{e^{i\rho_{j\mathbf{r}}}}{\rho_{j\mathbf{r}}}e^{-i\mathbf{k}\cdot\mathbf{R}_j}W_j(T)e^{-|\frac{\rho_{j\mathbf{r}}}{\mathbf{k}}|/2\Lambda}. \tag{30}$$

We then use this equation to calculate $I \propto \psi^*(\mathbf{R}_e)\psi(\mathbf{R}_e)$ as a function of the outgoing electron $\mathbf{k}$-vector. In order to calculate the intensity, the calculated result of Eq. (30) should be summed with the nonscattered component. This can be calculated by taking into account inelastic decay effects for the first term in the right-hand side of Eq. (25).

4.3.2 Calculation details

The DPCMA used for collecting Auger electrons is not originally designed to measure angle-resolved Auger spectroscopy. It has an angular aperture which should be considered for quantitative analysis. In order to account this for the calculations, Auger electron

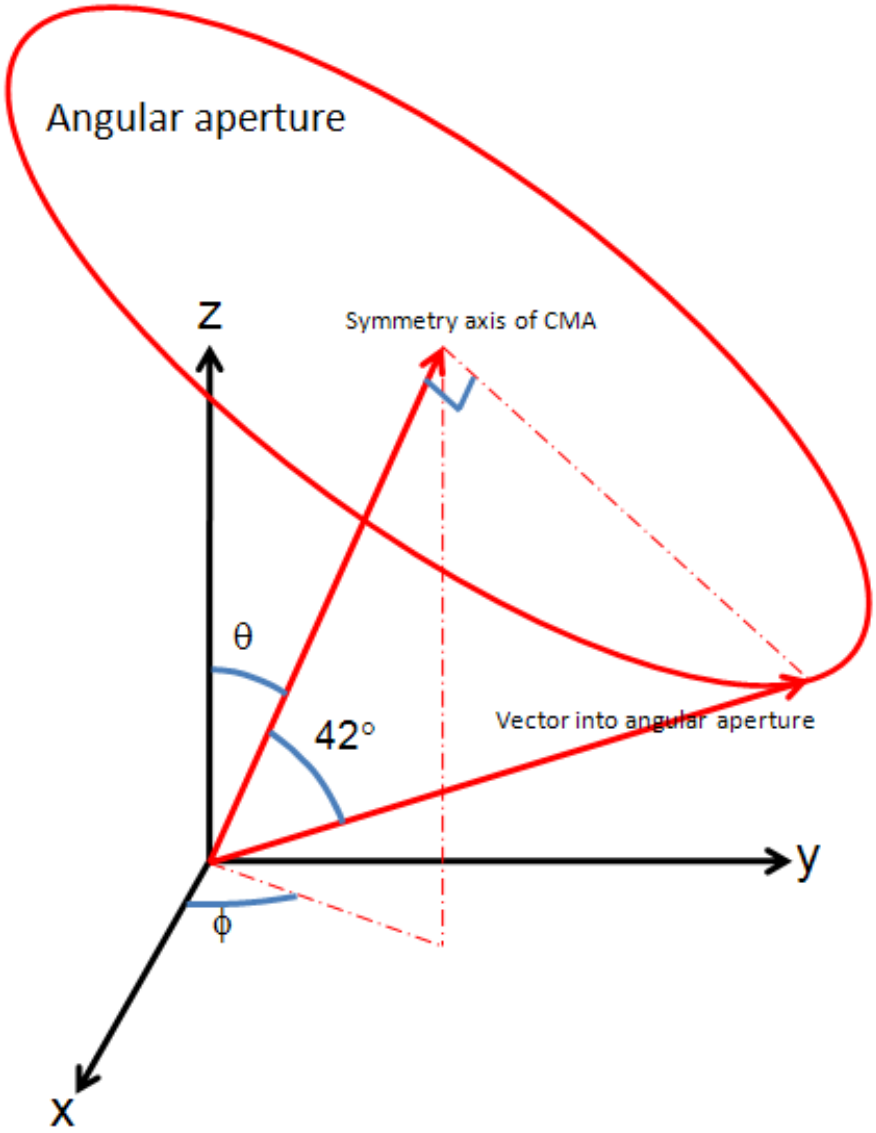

Figure 4.9: Angular aperture around the symmetry axis of the CMA. The symmetry axis has the direction of (θ, ϕ) corresponding to the polar and azimuthal angle in AED measurements. The circle which is normal to the symmetry axis represents the angular aperture of Auger electron entrance into the CMA. The vector drawn to the circle is one of the paths of Auger electrons which is going to be detected at the corresponding angular direction (θ, ϕ) during the measurement. The angle between the axis and the vector is 42° which is the parameter of the Physical Electronics 15-255G DPCMA.

k-vectors are generated around the symmetry axis of the CMA. The angle between the symmetry axis and the vectors is 42°. Figure 4.9 shows how the angular aperture is created for the calculations. For calculating the Auger electron intensity at a specific angle-resolved measurement with (θ, ϕ), 60 vectors are used around a 360° angular aperture. Auger electron intensity with each exit vector into the CMA is calculated and summed to give the total intensity. I mention here that even though 60 vectors are used, it is just due to limit of computation. More vectors for the angular aperture will produce better results.

For the oxide-removed 6H-SiC substrate, the Si-terminated 6H-SiC(0001) structure is used for generating the cluster geometry. Around the chosen Auger emitter, atoms inside a 10 Å radius sphere are used as scatterers. The atoms present down to the third bilayer are sampled for calculating the Auger electron intensity. For 3.7 ML graphene on a Si terminated SiC(0001) sample, the graphite structure is used for the cluster. The 10 Å radius cluster is used for scattering. Two different carbon atoms in one unit cell are taken from each graphene sheet to represent Auger electron emitters. Emitters present in the uppermost three graphene sheets are taken for calculating one Auger electron intensity.

In order to calculate the peak ratios, a semi-theoretical approach is used. Auger spectra with zero polar angle is taken and its non-derivative form is used to give the value for 245, 250, 255, and 260 eV. Then, the calculated intensity at each energy is multiplied and this result at 250 eV is subtracted by that at 245 eV, which gives the 1^{st} peak intensity on the derivative Auger spectrum. The 2^{nd} peak intensity is obtained by the result at 260 eV subtracted by 255 eV. The ratio of those peak intensities is plotted as a function of azimuthal angle for a specific polar angle.

4.4 Quantitative analysis of Auger electron diffraction effect

4.4.1 Comparison between the experiment and calculation

Plots of two peak ratios reflecting the diffraction effects in the carbon emitter from the clean SiC(0001) substrate are compared with the calculated Auger electron intensities as a function of azimuthal angle with polar angles ranging from 20 to 45 ° in Figure 4.10. For experimental AED plots, we observe some common features. The most noticeable

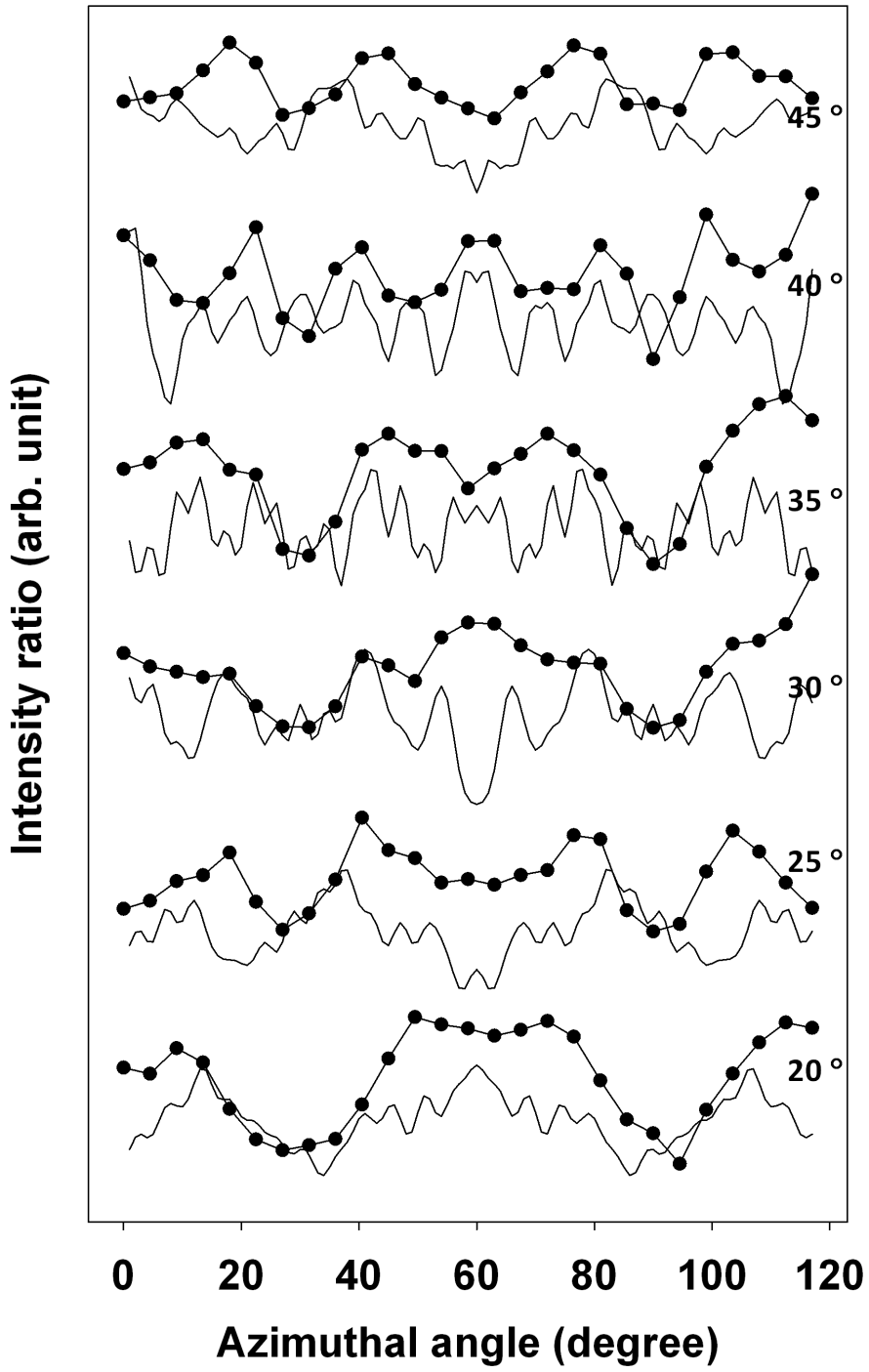

Figure 4.10: AED plots (lines with points) for the carbon emitter in the SiC(0001) substrate and calculated Auger electron intensities (solid lines) as a function of azimuthal angle at polar angles ranging from 20 to 45 °. The AED plots and calculated intensities with the same polar angle are compared.

feature is valleys at 30 and 90°. The other feature is 6-fold symmetry. All plots show similar periodicity with a 60 degree period. Actually, there is slight deviation from 6-fold symmetry. The SiC(0001) surface is 3-fold symmetric, but due to its bilayer structure, quasi-6-fold symmetry should be reflected in plots with Auger diffraction. Therefore, we can assume at this moment that the symmetric feature shown in these plots is induced by the surface geometry in SiC(0001).

Matching between the experimental results and calculations is only good at low polar angles (20 and 25°) which corresponds to next normal incidence. Their valleys and peaks are located closely at azimuthal angles. For the case of higher polar angles, it is difficult to correlate the AED features with the calculations. However, as can be seen in 40°, there are shared feature and roughly half of the experimental features can be correlated with the calculated intensities.

Figure 4.11 shows AED plots for a graphene grown on a SiC(0001) substrate. The epilayer thickness on SiC(0001) was calculated to be 0.7 ML from the Si (2p) and C peak (2p) ratio in the Auger spectrum taken with zero polar angle. The valley feature at 30 and 90 ° in the plots of SiC substrates are also observed in the thin graphene sample and the 6-fold like feature is also present in AED plots. Generally speaking, these plots are quite similar to the clean (i.e. oxide removed) SiC(0001) data.

The similarity of AED features in thin graphene grown on SiC can be understood in terms of the presence of buffer layer between the reconstructed SiC substrate and epilayer. During the oxide removal step, a carbon-rich buffer layer is also grown on top of the SiC substrate. Therefore, the surface reconstruction inhibits the direct investigation of SiC surface. This implies that the AED plots of 0.7 ML sample are coming from the reconstructed SiC and buffer layer. The contribution from the graphene layer is small. In fact, the calculated thickness of 0.7 ML graphene epilayer may be close to the buffer layer thickness and not discernible using AED.

We also studied the AED of a 3.7 ML graphene epilayer on SiC(0001). These AED plots are compared with the Auger electron intensity calculated using graphite coordinates in Figure 4.12. If we look at the experimental AED plots, the results show many changes

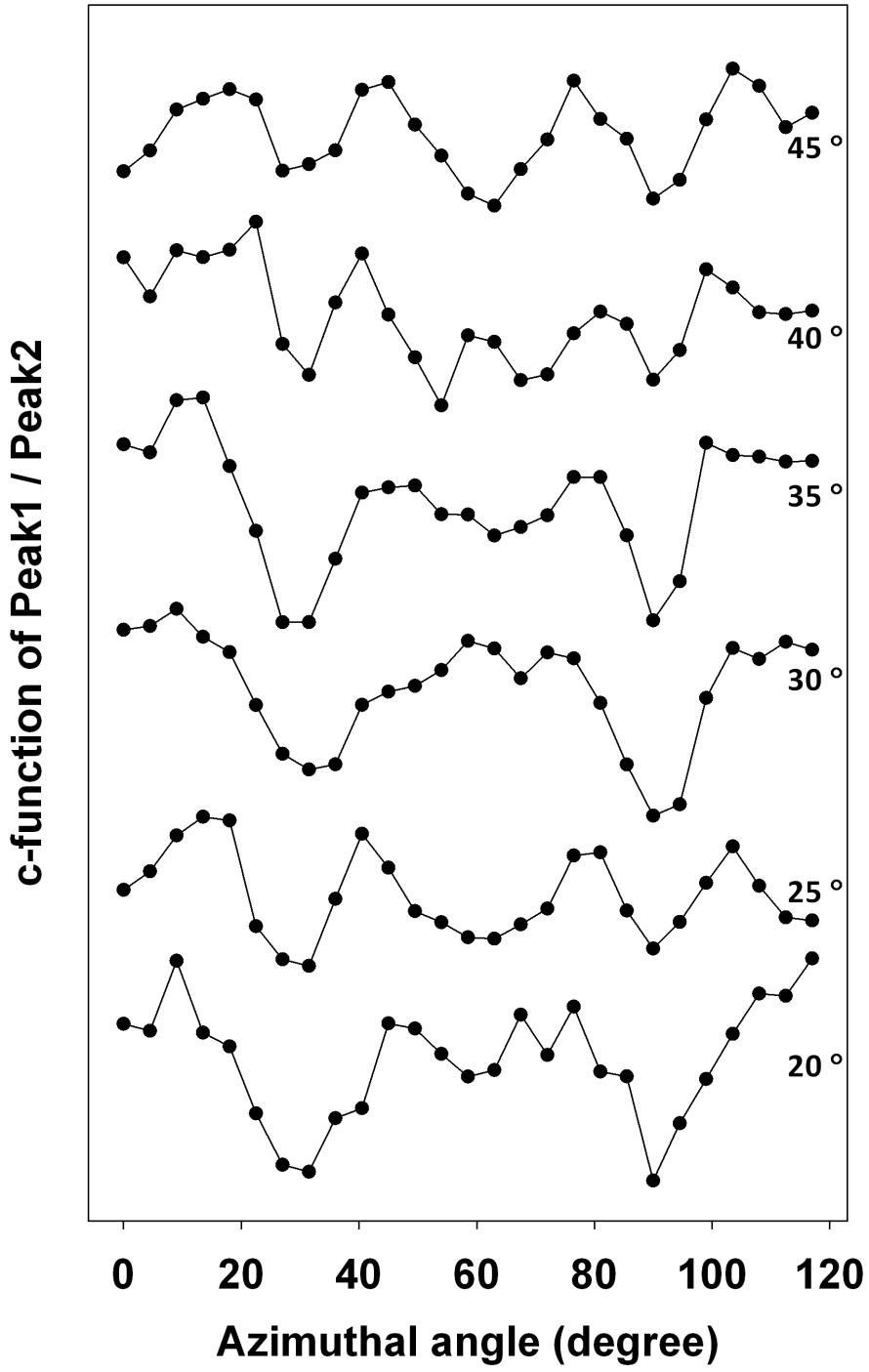

Figure 4.11: AED plots (lines with points) for the carbon emitter in 1.6 ML graphene on SiC(0001) as a function of azimuthal angle. Data points in each plot are obtained for polar angles ranging from 20 to 45 °.

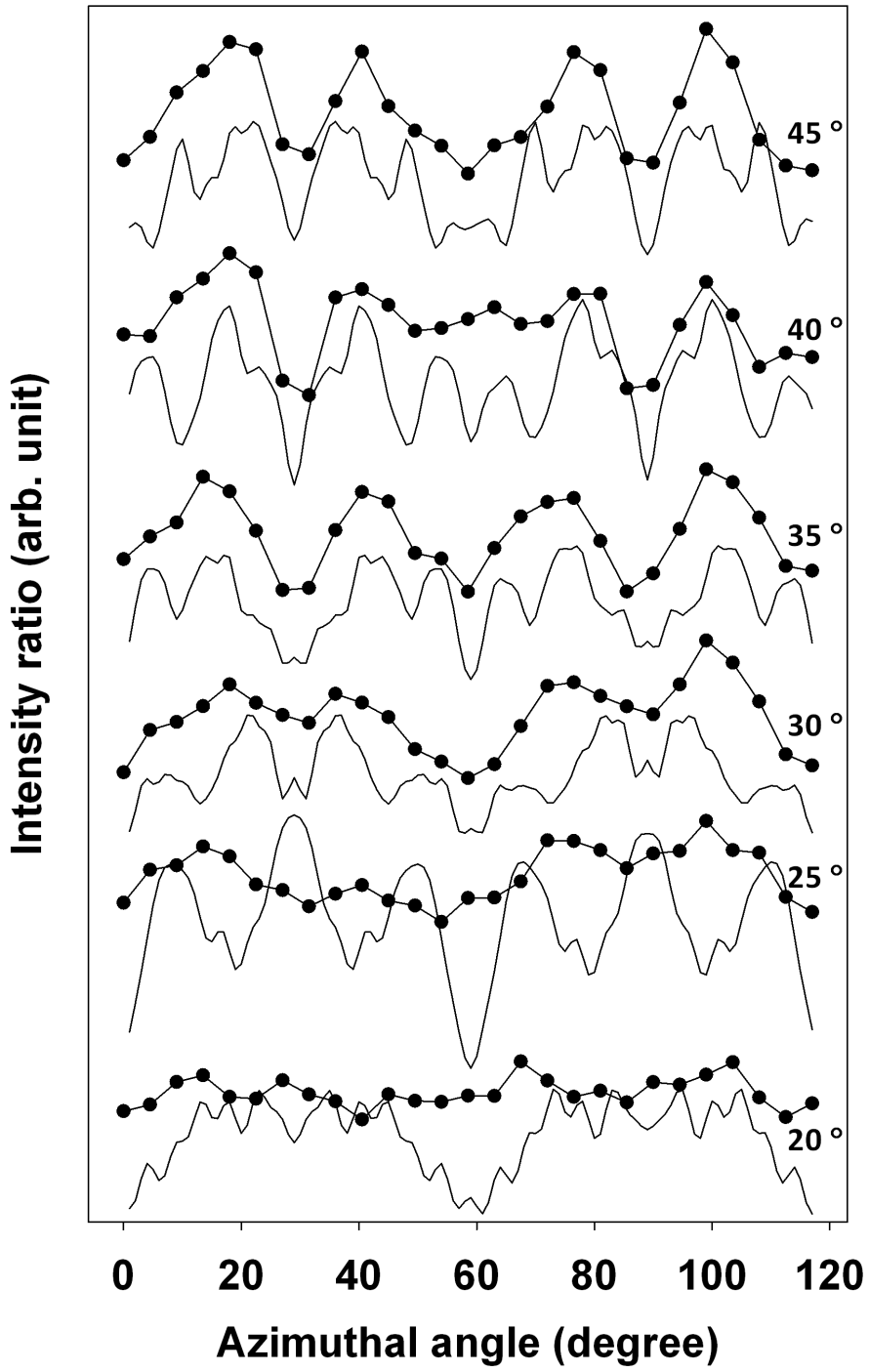

Figure 4.12: AED plots (lines with points) for the carbon emitter in 3.7 ML graphene grown epitaxially on SiC(0001) and calculated Auger electron intensities as a function of azimuthal angle with polar angle from 20 to 45°. The AED plots and calculated intensities with the same polar angle are compared.

compared to the clean SiC and the 0.7 ML graphene on SiC sample, which can be expected from thick graphitic epilayers. We still can observe the valley structures around 30 and 90°. They seem to be inherited from the valley structure at 30 and 90° in two previous samples. They also show quasi-6-fold symmetry. Another feature noticeable is weak fluctuation of intensity ratio in plots of lower polar angle (20, 25, and 30°). Overall features in the plot of 45° polar angle are similar to those in thin graphene samples or clean SiC, but in detail, some variations are detected. HOwever, the 35° polar angle plot has a valley around 60° that is deeper than that of other samples. For the 40° plot, the area between 30 and 90° becomes higher and the fine structure gets weaker. Another interesting thing in this plot is that it deviates from 6-fold symmetry.

4.4.2 Discussion

The calculated Auger electron intensity is corrected for the angular aperture acceptance and also for the angular dependence of the energy deposition. For the SiC(0001) substrate, the calculations show agreement with data taken with low polar angles. In contrast, the study of 3.7 ML graphene gives reasonable agreement only at high polar angles. These results give insight concerning the epilayer structure. As suggested by the Raman study described in chapter 5 of this thesis, the graphitic epilayer grows on top of a carbon-rich buffer layer. The AED features extracted from the angle-resolved Auger measurement reflect this heterogeneous structure.

In the clean SiC study, the acceptable correlation at 20 and 25° polar angle indicates that most of the features present in AED plot originates from the reconstructed SiC substrate. As the polar angle of measurement becomes higher, the contribution from SiC layers below the buffer layer becomes less due to increased attenuation length. Therefore, the AED data is not well described in the calculation. The AED data for 0.7 ML graphene grown on SiC(0001) is ostensibly the same as the clean surface. This indicates that the graphene overlayer is largely in registry with the underlying buffer layer.

These AED aspects are more obvious in 3.7 ML graphene sample. As mentioned, plots of high polar angle are correlated with calculations better than those of low polar angle.

It indicates that Auger electrons mostly originate from the graphene overlayer due to the increased attenuation length. Noticeably, the valley structure at 30 and 90° with 30 ∼ 45° polar angle is reproduced by the calculations rather well. The overall correlation is related to the presence of graphitic layers on the SiC surface. The valley structure may be also induced by the 6-fold symmetry of the buffer layer which is inherited by graphene epilayers.

Overall, the AED intensity calculations provide better quantitative analysis of the 3.7 ML sample than that of the clean SiC sample. Intuitively, we can expected this result. The buffer in the 3.7 ML sample is located below graphene layers so the affects on the AED data are weaker than that in reconstructed SiC or thin epilayer sample. The buffer is created during graphene growth and it mediates the lattice matching to release stress for both the substrate and epilayer. Its structure and element composition are not clear yet. However, we note that the reconstructed graphene unit cell is based on $6\sqrt{3} \times 6\sqrt{3}$R30° structure. Auger diffraction effects seems to show the signature of the buffer layer. However, the structural details of the buffer layer and related aspects need to be analyzed more.

4.5 Chapter summary

Angle-resolved Auger spectroscopy is used to analyze the structural properties of epitaxial graphene films created on 6H-SiC(0001) substrates. A method for extracting the Auger diffraction induced by final-state effects is devised and gives insight concerning the buffer layer and the heterogeneous graphene structure. It provides useful information about the buffer presence and its nature. The comparative studies for three samples proves that Auger electron diffraction can be a useful probe of analyzing the ultra-thin epitaxial grown film.

CHAPTER V

RAMAN SPECTROSCOPY OF EPITAXIAL GRAPHENE ON SIC(0001)

Epitaxial graphene is characterized with Raman scattering spectroscopy. Raman spectra are obtained for epitaxially grown graphene films on 6H-SiC(0001). Three intrinsic Raman bands of graphitic species are observed and show an interesting evolution as the film thickness grows. For the Raman 2D-band (overtone of the D-band and also known as the G′ band), the intensity increases for samples with a mean thickness of more than 2.5 graphene-equivalent layers. The information gleaned from Raman spectra is well correlated with scanning tunneling microscopy (STM).

5.1 Electronic properties of graphene

5.1.1 Graphene characterization

The electronic structure of graphene is induced by the 2-dimensional lattice. Its reciprocal lattice looks very similar to the real-space lattice. Near the Fermi energy, the valence electron energy is linearly proportional to the electron momentum so the electronic structure at this region is called a Dirac cone. Two Dirac cones exist at K and K′ points in the first Brilloin zone of graphene. Figure 5.1 explains how the first Brilloin zone is created and describes the low-energy structure around it. The upper limit of filled states in the Dirac cone is the Fermi level.

For graphene characterization, surface sensitive techniques such as scanning tunneling microscopy (STM), angle-resolved photoelectron spectroscopy (ARPES), and atomic force microscopy (AFM) are widely used to reveal the morphological and electronic properties. Even though those tools are very useful to probe graphene properties, however, they are generally low-throughput techniques. As part of an effort to develop high-throughput and non-invasive techniques, Raman spectroscopy was introduced to analyze properties of graphene and few layer graphene (FLG) layers [51]. This versatile technique could provide

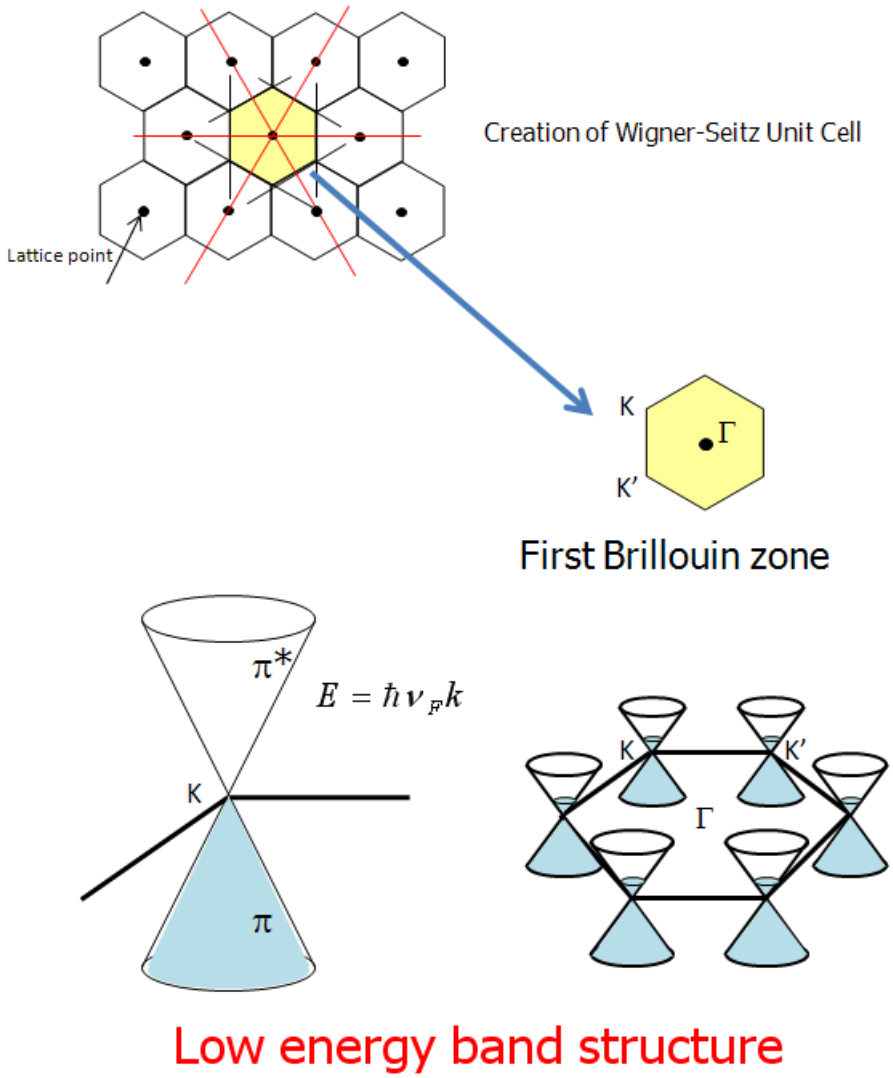

Figure 5.1: Reciprocal lattice of graphene in momentum space is used to create the first Brilloin zone. The Wigner-Zeitz unit cell corresponds to the first Brilloin zone and the electron structure in the first Brilloin zone is plotted. The blue colored volume in each Dirac cone represents the filled state.

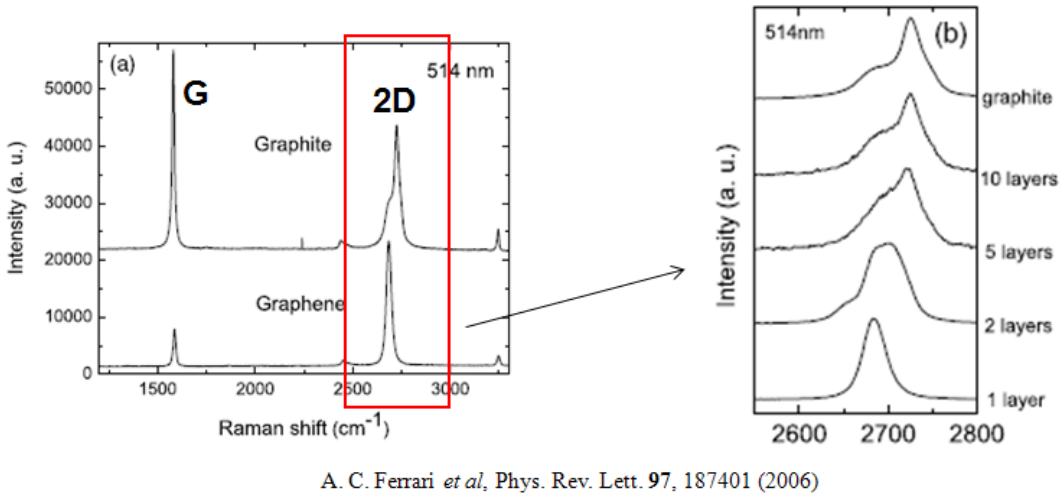

A. C. Ferrari *et al*, Phys. Rev. Lett. **97**, 187401 (2006)

Figure 5.2: Raman spectra of graphene prepared by the scotch tape method are presented.

important information concerning geometric and electronic properties of FLG [52].

5.1.2 Raman scattering in graphene

Raman studies revealed graphene signatures relative to bulk graphite [51]. In exfoliated graphene, two intense peaks are observed. One is located around 1582 cm^{-1} and other one is around 2700 cm^{-1}. Figure 5.2 shows the Raman spectra of graphitic species prepared by the scotch tape method. The first peak is called the G peak. The second is historically called the G$'$ peak. It is actually the 2^{nd} order D peak. Both peaks also occur in the Raman spectrum of graphite. However, their relative intensities are different in graphene and graphite. The ratio of the G peak to the 2D peak in single layer graphene is lower than in graphite. The intensity of peak in single graphene sheet is strong enough to be comparable to that of graphite and the shape of 2D peak evolves as the number of graphitic layers increases.

Raman spectroscopy was also applied to characterize graphene epitaxially grown on SiC substrates. Different from exfoliated graphene, epitaxial graphene is not well characterized. The Raman study done for FLG on C-terminated SiC(000$\bar{1}$) was done to prove the graphene sheets are not bernal-stacked, but are rotated against each other by some degree [53]. However, the usefulness of Raman spectroscopy for studying epitaxial graphene was shown

more obviously in charactering FLG grown on SiC(0001) [54–56].

In this thesis, Raman spectra are taken for epitaxial graphene grown on the Si-terminated face of 6H-SiC, and the Raman peaks are analyzed in conjunction with STM images. This STM study was carried out by Nikhil Sharma, School of Physics, Georgia Institute of Technology. Samples of a few monolayers (ML) thick are required in order to observe interfacial effects projected into top layers. All epitaxial graphene samples used for Raman measurement were grown under ultrahigh vacuum (UHV) conditions. Under UHV growth, it is possible to control the epitaxial graphene thickness to a certain degree by adjusting the growth temperature and time.

5.2 Raman measurement of epitaxial graphene on SiC(0001)

5.2.1 Experiment

5.2.1.1 Sample preparation and characterization in ultra-high vacuum

Pieces of n-doped 6H-SiC(0001) wafer are etched at 1500 °C with 1 atm of 5 percent H_2 / 95 percent Ar. Hydrogen etching is known to remove surface scratches on the surface. H-etched SiC is then transferred into an UHV chamber (base pressure $< 1 \times 10^{-10}$ Torr) and annealed by electron-bombardment heating in the back side. I built the UHV chamber for multi-functional surface analysis. Pictures of the growth and analysis chamber are presented in Figure 5.3. After growth, Auger electron spectra are taken for each sample for thickness calculations. The incident electron energy used to obtain Auger spectra is 3 KeV and the emitted Auger electron is scanned to show Si and C peaks around 90 and 270 eV, respectively. The sample preparation step is illustrated in chapter 4. STM is carried out by Nikhil Sharma for surface characterization of samples. All STM data are acquired using a chemically-etched tungsten probe tips at a constant tunneling current of 100 pA, unless otherwise indicated.

5.2.1.2 Raman spectroscopy on graphene on SiC(0001)

Raman spectrum for each graphene sample is taken in a Renishaw RM 1000 Raman microscope at a fixed laser wavelength of 514.5 nm (2.41 eV) and exit power below 3 mW. The schematic for Raman spectroscopy is illustrated in Figure 5.4. An Ar laser (514 nm)

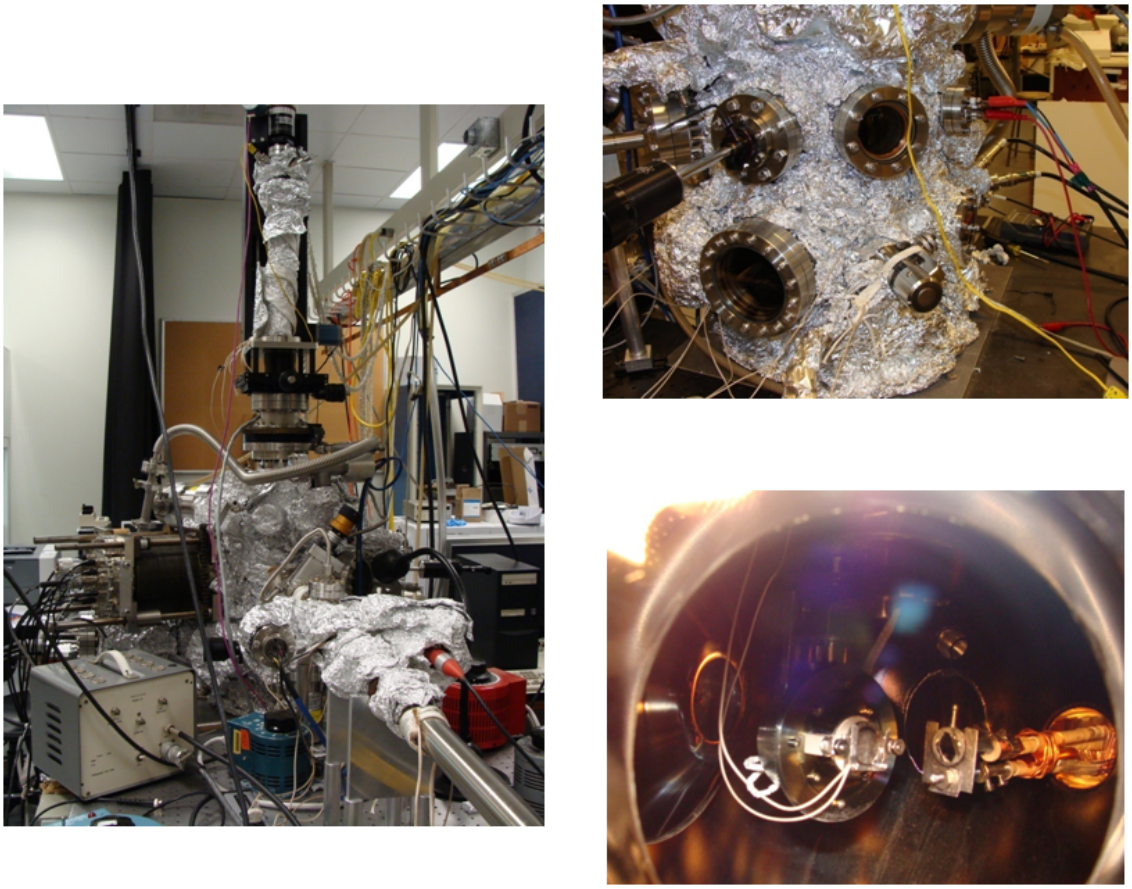

Figure 5.3: Ultra-high vacuum chamber used for graphene growth and Auger electron analysis. The left picture shows the overall chamber structure. The upper right picture shows the feedthrough for electron bombardment heating and the wobble stick for sample manipulation. The bottom right picture shows the rotation sample holder and an e-beam heater inside the chamber.

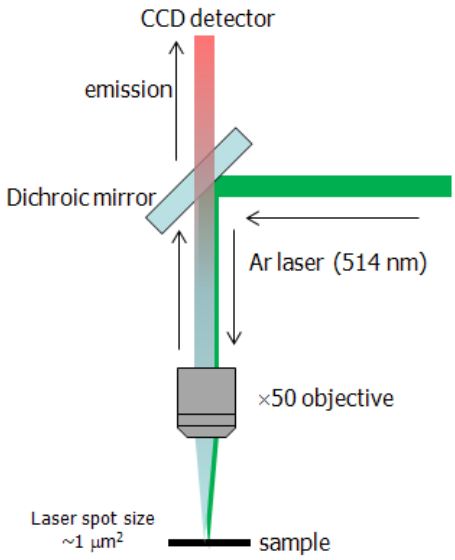

Figure 5.4: Schematic of the Raman measurement is illustrated. An Ar laser is focused to excite samples and the Raman scattering emission is collimated into a CCD detector.

is reflected by the dichroic mirror and focused with ×50 objective into the sample. The Raman beam scattered from the sample is collimated by the objective and passes through the dichroic mirror into the CCD detector. Raman spectra of graphene films are collected by focusing the excitation into volumes containing the graphene epilayer. The laser samples both the graphene overlayer and the bulk SiC substrate. In order to remove the bulk SiC signal, the Raman spectrum is collected with a H-etched SiC substrate by focusing the excitation into the bulk volume below surface. In addition to epitaxial graphene on SiC(0001), highly oriented pyrolytic graphite (HOPG) was also studied.

5.2.2 Data treatment and peak assignment

The way to extract Raman spectra for the graphene overlayers is described in Figure 5.5. Raman spectra of 2.7 and 1.8 ML samples on SiC(0001) substrates are shown together with the 6H-SiC spectrum obtained by focussing the laser into the bulk volume. Linear background intensities from the raw data are removed first. The region around 1950 cm^{-1} gives the same shape for those three spectra. Therefore, they can be normalized at a specific point in that region. The SiC component in the 2.7 ML spectrum is subtracted and then, the result is presented on the top of Figure 5.5. The pure graphene Raman spectrum has

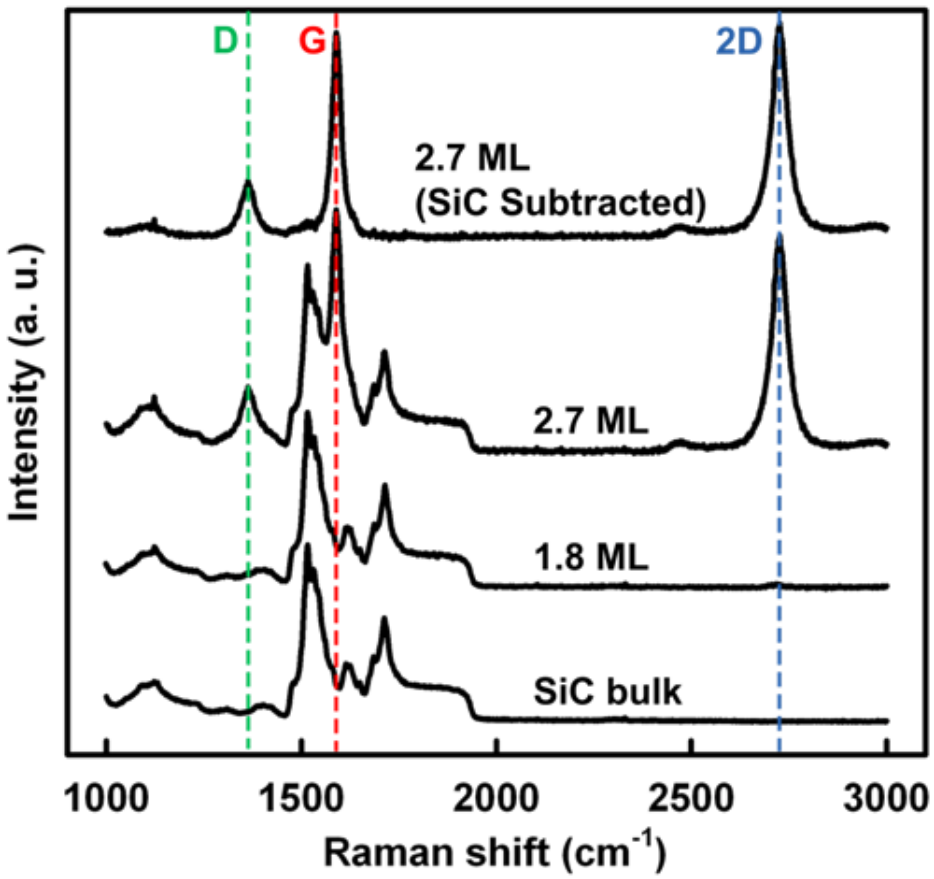

Figure 5.5: The description of obtaining Raman signal of graphene overlayer. Raman spectra of two samples are presented with the SiC bulk spectrum. They are normalized at the SiC edge around 1950 cm^{-1} and the SiC contribution is subtracted from the sample spectrum. Three peaks are notated with the D, G, and, 2D Raman bands.

three pronounced peaks. The peak around 1350 cm^{-1} is the D band and the peak around 1600 cm^{-1} is G the band. The 2nd order D band is also shown on around 2700 cm^{-1}.

5.3 Raman data analysis of epitaxial graphene on SiC(0001)

5.3.1 Mechanism of Raman scattering in graphene

The Dirac cone is introduced to explain the mechanisms of forming the three Raman peaks in graphene. The G band is associated with Γ center localized optical phonon. Because phonons involved in the G band do not have momentum, the excitation is represented by a vertical transition to create an electron-hole pair in the Dirac cone. The upper frame in Figure 5.6 illustrates the mechanism of G band with optical phonons. This process involves one Dirac cone and it is usually related to the amount of sp^2 hybridization in materials.

The D band is associated with the K center and momentum transfer occurs during the Raman process. In this case, another Dirac cone should be involved for a resonance enhanced Raman process. This intervalley Raman scattering can be counterbalanced by impurity-assisted scattering. Because this is an elastic scattering process, overall, only one phonon energy is shifted for emitted Raman photons. Therefore, the D band is related to the impurity structure in graphene such as defects and misfits. The D band mechanism is illustrated in the middle frame of Figure 5.6.

The 2D band has a similar mechanism as the D band, but instead of being an impurity-assisted process, other electron-phonon coupling occurs to balance the momentum change. Thus, the overall wavenumber is shifted twice as much as the first order process. The illustration is located at the bottom frame in Figure 5.6.

5.3.2 Epilayer thickness dependency of Raman spectra

Raman spectra of FLGs on SiC substrates are obtained and plotted in Figure 5.7. Multiple lorentzian fitting is carried out for each plot. Most of the Raman peaks can be resolved with a single lorentzian, but the G peaks in the thin samples (less than 2.5 ML sample) are fit with more than single lorentzian components. In Figure 5.7, minor fitting components are omitted and only fittings which are recognized for the D, G, and 2D bands are shown. Also, intensities for thin samples are multiplied 20 times. It is obvious that there is a big

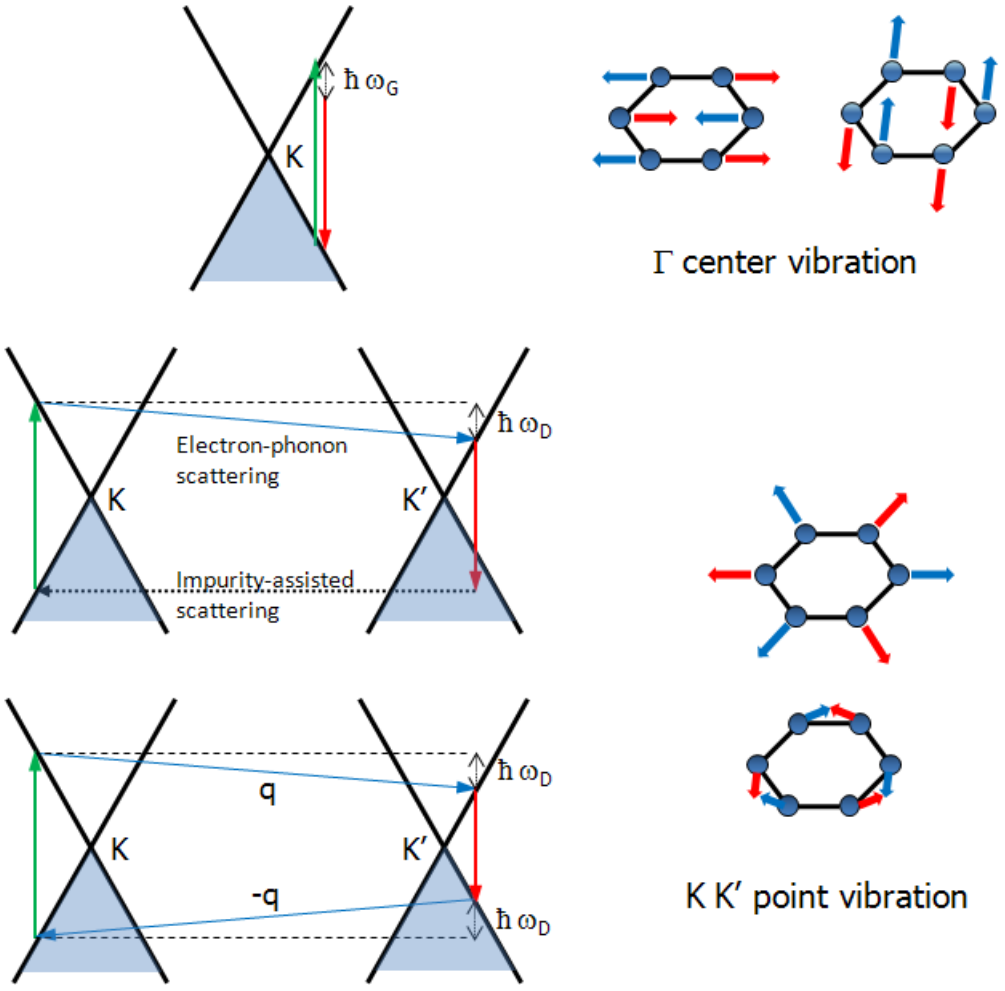

Figure 5.6: Raman scattering processes for the G, D, and 2D bands are presented. The Raman process for the G band occurs in one Dirac cone. The 1^{st} order and 2^{nd} order D band involve inter-valley momentum transfer. Associated phonon modes are also shown besides each Raman processes.

transition of overall intensity between thin and thick samples. This fact might indicate the presence of a buffer layer which does not have the electronic properties of graphene.

The next observable feature is the change of the ratio between the D peak and G peak. The overlayer presence of the D band indicates the presence of defects and other structural impurities in the graphene overlayer. The ratio of the D and G peak is usually recognized as an indicative of the defect density nearby. The Raman spectrum of HOPG does not have a D peak, which means that it is defect free. The last noticeable feature is the evolution of 2D peak. Except the thinnest sample, other samples show the 2D peak with different relative intensities.

5.3.3 Analysis of Lorentzian peaks as a function of few layer graphene thickness

For more quantitative analysis, 4 different features of the lorentzian peaks are presented in this subsection as a function of calculated graphene epilayer thickness. At first, G peak intensity is plotted in Figure 5.8. As mentioned before, the G peak is usually associated with the amount of sp^2 hybridization so that its intensity is believed to be proportional to the thickness of graphene layer. However, the G peak intensity jumps between 2.3 and 2.7 ML samples, which is the extreme deviation from the linear relationship. Actually, the calculated number of layers does include the interface between the graphene epilayer and the SiC substrate. This interface layer is known to be carbon-rich and corresponds to approximately 0.7 graphene-equivalent ML. This could partly explain the large transition of G peak intensity.

If we look at the Raman spectra of the exfoliated graphene in Figure 5.2, it is obvious that the ultra-thin single graphene layer has peak intensities comparable to those in graphite. Even though the interface contribution is subtracted from the overall thickness of epitaxial FLG on SiC, the suppression of the G peak intensity in 1.8 and 2.3 ML samples cannot be easily explained. It is assumed that the interaction of the buffer layer with the first graphene layer would suppress the Raman scattering process in that graphene sheet. For the purpose of obtaining more information about epitaxial graphene, scanning tunneling microscopy (STM) was carried out for 2.2 ML thick epitaxial graphene layer on SiC. This

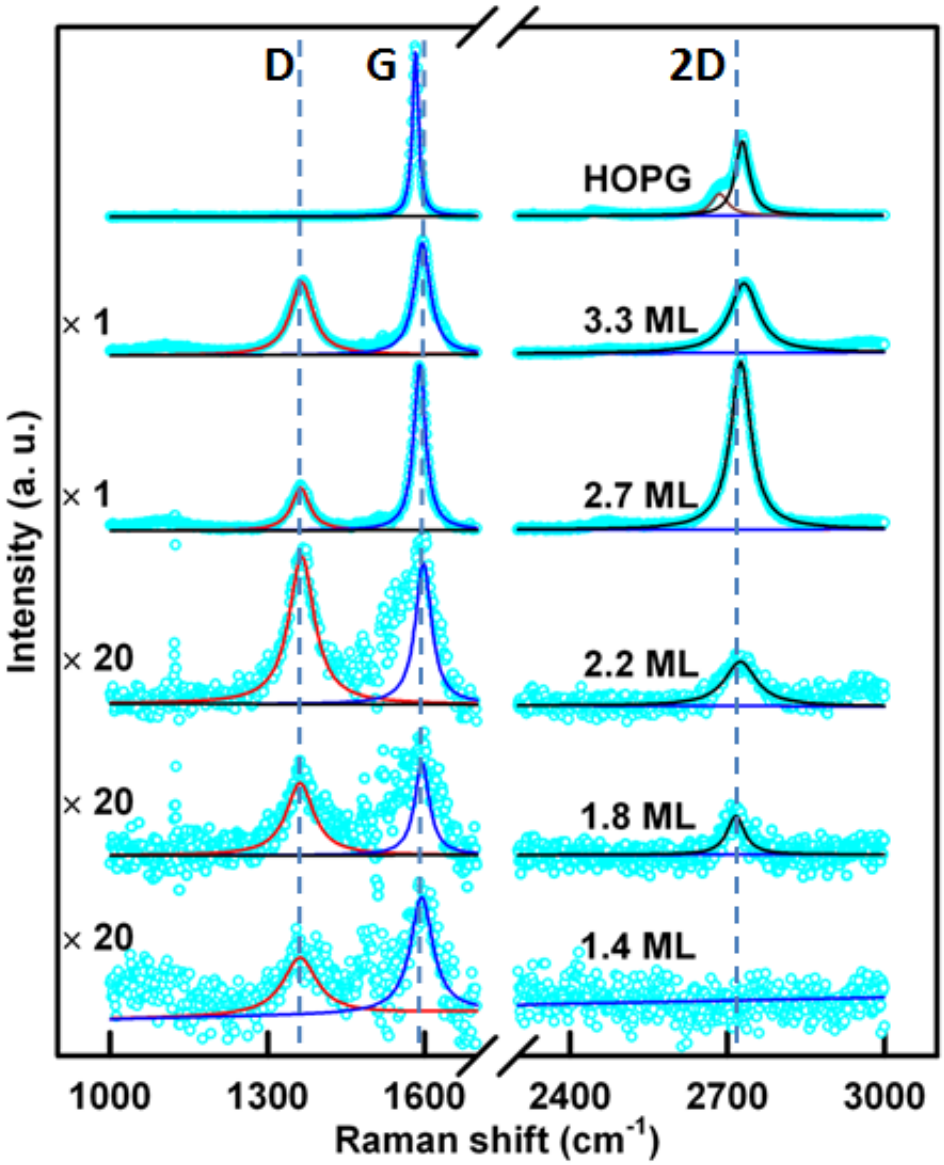

Figure 5.7: Raman spectra of five FLG samples and HOPG are plotted. Each entire spectrum is fit with multiple lorentzians. Measurements for these spectra are carried out collaboratively with Harry Abernathy, and Prof. Meilin Liu group, Materials Science and Engineering, Georgia Institute of Technology.

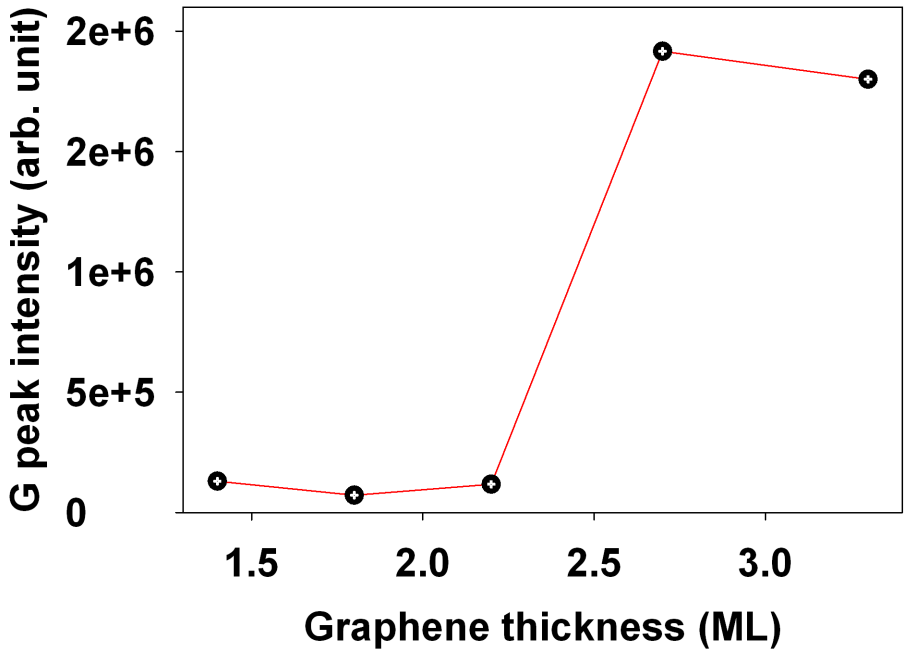

Figure 5.8: The G peak intensity is plotted as a function of graphene layer thickness.

STM data is presented in Figure 5.9. This image has three regions. Region 0 is the carbon-rich interface, region 2 shows the graphene lattice structure with 6×6 surface corrugation. It is interesting to note that region 1 seems to be an overlap of region 0 and 2.

From the STM images and G peak intensity plots, the hypothesis that the G peak suppression is caused by the interaction of buffer layer and the first graphene layer can be supported. The STM image of region 1 can be analyzed as the perturbation of electronic states in the first layer of graphene due to the interaction with buffer layer. It follows that the low energy electronic structure in the Dirac cone is perturbed so that the Raman processes involved in each peaks would be suppressed. Samples thicker than 2.3 ML should have graphene lattices where Raman scattering occurs without suppression thus giving the pronounced intensities for G peaks.

The ratio of D and G peaks is plotted as a function of epilayer thickness in Figure 5.10. The D/G ratio increases and then becomes a minimum in the 2.7 ML sample. It then increases again at 3.3 ML. Because the D/G ratio is known to be related with the defect

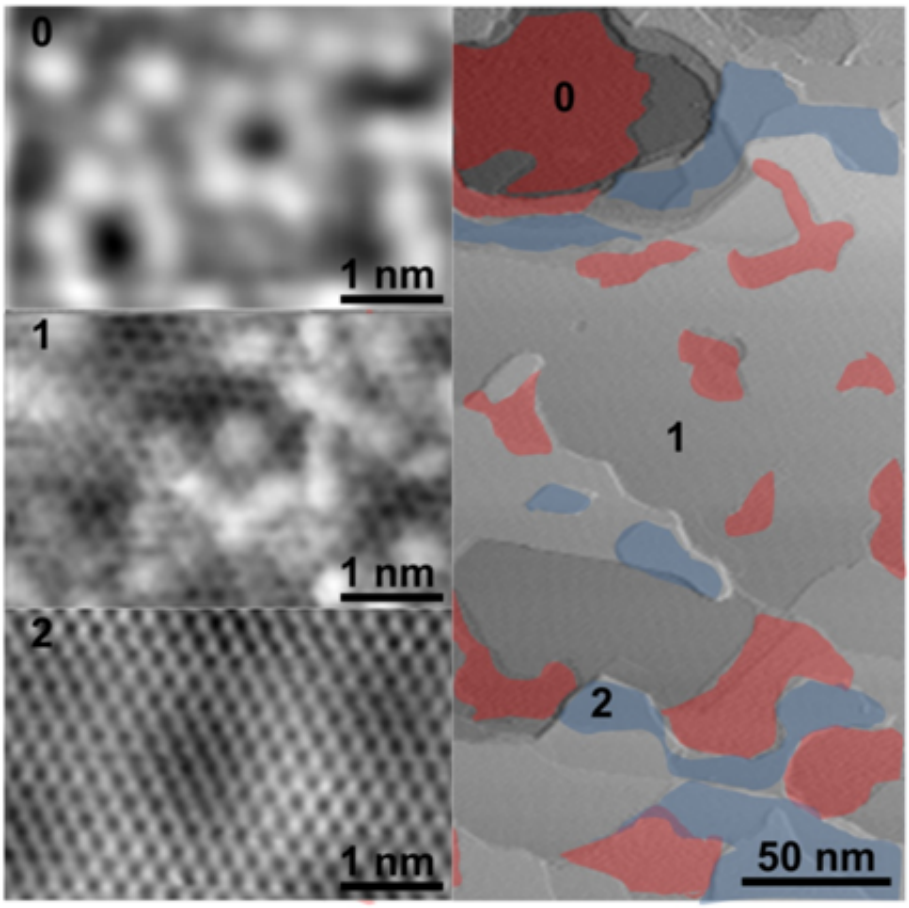

Figure 5.9: Scanning tunneling microscopy images of epitaxial graphene grown on SiC(0001) substrate. The right image is composed of three regions. Three left images are the magnefied ones for each region in the right image. This image was taken by Nikhil Sharma, Phillip First group, School of Physics, Georgia Institute of Technology.

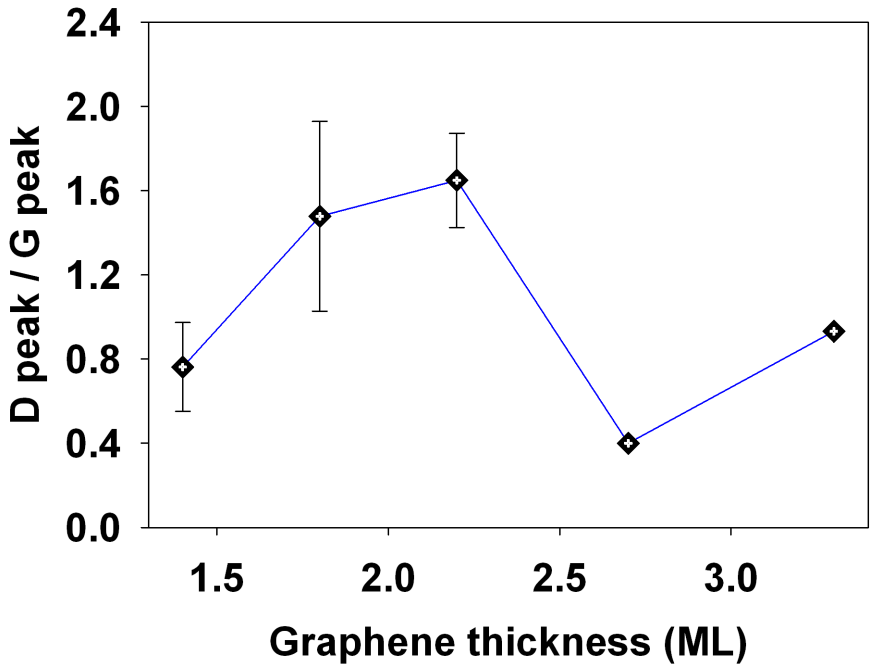

Figure 5.10: The ratio of D and G peak intensities plotted as a function of epilayer thickness.

density of graphene samples, it is instructive to look at the STM image. Actually, the epilayer thickness calculated by the Auger attenuation model is the average thickness so that there are many domains on the STM image. For thin samples, the domain density increases as they become thicker. However, a threshold thickness can be reached whereby the domain density becomes reduced and finally the upper graphene layer should be a graphene sheet with good quality. It could be deduced that the 2.7 ML sample has an average thickness corresponding to approximately two monolayers on top of the buffer layer.

The peak shifts of the Raman spectra are reported to provide useful information concerning the graphene electronic and geometric structure [54, 56]. From lorentzian fitting, each peak position can be obtained. The G and 2D peak shifts of epitaxial graphene relative to those of exfoliated graphene as a function of FLG thickness are plotted in Figure 5.11. The G peak shift tends to increase and becomes minimum at 2.7 ML. In contrast, the 2D peak shift increases as the sample becomes thicker.

It has been suggested [56] that peak shifts in epitaxial graphene on SiC(0001) substrate

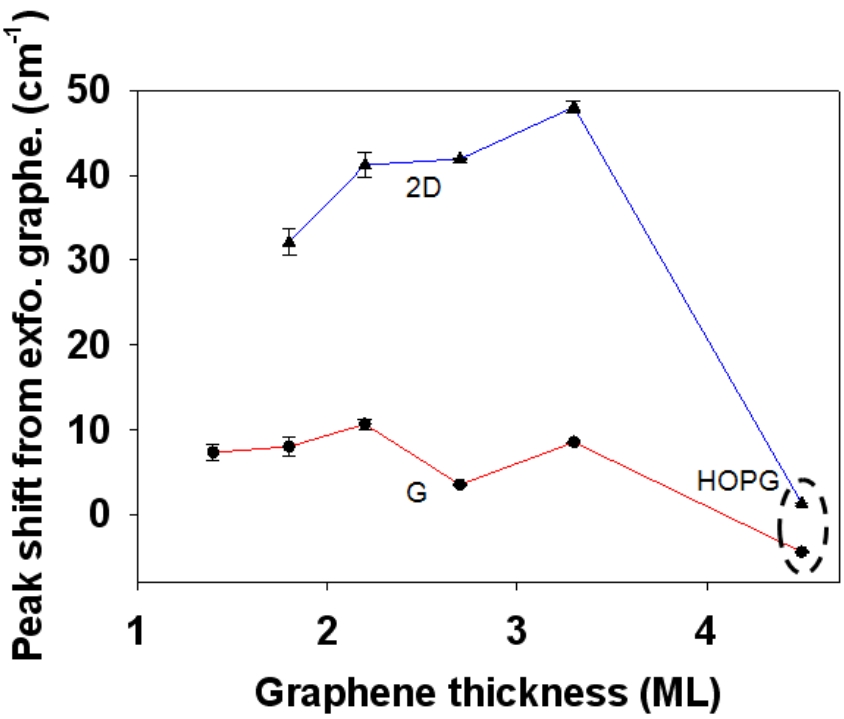

Figure 5.11: Shift of G and 2D peaks from exfoliated graphene are plotted as a function of epilayer thickness. In addition, HOPG shifts are presented.

are induced by the compressive strain of epilayer. Because epitaxial graphene on SiC is produced at high temperature ($< 1200°C$), the difference of thermal expansion coefficient between the epilayer and substrate does generate strain in the thin epilayer. However, the strain effect cannot explain why there is minimum in G peak shift at 2.7 ML. We suggest that the peak shifts come from electronic effects in addition to strain effects. Graphene epilayers are strained compressively during sample cooling. The shift parameter of the G peak is smaller than that of the 2D peak, which means that electronic effects exist, and they are more obvious in the G peak shift than in the 2D shift. The main electronic effect usually comes from doping in the Dirac cone region. We suggest that the thin samples have many small domains which are electron doped due to decoupling from SiC substrate or buffer layer.

5.4 Chapter summary

Raman spectroscopic investigation are carried out for FLG samples grown on SiC(0001) substrates by thermal annealing. A micro-Raman spectrometer is used to take Raman spectra for graphene epilayers. Raman spectra yield three main signature features - D, G, and 2D bands. Lorentzian fitting of the spectra yields a thickness dependency of the Raman spectra. Correlating the STM study of the epitaxial graphene with the Raman data provides useful information about structure and electronic properties. The first graphene epilayer is revealed not to have graphene electronic properties even though it has a graphene lattice. Defect and domain density can be minimized by controlling the epilayer thickness in order to obtain high quality graphene samples. Raman peaks are revealed to be shifted due to electronic doping effect in addition to epilayer strain.

CHAPTER VI

LOW-ENERGY ELECTRON INDUCED DAMAGE IN HYDRATED DNA

Elastic scattering of 5-30 eV electrons within the B-DNA 5'-CCGGCGCCGG-3' and A-tract-DNA 5'-CGCGAATTCGCG-3' DNA sequences is calculated using the separable representation of a free-space electron propagator and a curved wave multiple scattering formalism. The disorder brought about by the surrounding water and helical base stacking leads to featureless amplitude build-up of elastically scattered electrons on the sugars and phosphate groups for all energies between 5-30 eV. However, some constructive interference features arising from diffraction are revealed when examining the structural waters within the major groove. These appear at 5-10, 12-18 and 22-28 eV for the B-DNA target and at 7-11, 12-18 and 18-25 eV for the A-tract-DNA target. Although the diffraction depends upon the base-pair sequence, the energy dependent elastic scattering features are primarily associated with the structural water molecules localized within a 8-10 $\mathring{A}$ sphere surrounding the bases and/or the sugar-phosphate backbone. The electron density build-up occurs in energy regimes associated with dissociative electron attachment resonances, direct electronic excitation and dissociative ionization. Since diffraction intensity can be localized on structural water, compound H_2O:DNA states may contribute to energy dependent low-energy electron induced single and double strand breaks.

6.1 Contemporary research in revealing DNA damage mechanisms

There is strong interest in understanding the elastic and inelastic scattering of low energy electrons with complex targets such as deoxyribonucleic acid (DNA), ribonucleic acid (RNA) and small proteins. The general concern of the medical, chemical, biological, molecular and solid-state physics communities is due to the clear connections with radiation-induced carcinogenesis [57], radiation therapy [57, 58], ultrafast x-ray based structural studies of biological macromolecules [59] and the expectation that DNA can be useful in the burgeoning

field of molecular electronics and nanoscale device architectures [60].

Though the theoretical treatment of electron-molecule scattering is well established for diatomic and tri-atomic systems, there is recent activity that has combined first principles quantum dynamics calculations with state-of-the-art ab-intio scattering calculations to examine the formation and decay of one-hole, two-electron core excited Feshbach resonances in gas-phase water [61, 62]. There are also significant theoretical efforts currently focused on describing low-energy electron collisions with complex polyatomic collision targets. For example, scattering calculations have been carried out on isolated DNA constituents such as the bases [63–65], sugars [66], and phosphates [66, 67]. Some ab-initio electronic structure calculations have examined the mechanisms leading to single strand breaks during low energy electron excitation of shape resonances initially localized on bases [68, 69]. The potential role of water in stabilizing the resonances and mediating electron transfer from the base to the phosphate has been mentioned [68]. However, none of the calculations have explicitly taken into account the importance of hydration and solvent fluctuations on the electron-transfer and scattering processes.

Since DNA is a structured target, elastic scattering may lead to inherent diffraction effects (i.e. coherent scattering) within the target. A theoretical treatment based on the R-matrix method has been carried out to describe elastic scattering with a rare gas target structurally reminiscent of DNA [70–72]. The work has implied that coherence can enhance low-energy electron-induced DNA damage [70–73]. However, experimental investigations on the damage of small sequences of oligonucleotides have begun to refute this [74]. This is particularly true at energies above 10 eV.

In this chapter, I examine elastic scattering within selected DNA sequences using the separable representation of the electron Green function and a curved wave multiple scattering formalism originally developed for calculating x-ray absorption fine structure (XAFS) spectra [24, 75]. Realistic target parameters from x-ray diffraction studies [76, 77] are used so that the roles of diffraction and DNA structural waters in low-energy electron-induced formation of single and double strand breaks (SSBs and DSBs, respectively) can begin to be assessed. The approach is applicable to other large and well-ordered collision partners

and may be a generally useful strategy for examining electron interactions with complex biological targets.

6.2 Calculation of captured electron intensity

6.2.1 Definition of electron targets in model DNA structure

The theory of elastic scattering in complex targets is based on the multiple scattering theory described in chapter 2 and developed to examine diffraction effects in electron-stimulated desorption [16, 33]. It is a modification of the scattering theory introduced to solve problems in photoelectron diffraction [78] and XAFS [24]. This approach calculates and follows incident electron paths using a separable representation of the z-axis propagator. Since the path method was developed for calculating XAFS spectra, this approach is very competitive for electron energies above 20 eV whereas the cluster approach is generally superior for lower energies. The path method is not computationally intensive and can be applied to low-energy electron scattering with complex targets providing energies remain above the inner potential.

The formalism used for calculating incident electron intensity at selected targets is presented in the Calculation section of chapter 3. For the calculation, the B-DNA 5'-CCGGCGCCGG-3' and A-tract-DNA 5'-CGCGAATTCGCG-3' sequences are used to represent the DNA targets. Note C, G, A and T represent cytosine, guanine, adenine and thymine, respectively. Because the inelastic mean free path is short for low-energy electrons (10.6 $\AA$ for biological molecules), the dimensions of these 10 or 12 base pair DNA strands are large enough to sample all atomic scattering centers and guarantees convergence. A spherically symmetric muffin-tin potential is introduced to represent each scatterer constituting the condensed DNA target. An inner potential of $\sim$6 eV is used. This value was deduced from electron holography measurements on biological targets [79] and is the maximum value of the optical potential used in previous R-matrix calculations on a model DNA target [70–72]. The sign of the inner potential is positive which is opposite to that of optical potential used in the R-matrix calculation. This discrepancy arises from the definition of the inner potential. I note that though the calculation includes the effect of the inner

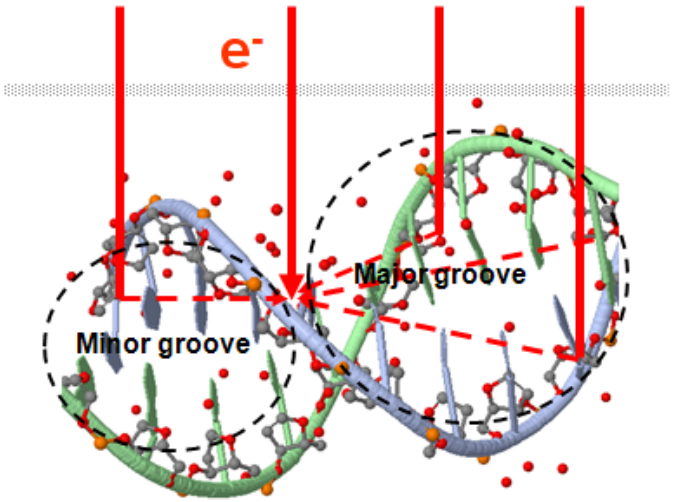

(a) B DNA structure used in calculations

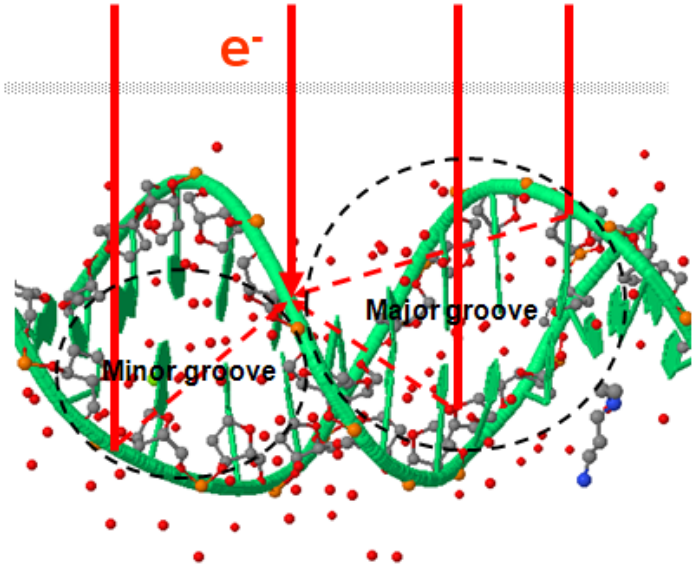

(b) A-tract DNA structure used in calculations

Figure 6.1: (a) The model structure of B-DNA 5'-CCGGCGCCGG-3' is illustrated along with incident electron paths. The detailed structural information was obtained from the protein databank (PDB). The dots in and around target represent the structural water positions extracted from the database. The minor and major grooves are indicated by the dashed-line circles. DNA strands are aligned with the symmetry axis parallel to the surface. Bold vertical lines describe the incident electrons whereas dashed lines are the 1st order scattered components. (b) The model structure of A-tract-DNA 5'-CGCGAATTCGCG-3' is illustrated.

potential, the data presented in this thesis is a function of incident electron energy and thus the inner potential value is subtracted. This shifts the data to lower energy.

In order to compare our calculations to experimental results using oriented DNA targets [80], the DNA strand is directed with its symmetry axis perpendicular to the electron k-vector. The A-tract-DNA with the sequence of 5'-CGCGAATTCGCG-3' and B-DNA with the sequence of 5'-CCGGCGCCGG-3' targets and collision geometries used in our calculations are shown in Figure 6.1. The positions of both the major and minor groove waters are indicated in both structures. In order to reveal the details involved in DNA damage, the approach used in my research gathers all the atoms forming each functional group - a phosphate, a sugar or a structural water - to create the targets for an electron collision. Throughout the calculations, the incident electron density for each atomic state was obtained and collected to produce an effective density for each target. For simplicity, it is assumed that each phosphate, sugar and water target contribute equally. The directly irradiated component is obtained by fixing the phase and decaying the amplitude at the absorber. First-order scattered amplitudes are then calculated with Eq. (20) and interfered with the non-scattered component. Complex phase shifts for each atomic scatterer are calculated with the modified FEFF 8.2 code developed by Rehr *et al* [81].

6.2.2 Electron intensities at each functional group

The calculated elastic scattered electron intensities localized on the sugar, phosphate and water groups in the B-DNA 5'-CCGGCGCCGG-3' target are presented in Figure 6.2, respectively. The same calculation for the A-tract-DNA 5'-CGCGAATTCGCG-3' target sequence is shown in Figure 6.3. In both sequences, the overall scattered intensity is greatest for electrons with incident energy less than 15 eV. The values of the calculated intensities are arbitrary and scale with the number of target atoms. Though these amplitudes do not represent cross sections, the energy dependent scattering amplitudes are important. There is only very weak structure superimposed upon the sugar components between 22-30 eV. The scattered electron intensity is similar for the phosphates, however, there is very weak

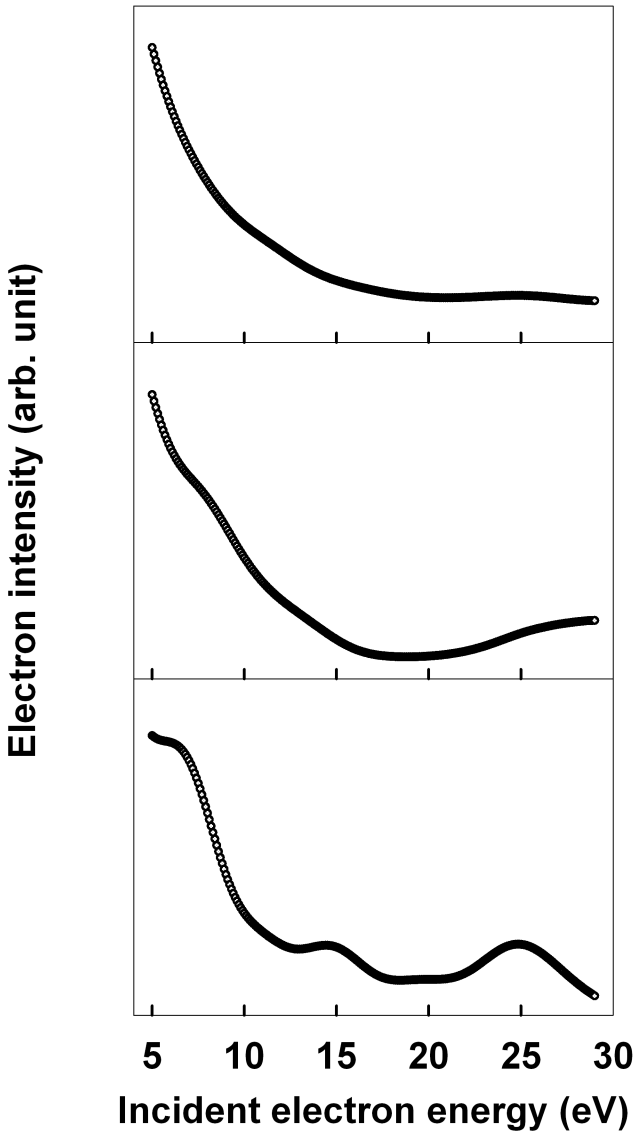

Figure 6.2: Calculated incident electron intensities at selected absorber sites in B-DNA 5'-CCGGCGCCGG-3'. The calculated electron intensity resulting from elastic scattering within a B-DNA target as a function of incident energy. Data for the phosphate is plotted in the upper frame, sugar is in the middle frame, and water groups are in the bottom frame, respectively.

structure observable between 8-12 and 22-30 eV for the B-DNA 5'-CCGGCGCCGG-3' target and 12-20 eV for the A-tract-DNA 5'-CGCGAATTCGCG-3' target. On the contrary, the bottom plots in Figure 6.2 and 6.3 show that constructive build-up of electron intensity due to elastic scattering is clearly more discernable for the water present in both structures.

The hydration of DNA is composed of two regimes: the primary hydration shell involving strongly bound water molecules (< 9 per nucleotide) and secondary hydration shells involving more loosely bound water (up to 20 water molecules per nucleotide). In this work, only molecules in the primary shell are examined theoretically; specifically those in the major and minor grooves. For example, 8 waters within the minor groove and 14 waters within the major groove are used for the calculation for the B-DNA 5'-CCGGCGCCGG-3'. More waters were not included due to an incomplete crystal database. For the A-tract-DNA 5'-CGCGAATTCGCG-3' sequence, 14 waters within the minor groove and 24 waters within the major groove are used. Although it is also known that the major groove waters are typically associated with the presence of cations such as Na^+ or K^+, the positions of these cations are not in the database. There is only one magnesium cation in the A-tract-DNA structure database. Since the current calculation does not take into account the charge, the magnesium cation is assumed to be a P atom for the sake of simplicity. However, I note that it is a worthwhile endeavor to improve the calculations by putting in effective charges and accurate molecular phase shifts.

Contributions of the minor and major groove water are revealed separately in Figure 6.4. Note that there is essentially no structure observed for what is assigned as the minor groove waters (blue triangle), whereas considerable structure in the charge density build-up is associated with the assigned major groove waters (red circle). In the case of the B-DNA, the upper plots show that there is a very pronounced feature between 5-10 eV, a weaker feature between 12-18 eV and a broad feature between 22-28 eV. For the A-tract-DNA, the bottom plots shows that the similar overall structure is still present but much weaker relative to the B-DNA containing only cytosine and guanine. The second peak shifts to higher energy (7-12 eV) and peaks near 10 eV. There are also large and broader features

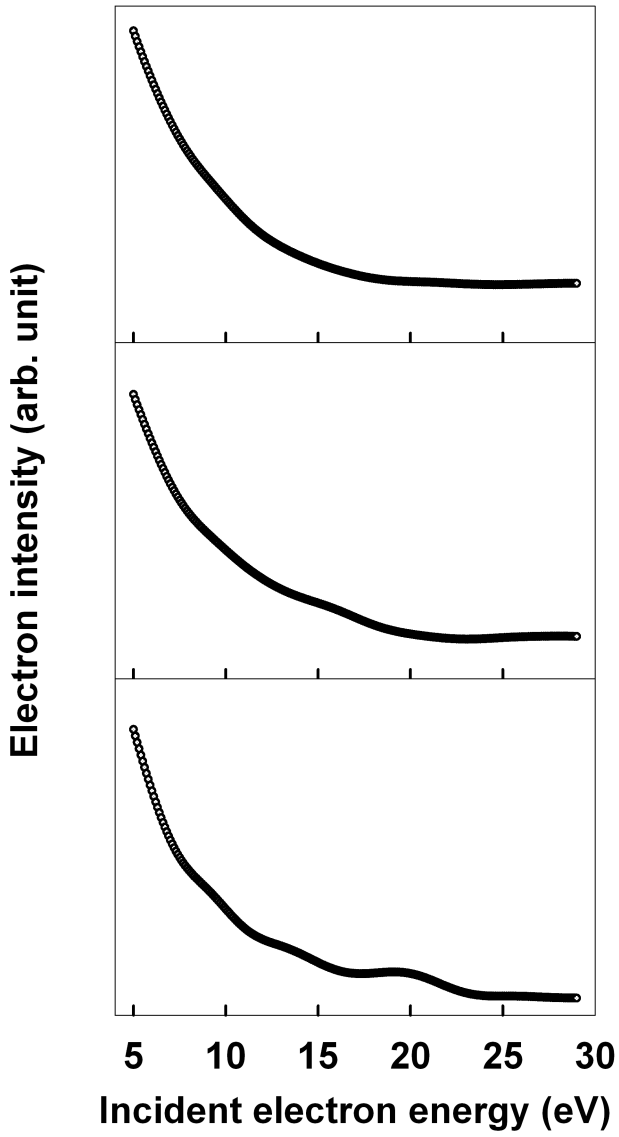

Figure 6.3: Calculated incident electron intensities at selected absorber sites in A-tract-DNA 5'-CGCGAATTCGCG-3'. The calculated electron intensity resulting from elastic scattering within a B-DNA target as a function of incident energy. Data for the phosphate is plotted in the upper frame, sugar is in the middle frame, and water groups are in the bottom frame, respectively.

between 12-18 and 18-25 eV. Figure 6.4 shows that the charge density build-up is dependent upon the base-pair sequence.

The theoretical results can be summarized as i) there is considerable low-energy electron intensity present on the phosphates, sugars and structural waters, especially for incident electron energies below 15 eV, ii) resonance structure is primarily associated with the structural water within the major grooves, and iii) the amplitude build-up occurs between 5-10, 12-18 and 22-28 eV for the B-DNA 5'-CCGGCGCCGG-3' and 7-11, 12-18 and 18-25 eV for the A-tract-DNA 5'-CGCGAATTCGCG-3'.

6.3 DNA damage by electron irradiation and characterization of SSBs and DSBs

Though the DNA sequences we have examined theoretically are only surrogates for more complex DNA targets, it is instructive and useful to compare the results to some recent experiments on low-energy electron induced SSBs and DSBs. These experiments described in this section were carried out by Yanfeng Chen, who was a graduate student in our group. They were done in a constructed apparatus designed by Chen to allow introduction of complex targets, such as DNA thin-films into an ultrahigh vacuum (UHV) (10^{-10} Torr) environment. Briefly, the system has a load lock transfer system magnetically coupled to the UHV chamber, which is differentially pumped and maintained in a nitrogen buffer gas. The UHV system has a variable temperature sample holder, pulsed low-energy (5-50 eV) electron beam, time-of-flight and quadrupole mass spectrometers.

Purified P14 double stranded supercoiled DNA plasmids (6360 base pairs), present as fully solvated species in dilute (200 mg of DNA/ml) aqueous buffer solution, are dispersed on a clean 5 mm $\times$ 5 mm tantalum substrate at room temperature. DNA films with good alignment and unitary orientation can be formed by this simple deposition and drying procedure providing the concentration allows initial formation of a nematic-like crystalline phase [82]. The deposited and vacuum-dried samples are characterized by a scanning electron microscope and are found to be polycrystalline with some aggregation.

Under the sample deposition conditions used in our study, it is impossible for all of the water from DNA to be removed at room temperature. Thus, the DNA samples studied

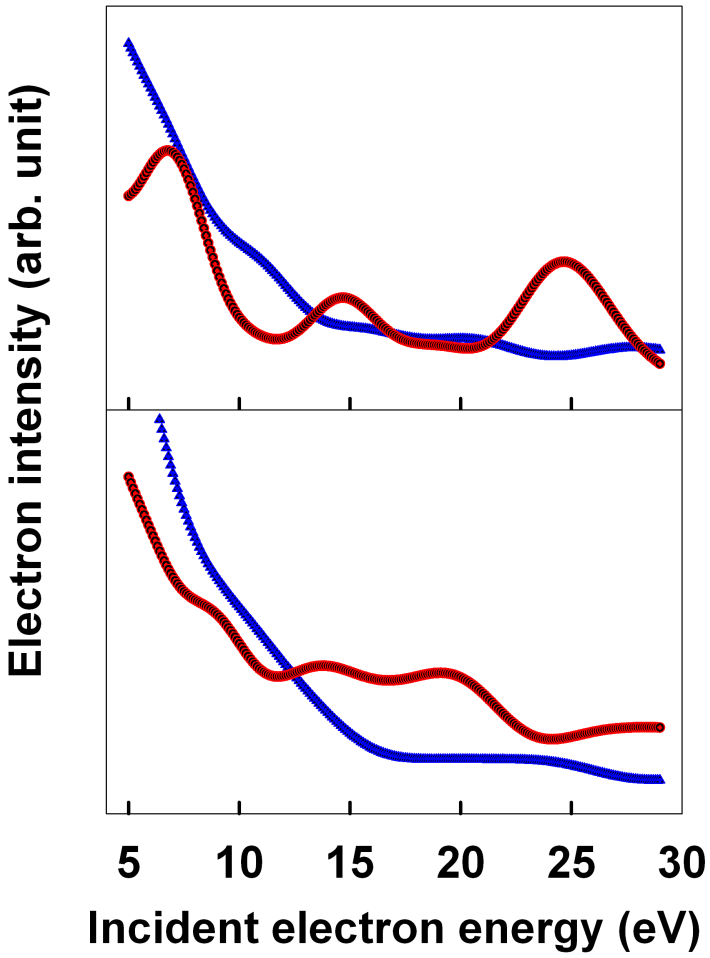

Figure 6.4: A comparison of the calculated electron intensities associated with the structural waters located within the major (red circle) or minor (blue triangle) groove of B-DNA 5'-CCGGCGCCGG-3' and A-tract-DNA 5'-CGCGAATTCGCG-3' targets as a function of incident electron energy

contain trapped water mainly in the form of primary and secondary waters of hydration. Because DNA can chemically decompose upon adsorption onto metal surfaces, 100 monolayer thick films are typically deposited. Since the penetration depth of 5 - 100 eV electrons is in the 15-35 nm range for liquid water or amorphous ice, this thickness reduces the effects of backscattered electrons from the metal substrate. The transmitted current and imaging did not show any evidences for charging. For the damage studies, total electron doses of only 10^{13} electrons/DNA sample are used. This dose is two orders of magnitude lower than that known to induce charging in DNA films [83] and assured a dose response in the linear regime. This dose is delivered in a pulsed mode that allows any charging to be completely dissipated between pulses. It is also more sensitive relative to continuous beam measurements when monitoring anion desorption [84] and is necessary for the preservation of the structures observed in the damage yield vs. incident electron energy.

After electron irradiation, the DNA samples are removed from the chamber and redissolved in water. The amount of DNA is determined from the absorbance at 260 nm before and after irradiation. More than 95 percent of the deposited DNA is recovered from the irradiated samples. The amount of supercoiled plasmids, SSBs and DSBs are then analyzed by ex-situ gel electrophoresis. Three controlled DNA samples are analyzed together with post-irradiation samples: (i) original plasmid DNA solution (ii) a DNA sample that is dried, transferred in vacuum and recovered in water without irradiation, and (iii) DNA with DSBs intentionally induced using the restriction enzyme Sca I. Analysis of the fluorescent light intensities of corresponding ethidium-stained DNA bands yielded quantitative information regarding the number of SSBs and DSBs. The number of SSBs per electron is 10^{-3} and the number of DSBs is at least a factor of 3-4 smaller.

6.4 DNA damage mechanism

6.4.1 Comparison of experiment and calculation

A comparison of the calculated electron density build-up with our measured SSB and DSB probabilities as a function of incident electron energy is shown in Figure 6.5. Though the samples studied are much more complex than the targets used in the calculation, the

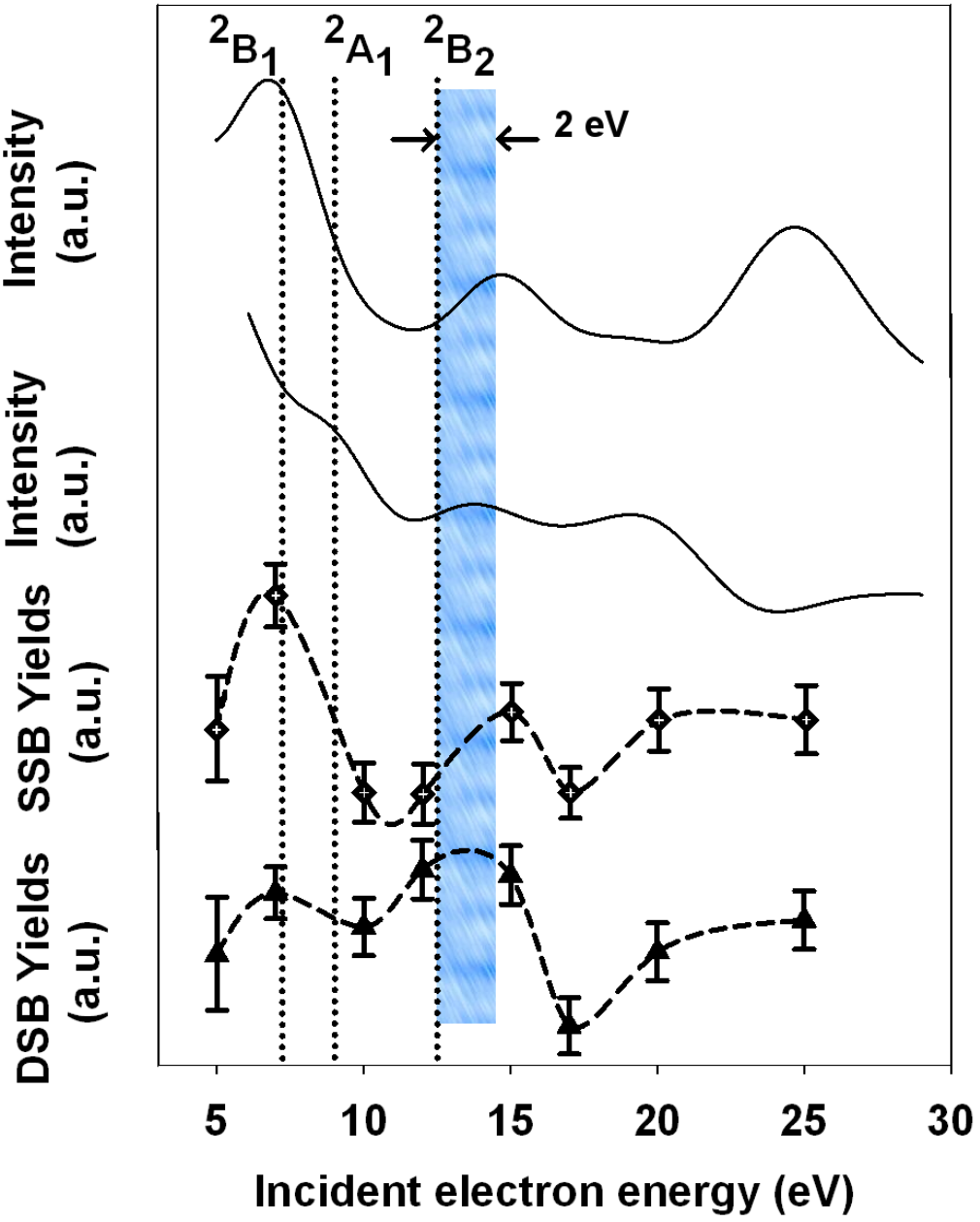

Figure 6.5: Comparison of the electron intensities at major-groove localized waters with SSB and DSB damage yields.

comparison serves to qualitatively illustrate the potential importance of diffraction and structural water in the overall electron-induced break probability. The calculated charge density build-up on the major groove waters of hydration for both DNA targets are shown with the two solid lines on the top half of Figure 6.5. The measured SSB (open diamonds) and DSB (open triangles) yields as a function of incident electron energy are shown in the lower half of Figure 6.5. Each point is taken on a separate DNA film and each point is the average of three or four separate measurements. Though the density of points is low, there is a general correspondence of the SSB and DSB probability with the calculated interference structure in the scattered electron intensity associated with the structural waters found in the major groove. These results are also generally consistent with the first experiments by Sanche and colleagues on DNA plasmid thin films [85] and the more recent experiments demonstrating maxima in the SSB and DSB yields at $\sim$ 9.5 eV in linear and supercoiled DNA [86, 87]. In order to understand these results, I discuss several electronic excitations known to dissociate DNA along with compound states involving water coupled to bases and phosphates.

6.4.2 Damage mechanism at each energy range

6.4.2.1 Low-energy range (0-5 eV)

Though we are not equipped to examine the incident electron energy range for 0 - 5 eV, DNA damage (i.e. SSBs) at incident electron energies as low as 0.8 and 2.2 eV has been reported. The production of SSBs at such low-energies was associated with shape resonances and efficient electron transfer [68, 69]. According to theoretical calculations [68, 69], electrons with incident energies less than 2 - 3 eV can cleave the C-O bond of the DNA backbone through initial capture into a base to form a π^* transient anion followed by transfer via the sugar moiety to the phosphate. This "transferred" electron occupies the dissociative σ^* orbitals of the phosphates at either the 3' or 5' C-O positions and then leads to efficient SSB formation. The role of solvation water in mediating this through bond electron transfer process was mentioned [68, 69], but not explicitly examined in the calculations or experiments.

Coherence and diffraction effects might persist during these low-energy shape resonances. For example, if the incoming electron is scattered along the DNA axis, coherent enhancement could arise from the base stacking and lead to the structures and high cross sections observed at both 0.8 and 2.2 eV. This assumes that the diffracted electron energy is the same as the shape resonance.

6.4.2.2 Medium-energy range (5-15 eV)

Figure 6.5 shows resonant structure in the SSB and DSB probability that is higher energy than those of the shape resonances discussed above. SSBs and DSBs in this energy range can be associated with core-excited Feshbach resonances and dissociative excitation of phosphates, sugars and bases. The core-excited Feshbach resonances can decay via DEA. In fact, recent studies on DEA of DNA bases in the gas-phase have revealed the formation of many fragment anions; especially at energies between 5 and 15 eV [88–91]. Similar experiments on condensed films of nucleobases (i.e. cytosine and thymine) also revealed DEA resonances. However, the overall fragmentation appeared to be less than that in the gas-phase due to interactions with the surroundings [92]. There is recent work on the DEA of gas-phase thymidine (thymine bound to 2-deoxyribose) that addresses the coupling of the base resonances with the attached sugar [93] and other work on condensed short GCAT oligomers [83] which examines base coupling as well as energy transfer to the sugar and phosphate groups. In general, these measurements on simplified systems endorse the original contention that core-excited resonances play a major role in the damage of DNA plasmids for energies between 5-15 eV [85].

There are not many studies of the DEA of the ribose sugars which are subunits of DNA [94], nor has there been much work on isolated phosphates or phosphoric acid [95, 96]. In the case of phosphoric acid and self-assembled monolayers of single or double stranded DNA films, the resonance between 4 and 12 eV leading to O^- and OH^- desorption was attributed to a core-excited resonance localized on the phosphate group [80]. This was investigated further in the only study reported to date which attempts to experimentally address the

role of water in DNA damage [97]. This interesting experiment demonstrated that the co-adsorption of water leads to the formation of new compound resonances associated with water-DNA complexes. The data suggested that the coupling was with the phosphate groups or bases. In addition to changing the DEA lifetimes and resonance energies, the presence of water can affect hole and electron localization [98].

6.4.2.3 High-energy range (15-30 eV)

Since electron resonances are not expected to dominate at these energies, it is expected that the DNA damage results from direct excitation of electronically excited dissociative states or direct dissociative ionization. Dipolar dissociation and direct production of two-hole states also occurs at excitation energies greater than 15 eV. Given the fact that there would be a multitude of possible excitation/fragmentation channels available for incident electron energies > 15 eV, diffraction may not play a role. Therefore, this energy regime is not explicitly examined in this thesis.

6.4.3 The role of water and diffraction in DNA damage

Because the above discussion strongly suggests that water is involved in electron-induced damage of DNA, it should be useful to discuss electronic excitations which lead to DEA of water. It is known that promotion of a $1b_1$, $3a_1$ or $1b_2$ electron to primarily the unoccupied $3s4a1$ level leads to the three prominent DEA resonances in water. These single-hole, two-electron configurations are core-excited Feshbach resonances and are formally written as the $^2B_1 : (1b_1)^{-1}(3s4a_1)^2$, $^2A_1 : (3a_1)^{-1}(3s4a_1)^2$, and $^2B_2 : (1b_2)^{-1}(3s4a_1)^2$ H_2O^- states. In the gas-phase, the $^2B_1$ state decays to form H^-, whereas the $^2B_2$ state decays to form O^- both with high probability [99]. The $^2A_1$ state can yield a mixture of H^- and O^- via nonadiabatic mixing with the $^2B_1$ and $^2B_2$ states [61, 62].

Formation of H^- during low-energy electron interactions with nanoscale water-ice films is primarily produced by decay of the $^2B_1$ resonance [84]. Since the $3a_1$ electronic levels are perturbed by hydrogen bonding and the overall symmetry of the $^2A_1$ resonance precludes long lifetimes in the condensed phase, most of the H^- yield above 9 eV should be due to the $^2B_2$ resonance. DEA favors desorption of light fragments so that the observation

of O^- desorption from water ice is negligible. Instead, this state may be observed in the nonthermal molecular hydrogen channel [100].

The positions of the $^2B_1$, $^2A_1$, and $^2B_2$ states in nanoscale films of water are shown in Figure 6.5. The vertical lines indicate potential correspondences with the positions of features in the SSB and DSB yields. Specifically, the SSB and DSB features between 5-10 eV and 10-17 eV potentially correlate with the $^2B_1$ and $^2B_2$ resonances, respectively [100]. As noted in Figure 6.5, the damage features near 10-17 eV are 2 eV higher in energy and broader than those of the condensed water $^2B_2$ resonance. Similar shifts are observed in comparison with the resonance known to produce O^- directly via DEA of the phosphate group [74]. However, good agreement is reached when compared to the position of the compound resonance recently reported from hydrated GCAT [97]. The observed energy shifts may be consequences of stronger coupling relative to hydrogen bonding in water and modified Franck-Condon factors associated with compound states of water-DNA constituents such as sugar-phosphate groups and bases/counter ions. The reproducible shifts to higher energy (relative to DEA resonances of water and phosphate) in the SSB and DSB probabilities are not caused by charging.

Recent calculations indicate the presence of resonances in phosphoric acid at 7.7 and 12.5 eV [67] and experiments indicate prominent DEA resonances peaking at 5 and 10 eV for most bases [74]. Since these states are nearly degenerate with the DEA resonances of water, they can easily mix and, depending upon the lifetimes, the coupled states could lead to enhanced DEA or increased autodetachment (i.e. electron-emission). Therefore, SSBs can be partially attributed to the formation of H^-, O^-, OH^-, H, O or OH via the decay of the compound (H_2O:DNA) DEA resonances and dissociative excited states. The presence of these reactive anions and radicals in the vicinity of the phosphate-sugar or within the major groove leads to facile bond breakage and is a well known damage mechanism for RNA [101].

As mentioned previously, calculations indicate that facile C-O bond cleavage between the sugar and phosphate groups can be caused by the excitation of the low-lying phosphate σ^* or π^* orbitals. This excitation could initially involve the π^* level of the base, which

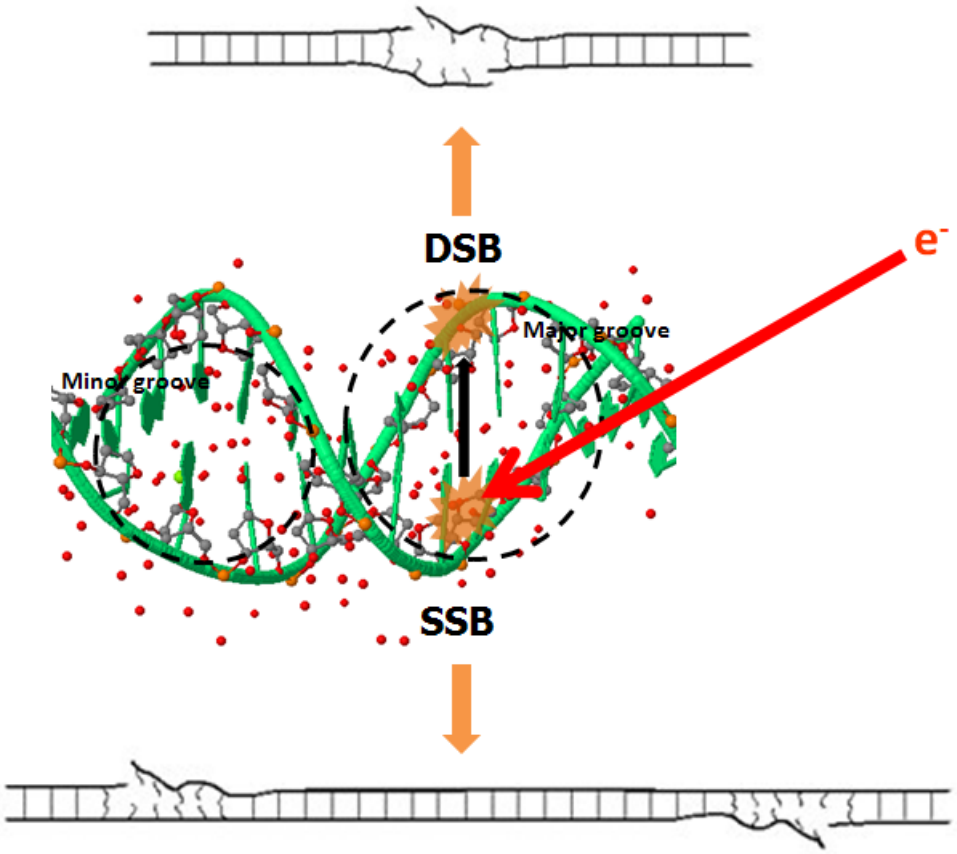

Figure 6.6: Cartoon of SSB and DSB in DNA fragments induced by the low-energy electrons. The black arrow between the SSB and DSB indicates reactive scattering of fragments.

will be transferred through the sugar to the phosphate. If low energy electrons (i.e. those emitted during decay of resonances at and above 5 eV) undergo inelastic scattering within their mean free paths, they can excite a phosphate in their vicinity or on the opposite strand. In the latter case, diffraction can enhance damage, but the inherent site specificity may not be preserved. Since both the initial excitation and the secondary scattering can lead to strand breaks, this could be an efficient path for DSBs. This process is consistent with a DSB threshold energy $\sim$ 5 eV and indicates that DSBs may actually require major groove waters and a compound resonance that simultaneously forms very reactive fragments and a low-energy electron.

Overall, our results indicate that the diffraction amplitude associated with the major groove waters can enhance both the SSB and DSB probabilities by providing a spatially varying charge density with the energy necessary for excitation of water:DNA compound resonances. DNA damage process by low-energy electron irradiation is drawn in Figure 6.6.

6.5 Chapter summary

The elastic scattering of 5-30 eV electrons within the B-DNA 5'-CCGGCGCCGG-3' and A-tract-DNA 5'-CGCGAATTCGCG-3' sequences is represented using the separable representation of a free-space electron propagator and a curved wave multiple scattering formalism. Generally speaking, calculations can be carried out in the low energy regime with reasonable convergence using this method. It shows featureless amplitude build-up on the sugars and phosphate groups for the energy range between 5-30 eV. However, diffraction effects are revealed when examining the structural waters at the major groove that are localized within a 8-10 $\mathring{A}$ sphere around each base and the sugar-phosphate backbone units.

The energy-dependent elastic scattering features appear at 5-10, 12-18 and 22-28 eV for the B-DNA target and at 7-11, 12-18 and 18-25 eV for the A-tract-DNA target. Since diffraction intensity is localized on the water, compound (H_2O:DNA) states involving core-excited Feshbach-type resonances are considered to contribute to the low-energy electron induced SSB and DSB probability. The features between 5-11 and 10-15 eV are potentially associated with the perturbed $^2B_1$ and $^2B_2$ DEA resonances of water, respectively. Electron

autodetachment is also an important decay channel which can lead to secondary scattering and excitation of lower low-lying σ^* or π^* orbitals of the phosphate. DSBs seem to require the simultaneous formation of two reactive entities, and this can be facilitated by structural waters within the major groove. Radiation damage is influenced by the multiple scattering events and thus, internal diffraction can enhance the DNA damage probability, especially for electron energies below 15 eV.

CHAPTER VII

CONCLUSION

Approaches to probe complex interfaces with low-energy electrons were developed. The first task is to examine zone and site specificity in electron-stimulated desorption of Cl^+ from reconstructed Si(111):Cl surfaces. The desorption probability depends on the direction of the incident electron beam and the desorption rate can be correlated with the electron intensity calculated at selected absorbers. The theory used for the intensity calculation originates from the multiple scattering formalism which implements spherical-wave effects by the separable representation of the free-particle Green function. In this thesis, the formalism is reduced into single scattering calculations, but it is still effective in revealing the zone-specific desorption of Cl^+ from Si(111)-7×7 surfaces. Therefore, electron-stimulated desorption may create spatially controlled active sites in a surface unit cell for nano-patterning applications.

The next thing studied in this thesis is an ultra-thin graphitic film called graphene grown on SiC substrates. A few layers of graphene sheet is characterized by Raman spectroscopy. This analysis shows that a carbon-rich buffer layer is created and graphene epilayers are grown above it. The first graphene overlayer is revealed to be Raman inactive due to the perturbation of its electronic structure. Peaks in the Raman spectra for all samples used can be resolved with a single lorenztian and shows the evolution of peak position and width. From these data, useful information concerning surface topography and defect density can be gleaned.

Epitaxial graphene was also probed with angle-resolved Auger spectroscopy. In order to extract final-state effects, two peak areas in the derivative Auger spectra were compared and plotted as a function of azimuthal angle. These plots were compared with calculations of the outgoing Auger electron intensities using the appropriate angular aperture for the CMA. The scattering formalism used was modified to encompass final state effects in the outgoing Auger electron wavefunction. This analysis shows that Auger electron diffraction is

partially affected by the buffer layer, but it depends on the polar angle of measurement. The buffer layer is suggested to be 6-fold symmetric and assimilates to the graphene structure.

The last topic studied was the low-energy electron induced damage of hydrated DNA. Plasmid DNA was irradiated with low-energy electron beams and the gel-electrophoresis analysis showed single and double strand breaks. These occurred primarily via the sugar-phosphate backbone. The probability of strand breaks is compared to the electron intensity at each selected site obtained by the single scattering calculation as a function of electron energy. The best correlation is for structural waters localized within the major-groove of DNA. Therefore, it is suggested that compound states involving the phosphate group and water molecule captures low-energy electrons into dissociative resonance states. This leads to breaking of single strand. Further, decay of the compound resonance produces an electron and this is reactively scattered into the opposite strand to induce double strand break.

For all research topics dealt in this thesis, the single scattering formalism based on path method was applied to accurately represent the perturbation and amplitude build-up due to elastic scattering. For both initial and final-state effect treatments, calculations with the formalism are in good correlation with experimental results. This approach is revealed to be applicable in representing low-energy electron diffraction not only in crystalline material, but also biological systems where the targets are ordered.

Bibliography

[1] T. M. Orlando, A. R. Burns, D. R. Jennison, and E. B. Stechel, "Electronically stimulated adsorbate dissociation in the presence of an electronegative coadsorbate: (nitrogen dioxide + oxygen) atom on platinum(111)," *Physical Review B*, vol. 45, no. 15, p. 8679, 1992.

[2] A. Alexandrov, M. Piacentini, N. Zema, A. C. Felici, and T. M. Orlando, "Role of excitons in electron- and photon-stimulated desorption of neutrals from alkali halides," *Physical Review Letters*, vol. 86, p. 536, 2001.

[3] D. Menzel and R. Gomer, "Desorption from metal surfaces by low-energy electrons," *Journal of Chemical Physics*, vol. 41, no. 11, p. 3311, 1964.

[4] D. Menzel and R. Gomer, "Desorption from surfaces by slow electron impact," *Journal of Chemical Physics*, vol. 40, no. 4, p. 1164, 1964.

[5] M. L. Knotek and P. J. Feibelman, "Ion desorption by core-hole Auger decay," *Physical Review Letters*, vol. 40, no. 14, p. 964, 1978.

[6] R. D. Ramsier and J. T. Yates, "Electron-stimulated desorption: principles and applications," *Surface Science Reports*, vol. 12, no. 6-8, p. 243, 1991.

[7] J. J. Czyzewski, T. E. Madey, and J. Yates, John T., "Angular distributions of electron stimulated desorption ions. Oxygen on tungsten (100)," *Physical Review Letters*, vol. 32, no. 6-8, p. 777, 1974.

[8] C. C. Cheng, Q. Gao, W. J. Choyke, and J. Yates, J. T., "Transformation of chlorine bonding structures on silicon (100)-(2×1)," *Physical Review B*, vol. 46, no. 19, p. 12810, 1992.

[9] T. Yonezawa, H. Daimon, K. Nakatsuji, K. Sakamoto, and S. Suga, "Adsorption and desorption processes of Cl on a si(111)7×7 surface," *Applied Surface Science*, vol. 79-80, p. 95, 1994.

[10] T. D. Durbin, W. C. Simpson, V. Chakarian, D. K. Shuh, P. R. Varekamp, C. W. Lo, and J. A. Yarmoff, "Stimulated desorption of Cl^+ and the chemisorption of Cl_2 on Si(111)-7×7 and Si(100)-2×1," *Surface Science*, vol. 316, p. 257, 1994.

[11] Q. Guo, D. Sterratt, and E. M. Williams, "Valence excitation and ESD of Cl^+ ions from the Cl/Si(100) interface," *Journal of Electron Spectroscopy and Related Phenomena*, vol. 72, p. 31, 1995.

[12] Q. Guo, D. Sterratt, and E. M. Williams, "The adsorption and bonding of chlorine at silicon (100) investigated using ESD/ESDIAD with Cl^+ and Cl^- ions," *Surface Science*, vol. 356, p. 75, 1996.

[13] A. R. Burns, E. B. Stechel, and D. R. Jennison, "Desorption by electronically stimulated adsorbate rotation," *Physical Review Letters*, vol. 58, p. 250, 1987.

[14] A. R. Burns, D. R. Jennison, and E. B. Stechel, "Intramolecular motion during stimulated surface processes," *Physical Review Letters*, vol. 72, p. 3895, 1994.

[15] E. B. Stechel, A. R. Burns, and D. R. Jennison, "Electron-stimulated dissociation of ammonia on Pt(111): observation of gas-phase atomic hydrogen," *Surface Science*, vol. 340, p. 71, 1995.

[16] M. T. Sieger, G. K. Schenter, and T. M. Orlando, "Stimulated desorption by surface electron standing waves," *Physical Review Letters*, vol. 82, p. 3348, 1999.

[17] M. T. Sieger and T. M. Orlando, "Incident beam diffraction in electron stimulated desorption," *Surface Science*, vol. 451, p. 31, 2000.

[18] J. I. Flege, T. Schmidt, J. Falta, and G. Materlik, "Origin of X-ray photon stimulated desorption of Cl^+ and Cl_2^+ ions from Cl/Si(1 1 1)-(1×1)," *Surface Science*, vol. 507-510, p. 381, 2002.

[19] J. Falta, A. Hille, T. Schmidt, and G. Materlik, "X-ray photon-stimulated ion desorption revealed by standing waves," *Surface Science*, vol. 436, p. L677, 1999.

[20] J. I. Flege, T. Schmidt, J. Baetjer, M. Cakmak, G. Materlik, and J. Falta, "Desorption site-specificity and halogen minority sites on Si(1 1 1)," *New Journal of Physics*, vol. 7, p. No pp given, 2005.

[21] J. Berakdar and M. P. Das, "Electron ejection from clean metallic surfaces upon charged particle impact," *Physical Review A*, vol. 56, p. 1403, 1997.

[22] R. Feder, H. Gollisch, D. Meinert, T. Scheunemann, O. M. Artamonov, S. N. Samarin, and J. Kirschner, "Low-energy (e,2e) spectroscopy from the W(001) surface: Experiment and theory," *Physical Review B*, vol. 58, p. 16418, 1998.

[23] A. S. Kheifets, S. Iacobucci, A. Ruocco, R. Camilloni, and G. Stefani, "Mechanism of the low-ejection-energy (e,2e) reaction on a graphite surface," *Physical Review B*, vol. 57, p. 7360, 1998.

[24] J. J. Rehr and R. C. Albers, "Scattering-matrix formulation of curved-wave multiple-scattering theory: Application to x-ray-absorption fine structure," *Physical Review B*, vol. 41, p. 8139, 1990.

[25] A. P. Kaduwela and C. S. Friedman, D. J. Fadley, "Application of a novel multiple scattering approach to photoelectron diffraction and Auger electron diffraction," *Journal of Electron Spectroscopy and Related Phenomena*, vol. 57, p. 223, 1991.

[26] J. Kanasaki, T. Ishida, K. Ishikawa, and K. Tanimura, "Laser-induced electronic bond breaking and desorption of adatoms on Si(111)-(7×7)," *Physical Review Letters*, vol. 80, p. 4080, 1998.

[27] J. Kanasaki, M. Nakamura, K. Ishikawa, and K. Tanimura, "Primary processes of laser-induced selective dimer-layer removal on Si(001)-(2×1)," *Physical Review Letters*, vol. 89, p. 257601, 2002.

[28] T. Gotoh, S. Kotake, K. Ishikawa, J. Kanasaki, and K. Tanimura, "Photoinduced structural instability of the InP (110)-(1×1) surface," *Physical Review Letters*, vol. 93, p. 117401, 2004.

[29] K. Nakayama and J. H. Weaver, "Electron-stimulated modification of Si surfaces," *Physical Review Letters*, vol. 82, p. 980, 1999.

[30] K. Mochiji and M. Ichikawa, "Atomic structural changes of a Br-chemisorbed Si(111)-7×7 surface under 10-150 eV electron impact," *Physical Review B*, vol. 62, p. 2029, 2000.

[31] K. Mochiji and M. Ichikawa, "Electron-stimulated ion desorption from bromine-chemisorbed Si(111) surfaces," *Physical Review B*, vol. 63, p. 115407, 2001.

[32] K. Mochiji, "Reconstruction of Br-chemisorbed Si(111) surfaces under electron-stimulated desorption," *Physical Review B*, vol. 67, p. 113314, 2003.

[33] T. M. Orlando, D. Oh, M. T. Sieger, and C. D. Lane, "Electron collisions with complex targets: Diffraction effects in stimulated desorption," *Physica Scripta*, vol. T110, p. 256, 2004.

[34] J. J. Boland and J. S. Villarrubia, "Formation of silicon (111)-(1×1)chlorine," *Physica Review B*, vol. 41, p. 9865, 1990.

[35] J. S. Villarrubia and J. J. Boland, "Scanning-tunneling-microscopy study of the silicon(111)-7×7 rest-atom layer following adatom removal by reaction with atomic chlorine," *Physical Review Letters*, vol. 63, p. 306, 1989.

[36] R. D. Schnell, F. J. Himpsel, A. Bogen, D. Rieger, and W. Steinmann, "Surface core-level shifts for clean and halogen-covered germanium(100) and germanium(111)," *Physica Review B*, vol. 32, p. 8052, 1985.

[37] J. A. Martin-Gago, E. Roman, M. C. Refolio, J. M. Lopez-Sancho, J. Rubio, L. Hellner, and G. Comtet, "Study of the electronic bonding of Cl-Si(100) by synchrotron radiation photoemission spectroscopy and many-body calculations," *Surface Science*, vol. 424, p. 82, 1999.

[38] D. E. Ramaker, "Covalent interaction effects in electron/photon-stimulated desorption," *Journal of Vacuum Science & Technology, A*, vol. 1, p. 1137, 1983.

[39] K. D. Brommer, M. Galvan, J. Dal Pino, A., and J. D. Joannopoulos, "Theory of adsorption of atoms and molecules on si(111)-(7×7)," *Surface Science*, vol. 314, p. 57, 1994.

[40] K. S. Novoselov, A. K. Geim, S. V. Morozov, D. Jiang, Y. Zhang, S. V. Dubonos, I. V. Grigorieva, and A. A. Firsov, "Electric field effect in atomically thin carbon films," *Science*, vol. 306, p. 666, 2004.

[41] J. S. Bunch, A. M. van der Zande, S. S. Verbridge, I. W. Frank, D. M. Tanenbaum, J. M. Parpia, H. G. Craighead, and P. L. McEuen, "Electromechanical resonators from graphene sheets," *Science*, vol. 315, p. 490, 2007.

[42] Y. Zhang, Y.-W. Tan, H. L. Stormer, and P. Kim, "Experimental observation of the quantum Hall effect and Berry's phase in graphene," *Nature (London)*, vol. 438, p. 201, 2005.

[43] G. Eda, G. Fanchini, and M. Chhowalla, "Large-area ultrathin films of reduced graphene oxide as a transparent and flexible electronic material," *Nature Nanotechnology*, vol. 3, p. 270, 2008.

[44] G. M. Rutter, J. N. Crain, N. P. Guisinger, T. Li, P. N. First, and J. A. Stroscio, "Scattering and interference in epitaxial graphene," *Science*, vol. 317, p. 219, 2007.

[45] A. Bostwick, T. Ohta, T. Seyller, K. Horn, and E. Rotenberg, "Quasiparticle dynamics in graphene," *Nature Physics*, vol. 3, p. 36, 2007.

[46] C. S. Fadley, "Diffraction and holography with photoelectrons and Auger electrons: Some new directions," *Surface Science Reports*, vol. 19, pp. 231–264, 1993.

[47] A. Chassé, L. Niebergall, M. Heiler, H. Neddermeyer, and S. K. M., "Auger electron diffraction in thin CoC films on Au(111)," *Surface Science*, vol. 602, pp. 443–451, 2008.

[48] M. H. Tuilier, P. Wetzel, C. Pirri, D. Bolmont, and G. Gewinner, "Interfacial structure of two-dimensional epitaxial Er silicide on Si(111)," *Physical Review B*, vol. 50, p. 2333, 1994.

[49] S. A. Chambers, H. W. Chen, I. M. Vitomirov, S. B. Anderson, and J. H. Weaver, "Direct observation of elastic strain and relaxation at a metal-metal interface by Auger electron diffraction: Cu/Ni(001)," *Physical Review B*, vol. 33, p. 8810, 1986.

[50] S. Valeri, A. di Bona, and G. C. Gazzadi, "Focusing and defocusing in electron scattering along atomic chains," *Physical Review B*, vol. 50, p. 14617, 1994.

[51] A. C. Ferrari, J. C. Meyer, V. Scardaci, C. Casiraghi, M. Lazzeri, F. Mauri, S. Piscanec, D. Jiang, K. S. Novoselov, S. Roth, and A. K. Geim, "Raman spectrum of graphene and graphene layers," *Physical Review Letters*, vol. 97, p. 187401, 2006.

[52] S. Pisana, M. Lazzeri, C. Casiraghi, K. S. Novoselov, A. K. Geim, A. C. Ferrari, and F. Mauri, "Breakdown of the adiabatic Born-Oppenheimer approximation in graphene," *Nature Materials*, vol. 6, p. 198, 2007.

[53] C. Faugeras, A. Nerriere, M. Potemski, A. Mahmood, E. Dujardin, C. Berger, and W. A. de Heer, "Few-layer graphene on SiC, pyrolitic graphite, and graphene: A Raman scattering study," *Applied Physics Letters*, vol. 92, p. 011914, 2008.

[54] Z. H. Ni, W. Chen, X. F. Fan, J. L. Kuo, T. Yu, A. T. S. Wee, and Z. X. Shen, "Raman spectroscopy of epitaxial graphene on a sic substrate," *Physical Review B*, vol. 77, p. 115416, 2008.

[55] J. Rohrl, M. Hundhausen, K. V. Emtsev, T. Seyller, R. Graupner, and L. Ley, "Raman spectra of epitaxial graphene on SiC(0001)," *Applied Physics Letters*, vol. 92, p. 201918, 2008.

[56] N. Ferralis, R. Maboudian, and C. Carraro, "Evidence of Structural Strain in Epitaxial Graphene Layers on 6H-SiC(0001)," *Physical Review Letters*, vol. 101, p. 156801, 2008.

[57] L. Sanche, "Low energy electron-driven damage in biomolecules," *European Physical Journal D*, vol. 35, p. 367, 2005.

[58] Z. Deng, I. Bald, E. Illenberger, and M. A. Huels, "Reactive scattering damage to DNA components by hyperthermal secondary ions," *Physica Review Letters*, vol. 96, p. 243203, 2006.

[59] R. Neutze, R. Wouts, D. van der Spoel, E. Weckert, and J. Hajdu, "Potential for biomolecular imaging with femtosecond X-ray pulses," *Nature (London)*, vol. 406, p. 752, 2000.

[60] J. R. Heath and M. A. Ratner, "Molecular electronics," *Physics Today*, vol. 56, p. 43, 2003.

[61] D. J. Haxton, C. W. McCurdy, and T. N. Rescigno, "Dissociative electron attachment to the H_2O molecule. I. Complex-valued potential-energy surfaces for the $^2B_1$, $^2A_1$, and $^2B_2$ metastable states of the water anion," *Physical Review A*, vol. 75, p. 012710, 2007.

[62] D. J. Haxton, T. N. Rescigno, and C. W. McCurdy, "Dissociative electron attachment to the H_2O molecule. II. Nuclear dynamics on coupled electronic surfaces within the local complex potential model," *Physica Review A*, vol. 75, p. 012711, 2007.

[63] S. Tonzani and C. H. Greene, "Low-energy electron scattering from DNA and RNA bases: Shape resonances and radiation damage," *Journal of Chemical Physics*, vol. 124, p. 054312, 2006.

[64] C. Winstead and V. McKoy, "Interaction of low-energy electrons with the purine bases, nucleosides, and nucleotides of DNA," *Journal of Chemical Physics*, vol. 125, p. 244302, 2006.

[65] C. Winstead, V. McKoy, and S. d'Almeida Sanchez, "Interaction of low-energy electrons with the pyrimidine bases and nucleosides of DNA," *Journal of Chemical Physics*, vol. 127, p. 085105, 2007.

[66] C. Winstead and V. McKoy, "Low-energy electron scattering by deoxyribose and related molecules," *Journal of Chemical Physics*, vol. 125, p. 074302, 2006.

[67] S. Tonzani and C. H. Greene, "Radiation damage to DNA: electron scattering from the backbone subunits," *Journal of Chemical Physics*, vol. 125, p. 094504, 2006.

[68] R. Barrios, P. Skurski, and J. Simons, "Mechanism for damage to DNA by low-energy electrons," *Journal of Chemical Physics*, vol. 106, p. 7991, 2002.

[69] J. Berdys, P. Skurski, and J. Simons, "Damage to model DNA fragments by 0.25-1.0 eV electrons attached to a thymine p^* orbital," *Journal of Physical Chemistry B*, vol. 108, p. 5800, 2004.

[70] L. G. Caron and L. Sanche, "Low-energy electron diffraction and resonances in DNA and other helical macromolecules," *Physical Review Letters*, vol. 91, p. 113201, 2003.

[71] L. Caron and L. Sanche, "Diffraction in resonant electron scattering from helical macromolecules: A- and B-type DNA," *Physica Review A*, vol. 70, p. 032719, 2004.

[72] L. Caron and L. Sanche, "Diffraction in resonant electron scattering from helical macromolecules: Effects of the DNA backbone," *Physical Review A*, vol. 72, p. 032726, 2005.

[73] Y. Zheng, J. R. Wagner, and L. Sanche, "Dna damage induced by low-energy electrons: Electron transfer and diffraction," *Physical Review Letters*, vol. 96, p. 208101, 2006.

[74] S. Ptasińska and L. Sanche, "On the mechanism of anion desorption from DNA induced by low energy electrons," *Journal of Chemical Physics*, vol. 125, p. 144713, 2006.

[75] J. J. Rehr, S. I. Zabinsky, A. Ankudinov, and R. C. Albers, "Atomic-XAFS and XANES," *Physica B*, vol. 208 & 209, p. 23, 1995.

[76] U. Heinemann, C. Alings, and M. Bansal, "Double helix conformation, groove dimensions and ligand binding potential of a G/C stretch in B-DNA," *EMBO Journal*, vol. 11, p. 1931, 1992.

[77] X. Shui, C. C. Sines, L. McFail-Isom, D. VanDerveer, and L. D. Williams, "Structure of the potassium form of CGCGAATTCGCG: DNA deformation by electrostatic collapse around inorganic cations," *Biochemistry*, vol. 37, p. 16877, 1998.

[78] Y. Chen, F. J. Garcia de Abajo, A. Chasse, R. X. Ynzunza, A. P. Kaduwela, M. A. Van Hove, and C. S. Fadley, "Convergence and reliability of the Rehr-Albers formalism in multiple-scattering calculations of photoelectron diffraction," *Physica Review B*, vol. 58, p. 13121, 1998.

[79] I. G. Stoianova, I. F. Anaskin, and M. D. Shpagina, "Mean internal potential of biological and organic microobjects measured by the electron interference microscope," *Biofizika*, vol. 13, p. 521, 1968.

[80] X. Pan and L. Sanche, "Mechanism and site of attack for direct damage to DNA by low-energy electrons," *Physical Review Letters*, vol. 94, p. 198104, 2005.

[81] A. L. Ankudinov, S. I. Zabinsky, and J. J. Rehr, "Single configuration Dirac-Fock atom code," *Computer Physics Communications*, vol. 98, p. 359, 1996.

[82] N. Morii, G. Kido, H. Suzuki, S. Nimori, and H. Morii, "Molecular chain orientation of DNA films induced by both the magnetic field and the interfacial effect," *Biomacromolecules*, vol. 5, p. 2297, 2004.

[83] Y. Zheng, P. Cloutier, D. J. Hunting, J. R. Wagner, and L. Sanche, "Phosphodiester and N-glycosidic bond cleavage in DNA induced by 4-15 eV electrons," *Journal of Chemical Physics*, vol. 124, p. 064710, 2006.

[84] W. C. Simpson, M. T. Sieger, T. M. Orlando, L. Parenteau, K. Nagesha, and L. Sanche, "Dissociative electron attachment in nanoscale ice films: Temperature and morphology effects," *Journal of Chemical Physics*, vol. 107, p. 8668, 1997.

[85] B. Boudaïffa, P. Cloutier, D. Hunting, M. A. Huels, and L. Sanche, "Resonant formation of DNA strand breaks by low-energy (3 to 20 eV) electrons," *Science*, vol. 287, p. 5458, 2000.

[86] X. Pan, P. Cloutier, D. Hunting, and L. Sanche, "Dissociative electron attachment to DNA," *Physical Review Letters*, vol. 90, p. 208102, 2003.

[87] M. A. Huels, B. Boudaïffa, P. Cloutier, D. Hunting, and L. Sanche, "Single, double, and multiple double strand breaks induced in DNA by 3-100 eV electrons," *Journal of the American Chemical Society*, vol. 125, p. 4467, 2003.

[88] S. Denifl, S. Ptasińska, M. Probst, J. Hrušák, P. Scheier, and T. D. Märk, "Electron attachment to the gas-phase DNA bases cytosine and yhymine," *Journal of Physical Chemistry A*, vol. 108, p. 6562, 2004.

[89] M. A. Huels, I. Hahndorf, E. Illenberger, and L. Sanche, "Resonant dissociation of DNA bases by subionization electrons," *Journal of Chemical Physics*, vol. 108, p. 1309, 1998.

[90] S. Ptasińska, S. Denifl, P. Scheier, E. Illenberger, and T. D. Märk, "Bindungs- und ortsselektive abspaltung von H-atomen aus nucleobasen, induziert durch elektronen sehr niedriger energie (<3 eV)," *Angewandte Chemie*, vol. 117, p. 6949, 2005.

[91] S. Ptasińska, S. Denifl, P. Scheier, E. Illenberger, and T. D. Märk, "Bond- and site-selective loss of H atoms from nucleobases by very-low-energy electrons (< 3 eV)," *Angewandte Chemie, International Edition*, vol. 44, p. 6941, 2005.

[92] M. A. Huels, L. Parenteau, M. Michaud, and L. Sanche, "Kinetic-energy distributions of O^- produced by dissociative electron attachment to physisorbed O_2," *Physical Review A*, vol. 51, p. 337, 1995.

[93] S. Ptasińska, S. Denifl, S. Gohlke, P. Scheier, E. Illenberger, and T. D. Märk, "Decomposition of thymidine by low-energy electrons: implications for the molecular mechanisms of single-strand breaks in DNA," *Angewandte Chemie, International Edition*, vol. 45, p. 1893, 2006.

[94] S. Ptasińska, S. Denifl, P. Scheier, and T. D. Märk, "Inelastic electron interaction (attachment/ionization) with deoxyribose," *Journal of Chemical Physics*, vol. 120, p. 8505, 2004.

[95] C. Konig, J. Kopyra, I. Bald, and E. Illenberger, "Dissociative electron attachment to phosphoric acid esters: The direct mechanism for single strand breaks in DNA," *Physical Review Letters*, vol. 97, p. 018105, 2006.

[96] X. Pan and L. Sanche, "Dissociative electron attachment to DNA basic constituents: The phosphate group," *Chemical Physics Letters*, vol. 421, p. 404, 2006.

[97] S. Ptasińska and L. Sanche, "Dissociative electron attachment to hydrated single DNA strands," *Physical Review E*, vol. 75, p. 031915, 2007.

[98] R. N. Barnett, A. Bongiorno, C. L. Cleveland, A. Joy, U. Landman, and G. B. Schuster, "Oxidative damage to DNA: Counterion-assisted addition of water to Ionized DNA," *Journal of the American Chemical Society*, vol. 128, p. 10795, 2006.

[99] J. Fedor, P. Cicman, B. Coupier, S. Feil, M. Winkler, K. Gluch, J. Husarik, D. Jaksch, B. Farizon, N. J. Mason, P. Scheier, and T. D. Märk, "Fragmentation of transient water anions following low-energy electron capture by H_2O/D_2O," *Journal of Physics B*, vol. 39, p. 3935, 2006.

[100] G. A. Kimmel and T. M. Orlando, "Observation of negative ion resonances in amorphous ice via low-energy (5-40 eV) electron-stimulated production of molecular hydrogen," *Physical Review Letters*, vol. 77, p. 3983, 1996.

[101] G. A. Soukup and R. R. Breaker, "Relationship between internucleotide linkage geometry and the stability of RNA," *RNA*, vol. 5, p. 1308, 1999.

[102] M. I. Katsnelson, K. S. Novoselov, and A. K. Geim, "Chiral tunnelling and the Klein paradox in graphene," *Nature Physics*, vol. 2, p. 620, 2006.

[103] F. Miao, S. Wijeratne, Y. Zhang, U. C. Coskun, W. Bao, and C. N. Lau, "Phase-coherent transport in graphene quantum billiards," *Science*, vol. 317, p. 1530, 2007.

[104] K. S. Novoselov, A. K. Geim, S. V. Morozov, D. Jiang, M. I. Katsnelson, I. V. Grigorieva, S. V. Dubonos, and A. A. Firsov, "Two-dimensional gas of massless dirac fermions in graphene," *Nature (London)*, vol. 438, p. 197, 2005.

[105] K. S. Novoselov, Z. Jiang, Y. Zhang, S. V. Morozov, H. L. Stormer, U. Zeitler, J. C. Maan, G. S. Boebinger, P. Kim, and A. K. Geim, "Room-temperature quantum Hall effect in graphene," *Science*, vol. 315, p. 1379, 2007.

[106] D. Oh, M. T. Sieger, and T. M. Orlando, "Zone specificity in low energy electron stimulated desorption of Cl^+ from reconstructed Si(1 1 1)-7×7:Cl surfaces," *Surface Science*, vol. 600, p. L245, 2006.

VITA

Doogie Oh was born in Seoul, Republic of Korea on September 17, 1973. He was admitted into the Department of Industrial Chemistry, Hanyang University, in 1993 and obtained his degree for Bachelor of Science in 1997. After finishing military service in 1998, he was accepted into the Department of Materials Science and Engineering, Gwangju Institute of Science and Technology. He carried out a project to fabricate an optical amplifier with europium complex doped polymer fiber under the direction of Professor Jang-Joo Kim. Prof. Kim is currently Professor in the Department of Materials Science and Engineering, Seoul National University. Doogie Oh obtained his Master of Science in 2001. Then, he came to Atlanta, United States of America and started his Ph.D degree in the School of Chemistry and Biochemistry, Georgia Institute of Technology. He studied under the direction of Professor Thomas M. Orlando The thesis work was focused on low-energy electron diffraction effects in crystalline surface and biological samples and in proving the applicability of electron scattering theory in complex materials. He obtained his Ph.D degree in Spring, 2009 and will be a postdoctoral fellow in the School of Engineering and Applied Sciences, Harvard University. He will work on developing fluorescence correlation spectroscopy for revealing the mechanism of cell division.